



## CHAPTER 6

## FUNDAMENTAL PHYSICS RESULTS



## **Results of Fundamental Physics Experiments**

**Bob Silberg, Raytheon**

Pierre Meystre of the University of Arizona discussed the use of ultracold fermion atoms, instead of bosonic atoms, in interferometric inertial force sensors.

Juha Javananian of the University of Connecticut spoke of his work on collisionless conversion of a degenerate Fermi gas into molecules in a Feshbach resonance, using a time-dependent Schrodinger equation.

Randy Hulet of Rice University said his team has converted a quantum degenerate Fermi gas of  ${}^6\text{Li}$  atoms into an ultracold gas of  ${}^6\text{Li}_2$  molecules. He said that  $10^5$   $\text{Li}_2$  molecules were created, with an initial phase space density of  $\sim 0.5$ . Their long lifetime (1 sec.) enabled formation of a molecular BEC.

Erik Streed of MIT reported that said the Ketterle team at MIT achieved a Guinness World Record low temperature of 450 picokelvins by overcoming the gravitational influence that keeps gas from expanding and cooling. He said this technology could be useful in high-precision atomic clocks. The goal is atom interferometry on a chip with two BECs.

Murray Holland of JILA and the University of Colorado presented his team's work on resonance superfluidity in dilute fermion gases. He said that beyond fundamental physics, this work can be applied to the creation of optical lasers and matter-wave lasers.

John Thomas of Duke University said that observations by his team provided the first evidence for superfluid hydrodynamics in a strongly attractive Fermi gas.

Horst Meyer, also of Duke University, reported on numerical simulation studies of the transient-to-steady convection in a supercritical fluid.

Harry Kojima of Rutgers University discussed stress-driven instability on a solid  ${}^4\text{He}$  surface. This addresses the problem of what happens to an object's shape when it begins as a solid in equilibrium with its melt, and then external stress is applied. The surface is expected to become unstable and develop corrugation. He said the phenomenon can be seen macroscopically in land formations in Ireland, and in drying starch, and the issue has implications for assembly of nanostructures by self-organization.

In a departure from the general theme of the workshop, Douglas Osherooff of Stanford University, who was a member of the Columbia Accident Investigation Board, reported on the investigation and its results.



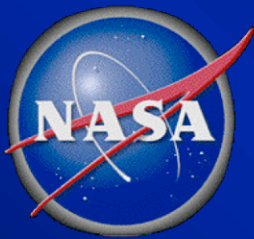
# Fermionic atom optics

... or, preaching the fermionic gospel

Chris Search ( \_ Stevens Inst. Of Technology )  
Markku Jääkseläinen  
Takahiko Miyakawa

Henning Christ ( \_ MPQ Garching )  
Dennis Douglas  
Ben Kalafut  
Dominic Meiser

Mike Moore ( \_ Ohio U. )

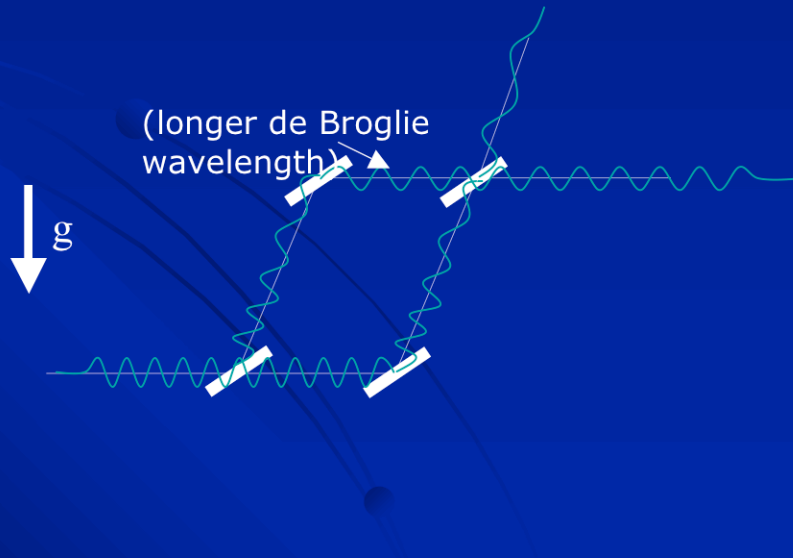


# Atom Interferometer Force Sensors

Use quantum mechanical wave-like properties of atoms to sense inertial forces.

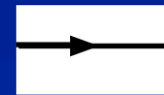
## Gravity/Accelerations

As atom climbs gravitational potential, velocity decreases and wavelength increases



## Rotations

Rotations induce path length differences by shifting the positions of beam splitting optics



(From M. Kasevich)

# Atom optics with fermions

- **Fermionic interferometer**

- **Fermionic three-wave mixing**

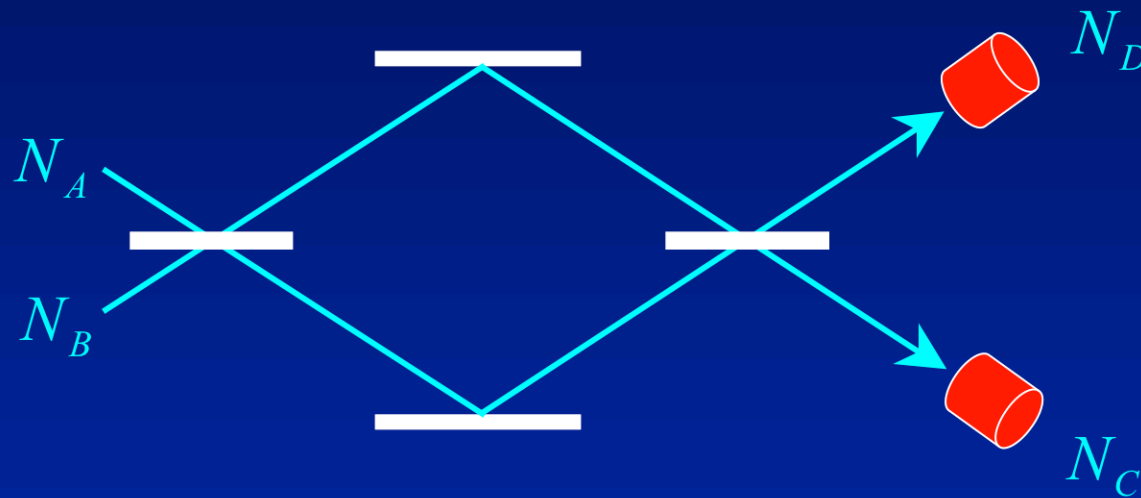
Molecular “micromaser”

- **Fermionic four-wave mixing**

Dicke superradiance  
“phase-conjugation”



# Atom Interferometer\_ Bosons versus fermions



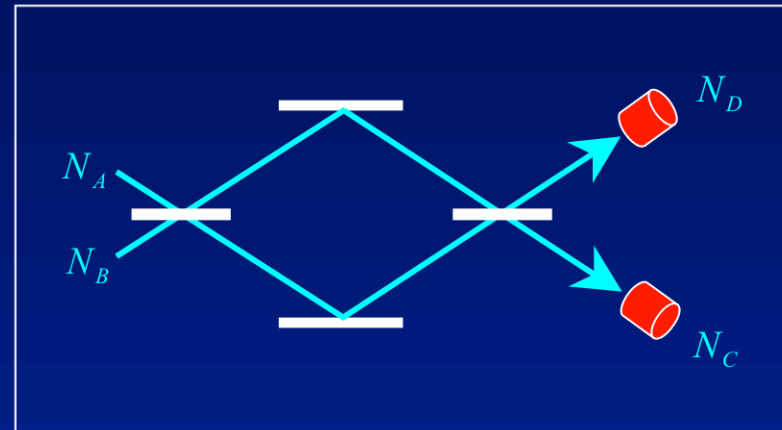
- Mach-Zehnder interferometer
- Quantum degenerate Bose or Fermi beam
- Collisions
- Pauli exclusion principle

# Phase fluctuations

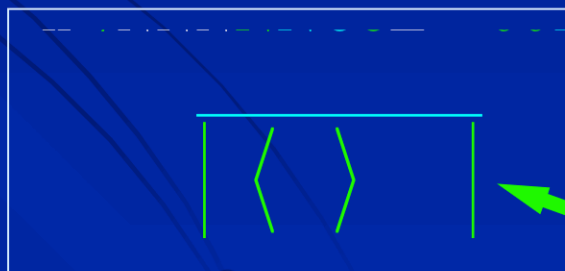
Difference in number of counts:

$$\hat{N} = \hat{N}_D - \hat{N}_C$$

$$\langle \hat{N} \rangle = \langle \hat{N}_A - \hat{N}_B \rangle \cos \theta \quad (\text{uncorrelated inputs, noninteracting atoms})$$



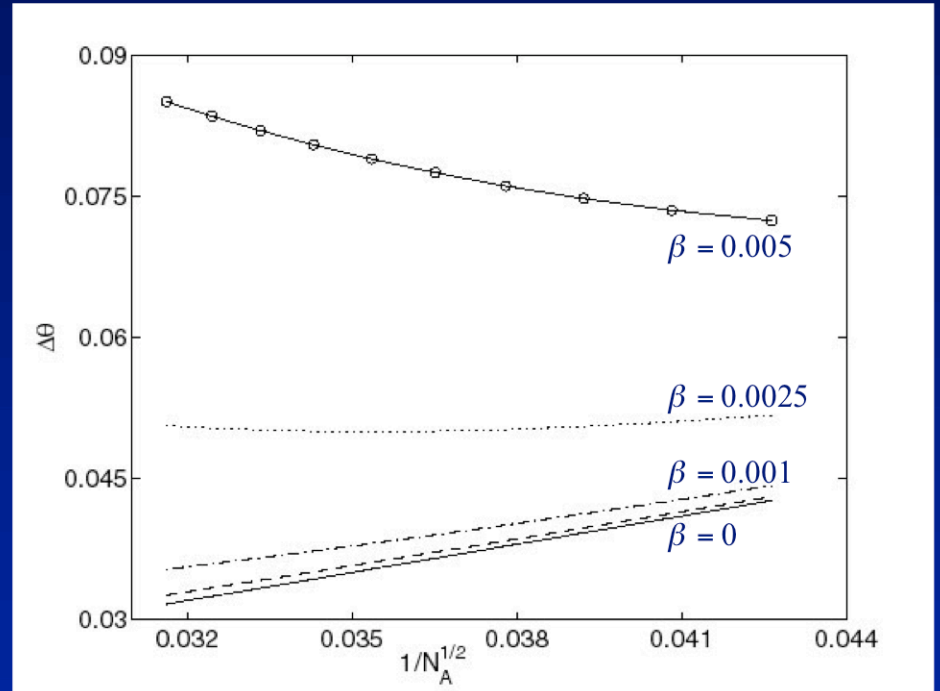
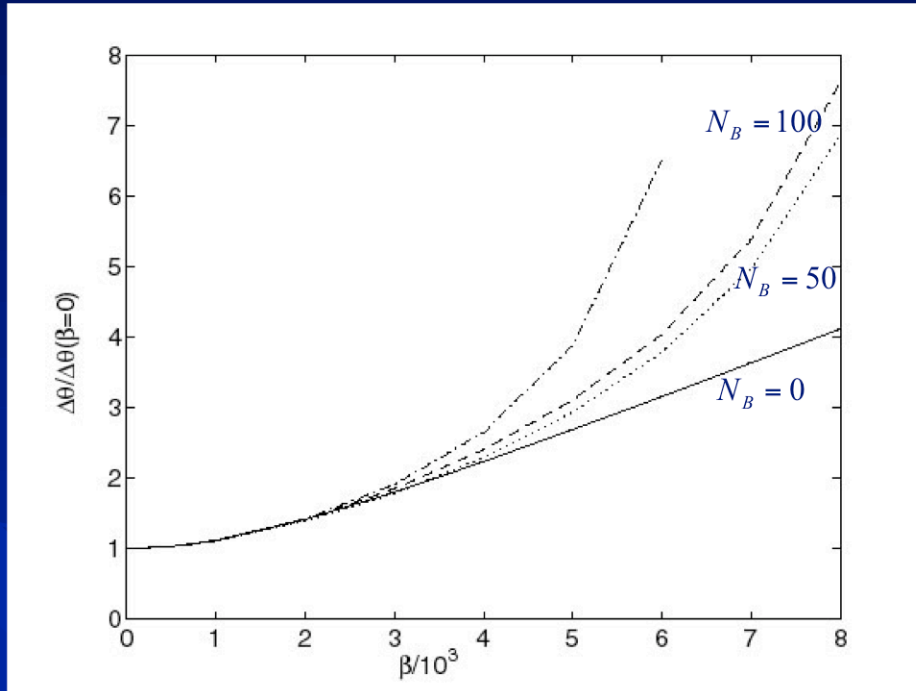
Fluctuations:



$$\sqrt{\langle \quad \rangle \langle \quad \rangle}$$

Intrinsic fluctuations

# Phase sensitivity \_ bosons



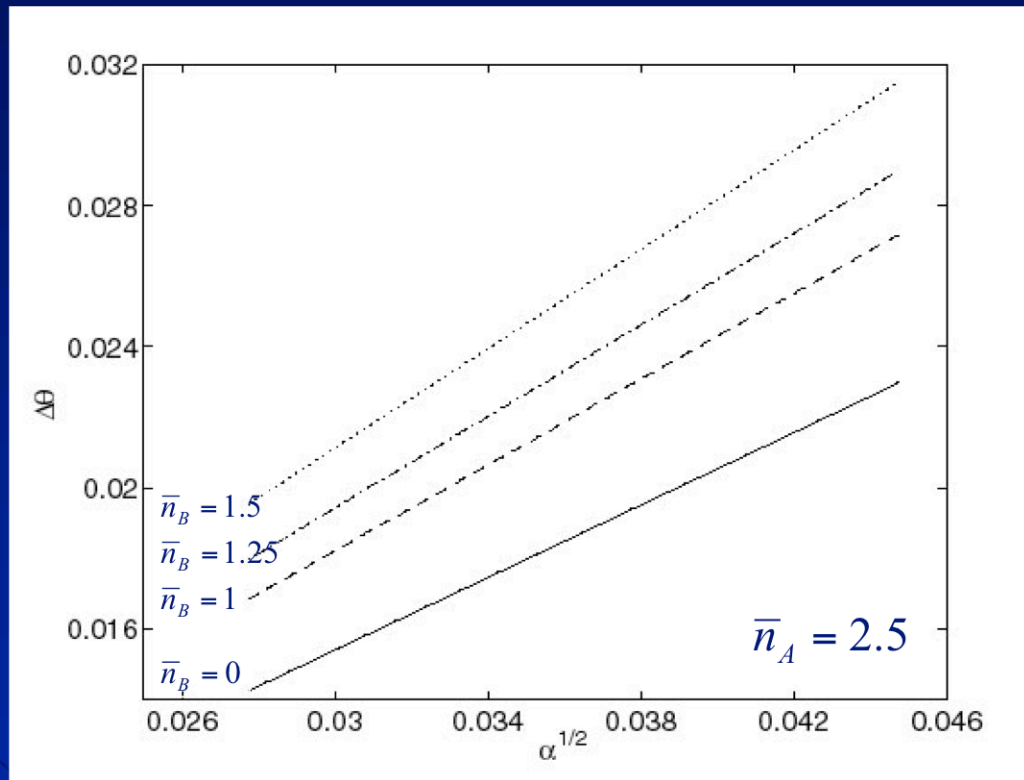
$$N_A = 1000$$

$$\theta = \pi / 2, \quad N_B = 0$$

$$\beta = \frac{4\pi \hbar a}{M\ell} (t_u + t_\ell) \int d^2 r_\perp |\phi_0(\mathbf{r}_\perp)|^4$$



# Phase sensitivity \_ fermions

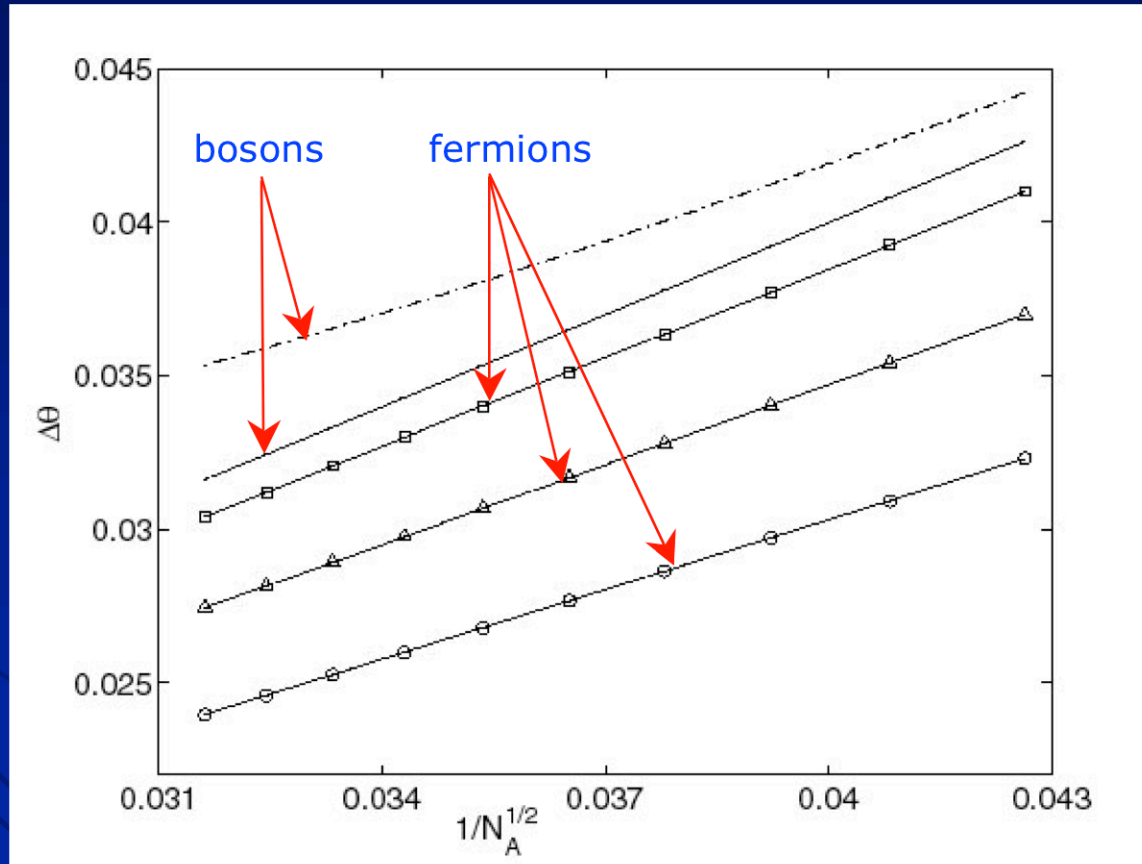


$$\bar{n}_A = \frac{2\pi n_A}{k_0} = \frac{2k_{F,A}}{k_0}$$

$$\alpha = N^{-1}$$

(Degree of monochromaticity)

# Bosons versus fermions



$$\beta = 0.001$$

$$\beta = 0$$

$$\bar{n}_A = 1$$

$$\bar{n}_A = 2$$

$$\bar{n}_A = 3$$

$$N_B = 0$$

# Experiment

## Atom interferometry with trapped Fermi gases

G. Roati, E. de Mirandes, F. Ferlaino, H. Ott, G. Modugno and M. Inguscio

*LENS and Dipartimento di Fisica, Università di Firenze, and INFN*

*Via Nello Carrara 1, 50019 Sesto Fiorentino, Italy*

(Dated: February 13, 2004)

We realize an interferometer with an atomic Fermi gas trapped in an optical lattice under the influence of gravity. The single-particle interference between the eigenstates of the lattice results in macroscopic Bloch oscillations of the sample. The absence of interactions between fermions allows a time-resolved study of many periods of the oscillations, leading to a sensitive determination of the acceleration of gravity. The experiment proves the superiority of non interacting fermions with respect to bosons for precision interferometry, and offers a way for the measurement of forces with microscopic spatial resolution.

arXiv: cond-mat/0402328



# Experiment (cntd)

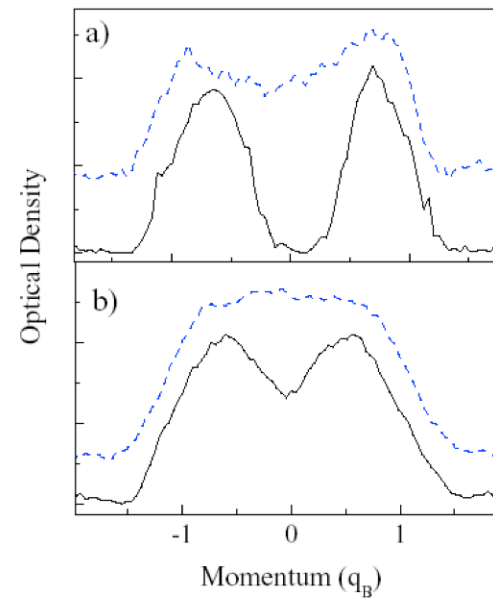
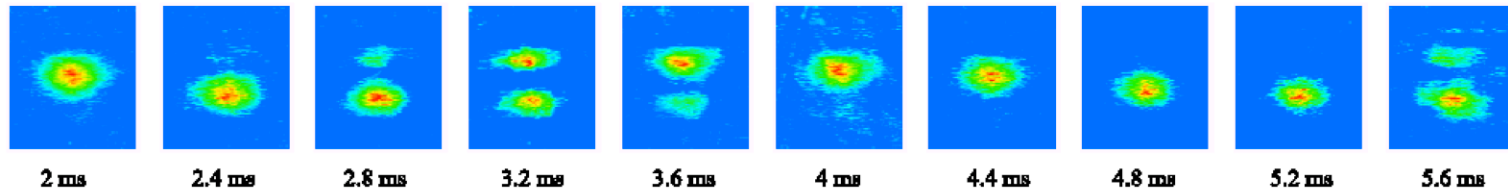
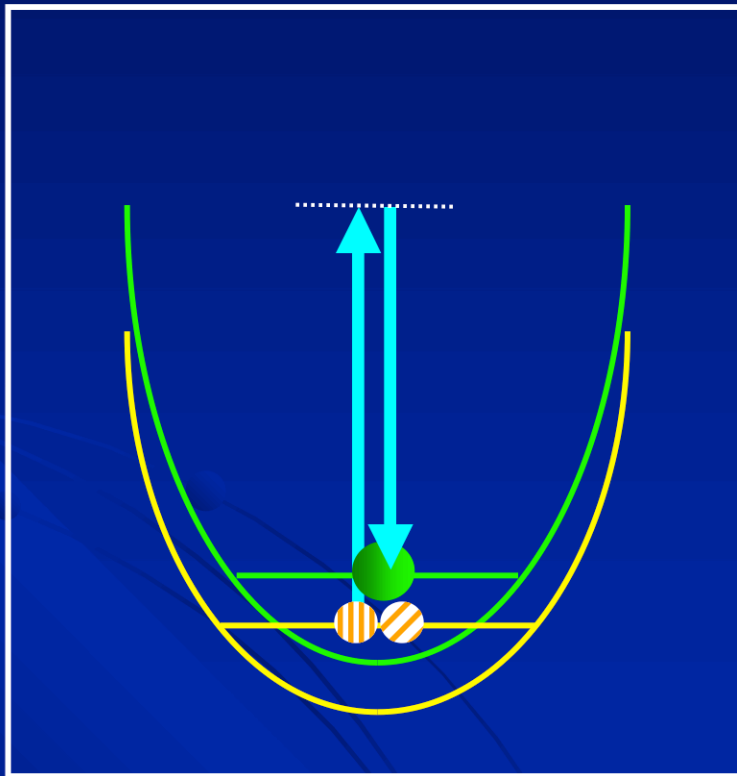


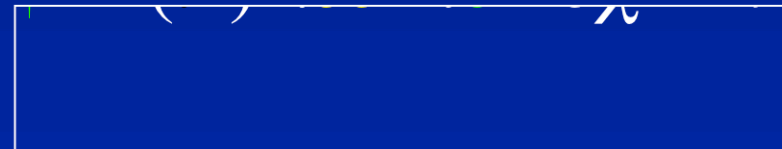
FIG. 4: a) Momentum distribution of fermions at two different holding times in the lattice: 1 ms (continuous line) and 252 ms (dashed line). b) Momentum distribution of bosons at 0.6 ms (continuous line) and 3.8 ms (dashed line). The much faster broadening for bosons is due to the presence of interactions.

# 3-Wave Mixing: Photoassociation



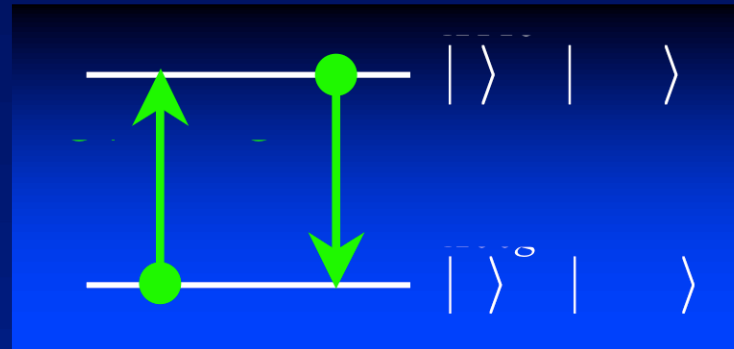
Two distinguishable **atomic fermions**  
in trap ground state

One **bosonic molecule** in trap ground state



# Mapping

$$\left\{ \begin{array}{l} \sigma_- = \hat{c}_1 \hat{c}_2 \\ \sigma_+ = \hat{c}_2^\dagger \hat{c}_1^\dagger \\ \sigma_z = \hat{c}_1^\dagger \hat{c}_1 + \hat{c}_2^\dagger \hat{c}_2 - 1 \end{array} \right.$$



- Molecules in Mott insulator state
- Neglect atomic intersite tunneling during photoassociation (multi-well trap)



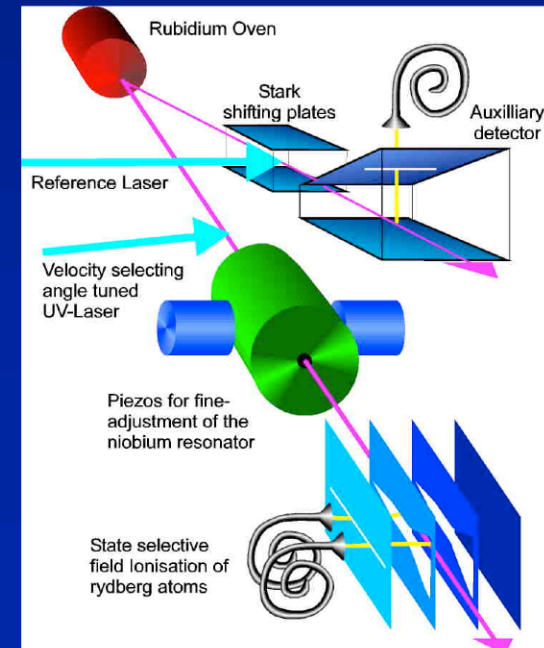
**Reduces to Jaynes-Cummings model for  $U_x$  and  $U_b \rightarrow 0$**



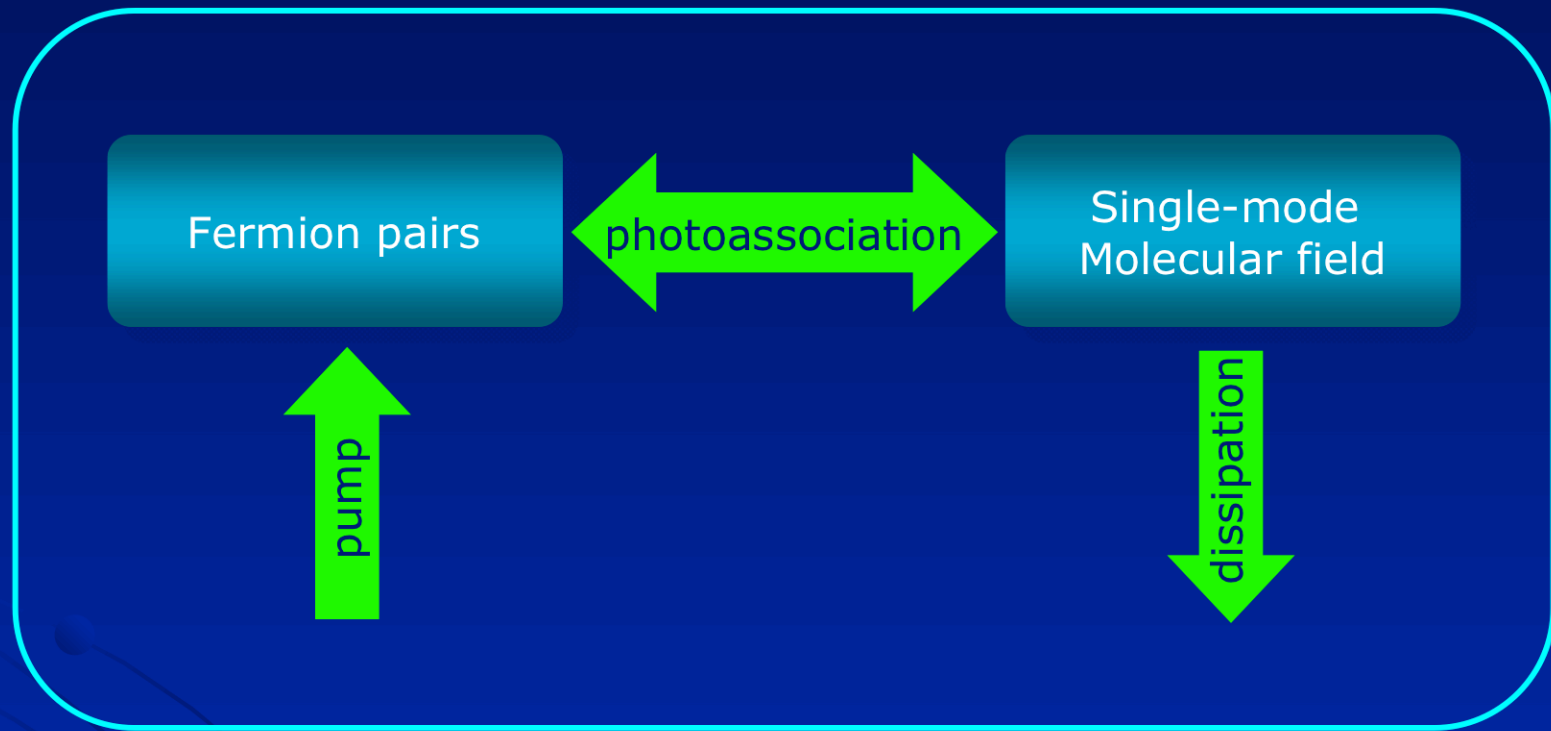
# Micromaser

- Single-mode lasers far above threshold produce **coherent state**.
- Micromasers can produce **nonclassical states**, Fock states, squeezed states, etc...
- Micromasers undergo a series of first-order-like **phase transitions** past the usual laser threshold.

- **Matter-wave analog of a micromaser**
- **Cavity matter-wave optics**



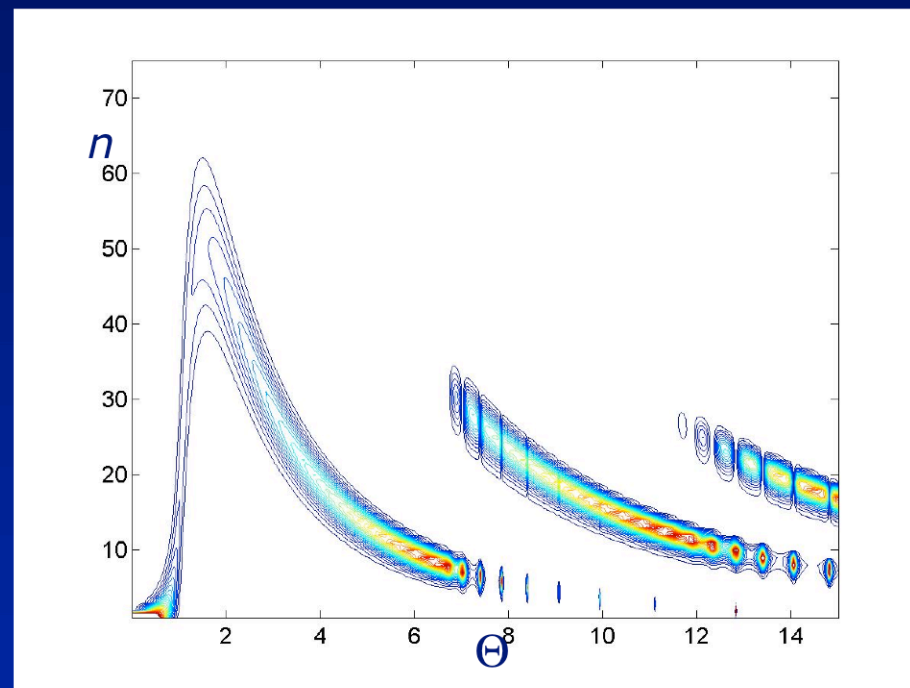
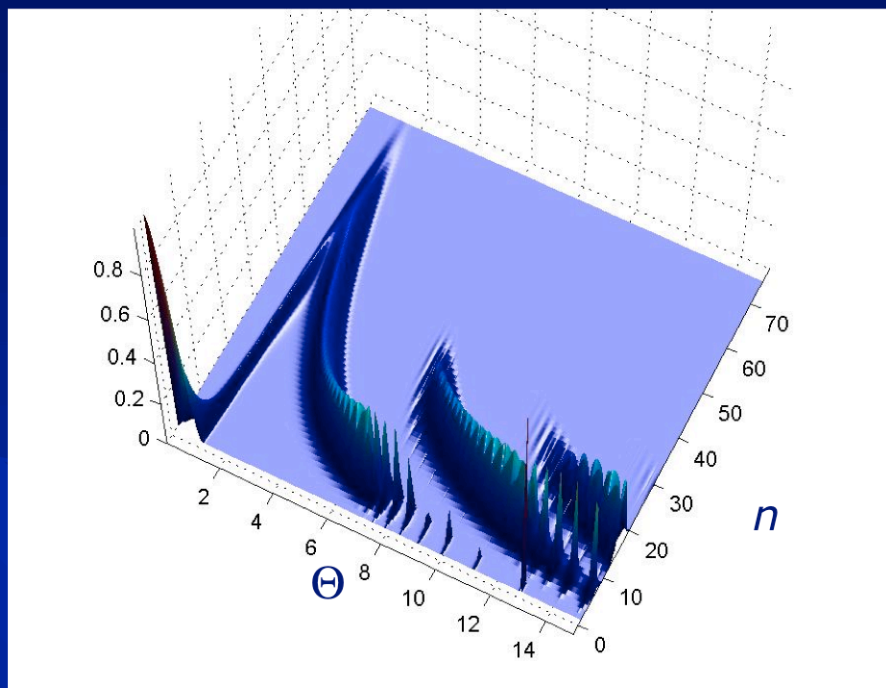
# Micromaser-like model



Photoassociation: Jaynes-Cummings Hamiltonian

$$H_P = \hbar\omega_0 \sigma_z + \hbar\omega a^\dagger a + \hbar g (a\sigma_+ + a^\dagger\sigma_-) + \text{nonlinear terms due to collisions}$$

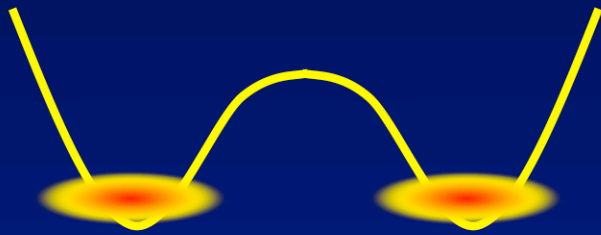
# Molecule statistics



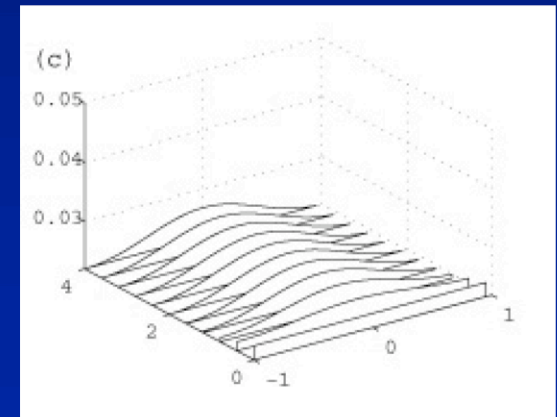
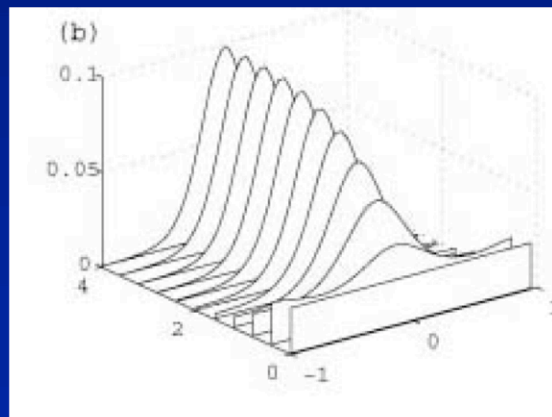
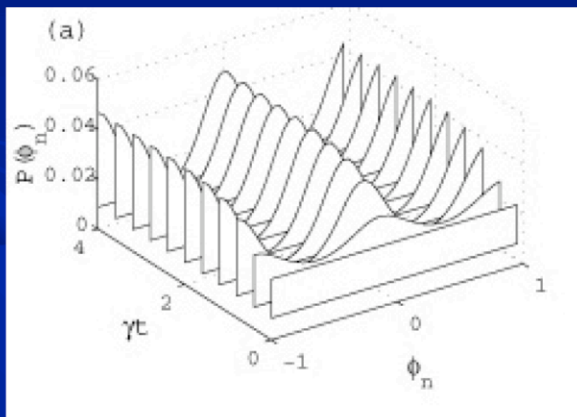
Molecule statistics as a function of  $\Theta$  for  $\_ = \eta = 0$  and  $N_{ex} = 50$

Next: Coherent control of molecular field...

# Tunneling \_Coupled molecular fields



Double-well trap potential



# SUMMARY

---

Think Fermions !

## **Conversion of a degenerate Fermi gas into molecules in a Feshbach resonance**

Juha Javanainen  
University of Connecticut

Presently, conversion of a degenerate gas into molecules in a Feshbach resonance and the attendant production of a molecular condensate are probably the most prominent topics in Atomic, Molecular and Optical physics. We investigate coherent, collisionless conversion by integrating the time dependent Schrodinger equation under the assumption that the bosonic molecules are treated as a classical field. In this framework the conversion from atoms to molecules emerges as a dynamical instability, a time-dependent counterpart of the thermodynamical instability responsible for BCS pairing in superconductors. We simulate numerically experiments on sweeps of the magnetic field across the Feshbach resonance. We find a semiquantitative agreement with the experiments, and predict that the initial temperature of the Fermi gas sets the limit on the efficiency of atom-molecule conversion.

# Conversion of an Atomic Fermi Gas to a Gas of Molecular Bosons

Kevin Strecker  
Andrew Truscott

Guthrie Partridge  
Ying-Cheng Chen

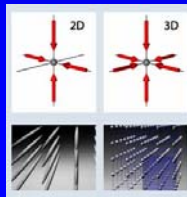


Kevin Strecker and Guthrie Partridge are the graduate students on this project.  
Andrew Truscott and Ying-Cheng Chen have worked on the project as post-docs.



# Ultracold Fermi Gases

- Building blocks of matter
  - The vast majority of the e, p, n on the moon and mars are fermions!
- Connections to condensed matter
  - Superconductivity (T-J model of high- $T_c$ )
  - Pseudo-gap
  - Lattices
  - Luttinger liquid, spin-charge separation, ...



Optical Lattices

Ultracold atoms obeying Fermi-Dirac statistics may be used to realize many of the paradigm models of condensed matter physics, including those of high temperature superconductivity. The purity of the gases, the ability to control defects in lattices created by interfering laser beams, and the fundamental simplicity of the interactions between atoms provide nearly ideal systems for fundamental measurements.

## BCS/Pairing Transition

- Cooper pairing
  - Superconductivity
  - Superfluidity  $^3\text{He}$
  - Dilute atomic gas?
- For  $s$ -wave pairing,  $T_c \cong T_F \exp(-1/k_F|a|)$  (BCS)
- For  $^2\text{H}$ ,  $a = -4 \text{ \AA} \Rightarrow T_c = 1 \text{ fK @ } 10^{19} \text{ cm}^{-3}$ 
  - Leggett (1980)
- For  $^6\text{Li}$ ,  $a = -1100 \text{ \AA} \Rightarrow T_c = 100 \text{ nK @ } 10^{13} \text{ cm}^{-3}$ 
  - Stoof *et al.* (1996)

Cooper pairing underlies superconductivity and superfluidity in fermions. Tony Leggett showed the direct  $s$ -wave pairing of atomic deuterium was not possible in a gas at reasonable temperatures due to its relatively small attractive interaction. However, Henk Stoof and I showed in 1996 that  $^6\text{Li}$  was a good candidate because of the extraordinarily large attractive interactions between atoms.

# Tunable Interactions

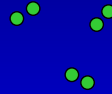
- Interactions variable for quantum gases

Weak coupling  
- BCS



BEC/BCS  
Crossover

Strong coupling -  
BEC of molecules



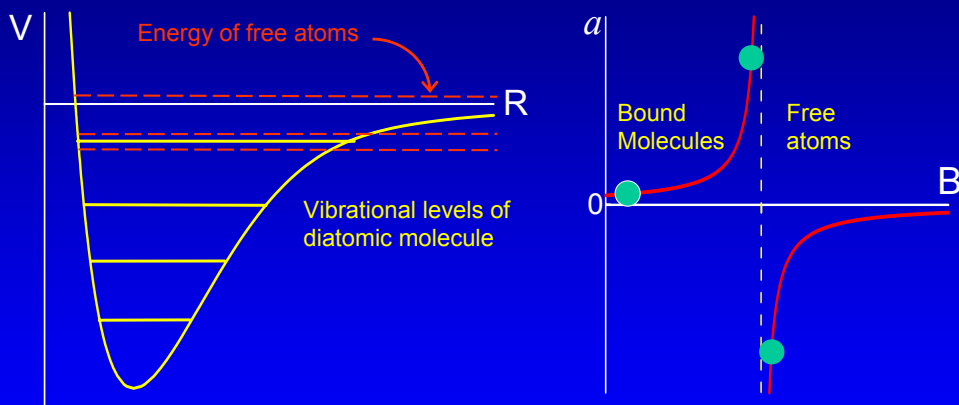
- BCS breaks down for strong or intermediate coupling:

$$k_F|a| \geq 1 \quad \text{or} \quad n|a|^3 \geq 1$$

(theory by M. Holland, E. Timmermans, and others)

Feshbach resonances can be used to vary the interaction strength and sign in atomic gases. This may enable the realization of atomic Cooper pairing in the weak coupling (BCS) limit, or in the strong coupling (BEC) limit.

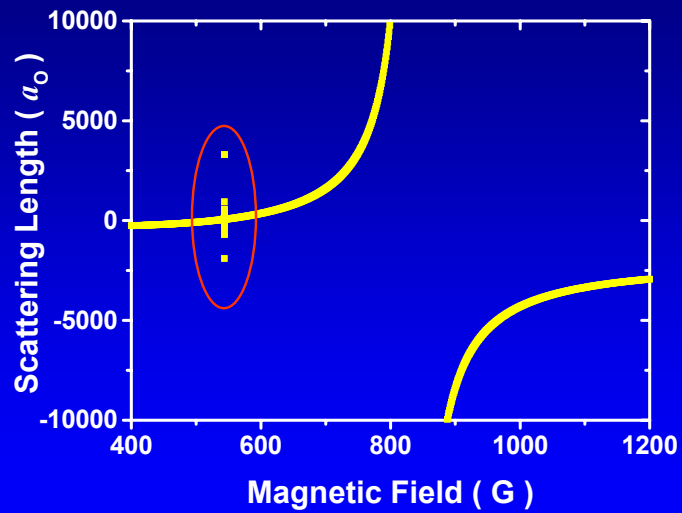
# Feshbach Resonance - Tunable Interactions



Magnetically tune dissociative state into resonance with a bound molecular state

Feshbach resonances are magnetically tuned collisional resonances. A magnetic field can differentially tune the energy of a pair of colliding free atoms and a bound vibrational state of the diatomic molecule. Right on resonance, the  $s$ -wave scattering length diverges. At higher fields, the last vibrational level becomes unbound and the scattering length is large and negative, corresponding to a large attractive interaction.

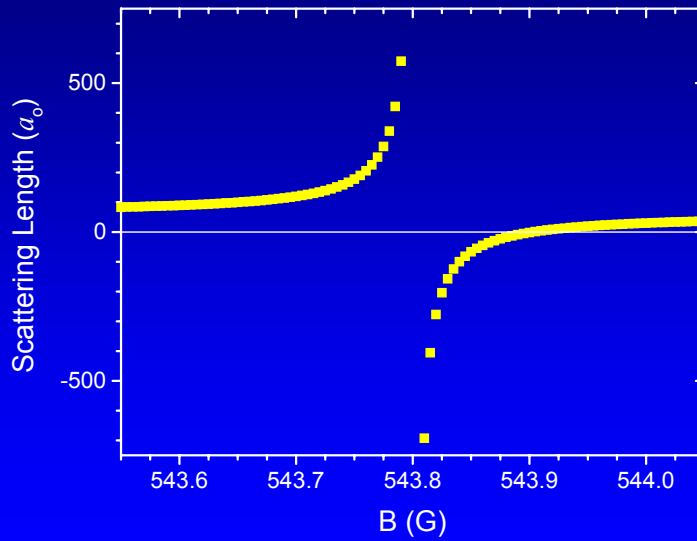
## Feshbach Resonance in ${}^6\text{Li}$



Houbiers, Stoof, McAlexander, Hulet, PRA **57**, R1497 (1998)  
O'Hara *et al.*, PRA **66** 041401 (2002)

This is a calculation of a Feshbach resonance in  ${}^6\text{Li}$ . There are actually two resonances shown here; the red circle indicates a narrow resonance at 543 G.

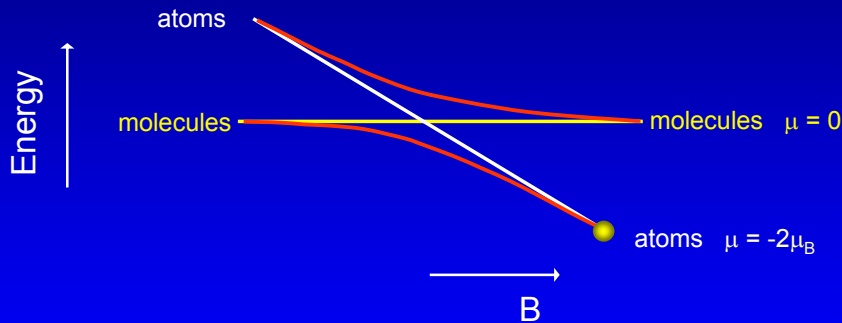
# Narrow Feshbach Resonance



This is a blow up of the resonance at 543 G. By ramping the magnetic field through this resonance, we create a gas of diatomic molecules from the original Fermi gas of atoms.

# Converting an Atomic Fermi Gas to a Molecular Bose Gas

Feshbach resonance:



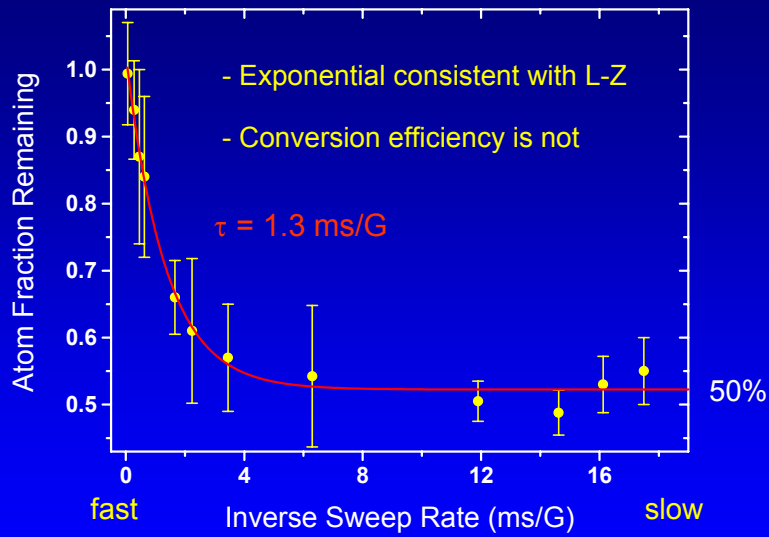
Landau-Zener theory: exponential dependence on inverse ramp rate

Theory: LANL, Eindhoven, NIST, Tel Aviv, UConn/Helsinki, Utrecht

Expts: JILA, Rice, Paris, Innsbruck, MIT

The process by which the atomic gas is associated into a gas of molecules is shown here. The molecules are in a spin singlet state and therefore, have no magnetic moment. The coupling between the atoms, which are spin triplet, and the molecules is due to the hyperfine interaction. Landau-Zener theory predicts that the conversion efficiency scales exponentially with the inverse ramp rate and is 100% when the ramp rate is sufficiently slow.

# Atoms Remaining vs. Ramp Rate

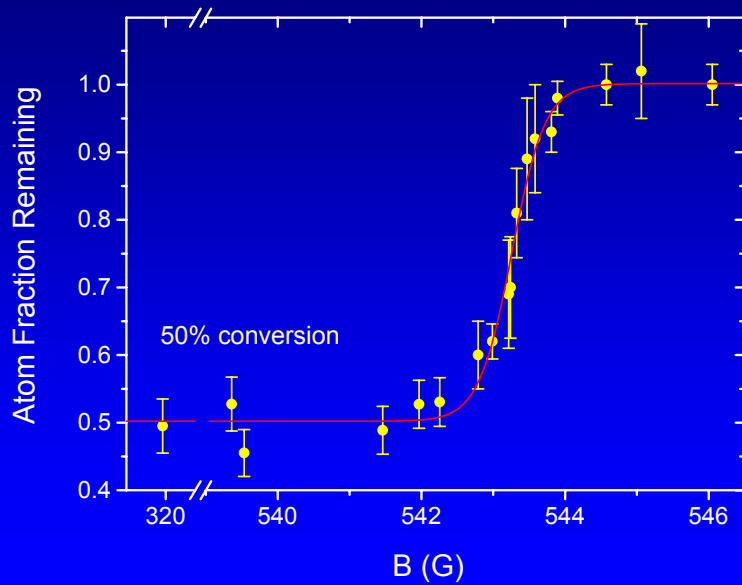


K.E. Strecker *et al.*, PRL 080406 (2003)

Experimentally, we observe an exponential dependence as predicted, but the maximum conversion efficiency is 50%.



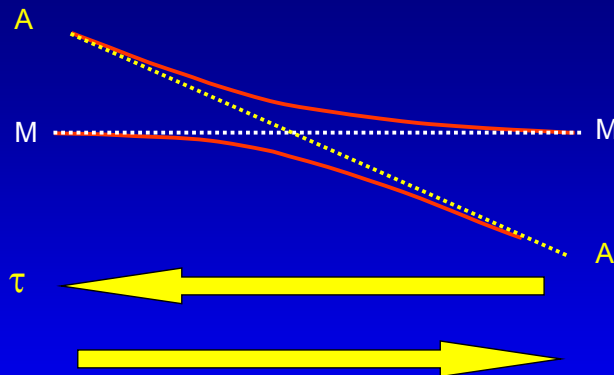
## Atoms Remaining vs. Final Field



K.E. Strecker *et al.*, PRL 080406 (2003)

The ramp is started at a high field of approximately 546 G. By stopping the ramp during the sweep, the Feshbach resonance can be mapped out. Again, the maximum conversion efficiency is 50%.

## 2-Way Ramp - Molecular Lifetime

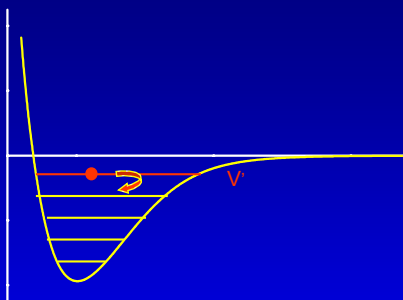


- Ramp field down – make molecules
- Wait time  $\tau$  - final field far from resonance  
(i.e. looking at deeply bound molecules)
- Ramp field back up – detect remaining atoms

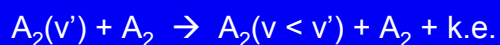
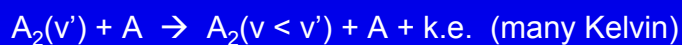
The data shown on the previous slides indicates that adiabatic passage through the Feshbach resonance causes atoms to be lost. However, it did prove that molecules are formed. We used a two-way ramp to demonstrate the production of molecules and to measure their lifetime. First, the molecules are created by ramping the field downward through resonance. The field is held there for a time  $\tau$  before ramping the field back through resonance, where surviving molecules are converted back to atoms.

# Limits to Molecular Lifetime

Molecules are vibrationally excited



Vibrational quenching collisions:

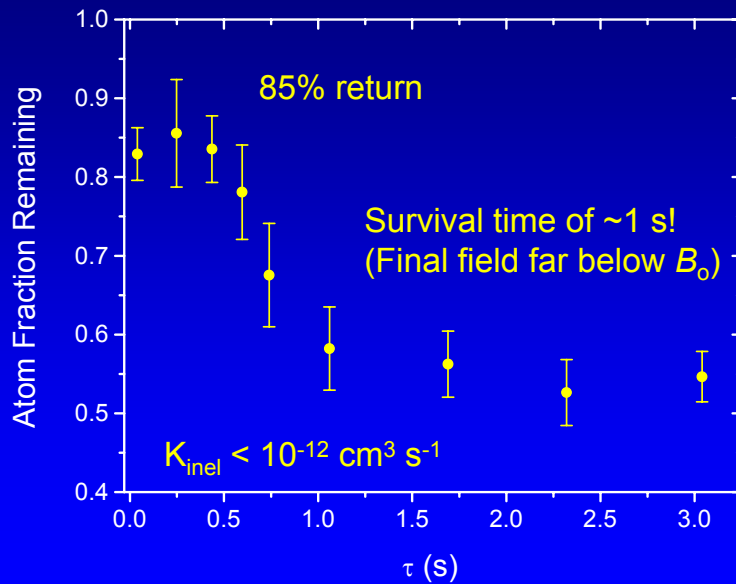


Heinzen *et al.* ( $^{87}\text{Rb}$ ), Ketterle *et al.* (Na)

Rate constant  $\sim 10^{-10} \text{ cm}^3/\text{s} \Rightarrow \sim 1 \text{ ms lifetime}$

The molecules produced by this method are vibrationally excited and are expected to be rapidly quenched to a lower lying vibrational level by collisions with other atoms and molecules. Rate constants for this mechanism have been measured to be  $\sim 10^{-10} \text{ cm}^3 \text{ s}^{-1}$  for bosons.

## 2-Way Ramp - Molecular Lifetime



K.E. Strecker *et al.*, PRL 080406 (2003)

The data show that most of the molecules are converted back to atoms as long as  $\tau$  is sufficiently small. To our surprise, we found that the molecular lifetime is  $\sim 1$  s, corresponding to a rate constant that is more than a factor of 100 smaller than for bosonic atoms.

## Molecular BEC

- Long lifetime enables formation of condensate
- We have produced a molecular BEC by evaporation (also Innsbruck, JILA, MIT, Paris; evidence for superfluidity at Duke)
- MBEC with fermions can be considered Cooper pairing in *extreme* strong coupling limit

The long lifetime enables the formation of a Bose-Einstein condensate by evaporation. We have produced a molecular BEC by evaporation of molecules produced on the broad Feshbach resonance. These Bose condensed molecules can be considered to be Cooper pairs in the extreme strong coupling limit.

## Summary

- $10^5$   $\text{Li}_2$  molecules created
- Estimate that initial phase space density  $\sim 0.5$
- Long lifetime (1 s) enabled formation of a molecular BEC
- Next: Direct imaging of deeply bound molecules to explore role of deeply bound molecules in BEC/BCS crossover

In summary, we created approximately  $10^5$   $\text{Li}_2$  molecules in the  $v=38$  singlet state. Initially, the molecules are formed with a phase space density of about half of that required for BEC. However, the molecules evaporate from the shallow optical trap on the time scale of a few hundred ms, and the phase space density may increase. The formation of the condensate may explain the unusual shape of the molecular lifetime shown in the 2-way ramp data. The unexpectedly long molecular lifetime enabled the formation of a molecular Bose-Einstein condensate. We are currently attempting to directly image the deeply bound molecules and to study their role in the BCS/BEC crossover.

# Recent results with ultracold gases

Erik Streed

Ketterle-Pritchard Group

Massachusetts Institute of Technology  
MIT-Harvard Center for Ultracold Atoms




April 21, 2004

2004 NASA/JPL Workshop on Physics for Planetary Exploration  
Solvang, California

# Overview

- Record Low Temperature
- Zero clock shift in Fermions
- Atom Chips
- Atom Interferometry
- Raman Matter Wave Amplifier
- BEC of molecules
  - From condensed Bosons
  - From cold Fermions





MEDIA | ABOUT GWR | CONTACT US

**FIND A WORLD RECORD**

leanhardt **GO**

Enter keywords separated by a space  
e.g., pogo stick, longest fingernails

**BE A RECORD BREAKER**

FAQs **GO**

HUMAN BODY   AMAZING FEATS   NATURAL WORLD   SCIENCE & TECH   ARTS & MEDIA   HI & S

SCIENCE AND TECHNOLOGY << AMAZING SCIENCE << LOWEST TEMP

## Lowest Manmade Temperature


The lowest manmade temperature achieved so far is 450 picokelvin. It was achieved by a team of scientists at the Massachusetts Institute of Technology in Cambridge, Massachusetts, USA: A.E. Leanhardt, T.A. Pasquini, M. Saba, A. Schirotzek, Y. Shin, D. Kielpinski, D.E. Pritchard and W. Ketterle. The results were published in *Science* magazine on September 12, 2003.

**WHO:** Aaron Leanhardt & team

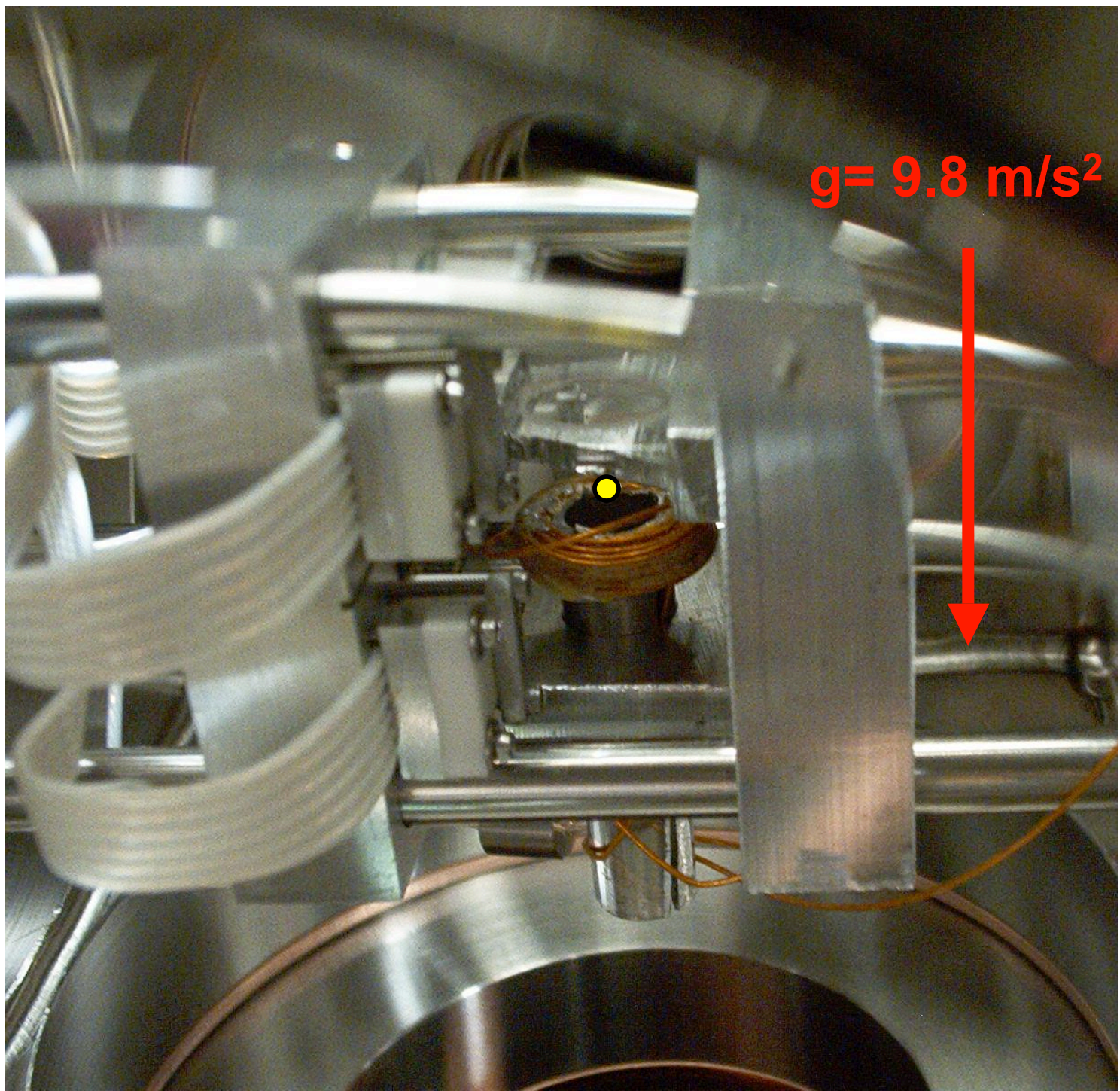
**WHEN:** Results published Sept 12, 2003

**WHERE:** MIT, Massachusetts, USA

**WHAT:** 450 picokelvin above zero K

 **Send to a friend**

A.E. Leanhardt, T.A. Pasquini, M. Saba, A. Schirotzek, Y. Shin, D. Kielpinski, W. Ketterle, and D.E. Pritchard, *Science* 301 p. 1513 (2003).





# Cooling Bose-Einstein condensates below 500 picokelvin

## Low density and low temperature

- Cooled partially condensed atomic vapors to  $450 \pm 80$  pK.
- Peak condensate densities  $\sim 5 \times 10^{10} \text{ cm}^{-3}$
- Thermal velocity  $\sim 1 \text{ mm/s}$
- Speed of sound  $\sim 100 \text{ } \mu\text{m/s}$
- Healing length  $\sim 20 \text{ } \mu\text{m}$
- Mean field energy  $\sim k_B \times 33 \text{ pK} \sim h \times 0.7 \text{ Hz} \sim (\mu_B/2) \times 1 \text{ } \mu\text{G}$

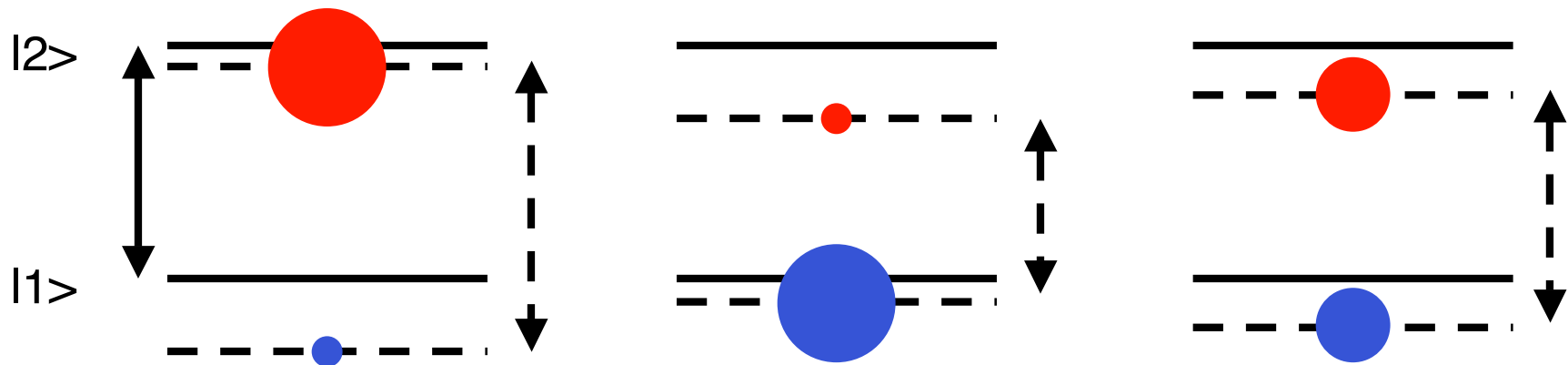
## Applications

- Precision measurements with reduced density-dependent line shifts
- Ultracold atom source for atom optics
- Surface reflection of ultracold atoms

# Overview

- Record Low Temperature
- • Zero clock shift in Fermions ←
- Atom Chips
- Atom Interferometry
- Raman Matter Wave Amplifier
- BEC of molecules
  - From condensed Bosons
  - From cold Fermions

# Clock shifts\*



$$E_{\text{int}} = V_{12} n_1 n_2 \quad V_{12} = \frac{4\pi\hbar^2 a_{12}}{m} < 0$$

$$h\Delta\nu = V_{12}(n_1 - n_2)$$

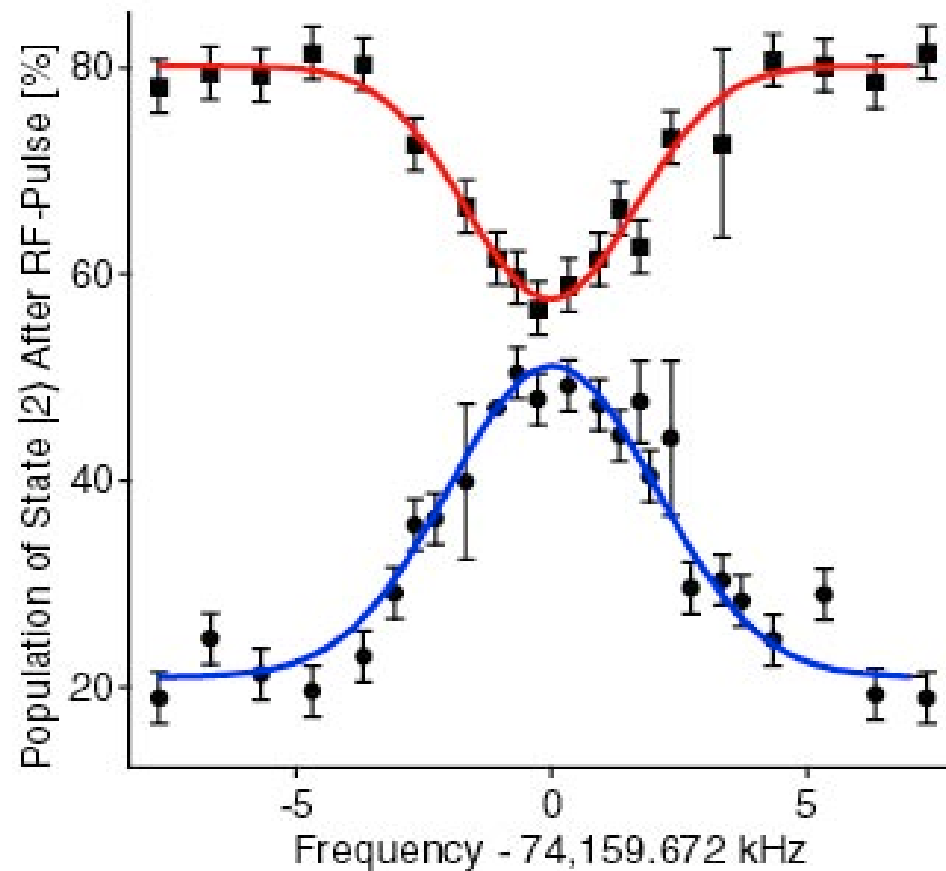
Get  $V_{12}$  from  $n_1=0$  and  $n_2=0$  measurements

\* This effect limits the accuracy of the (bosonic) atomic clocks

# No clock shift in a degenerate Fermion mixture

“Expected” splitting  
of the lines:  
~20 kHz

The system **is**  
interacting, but still  
no shift...

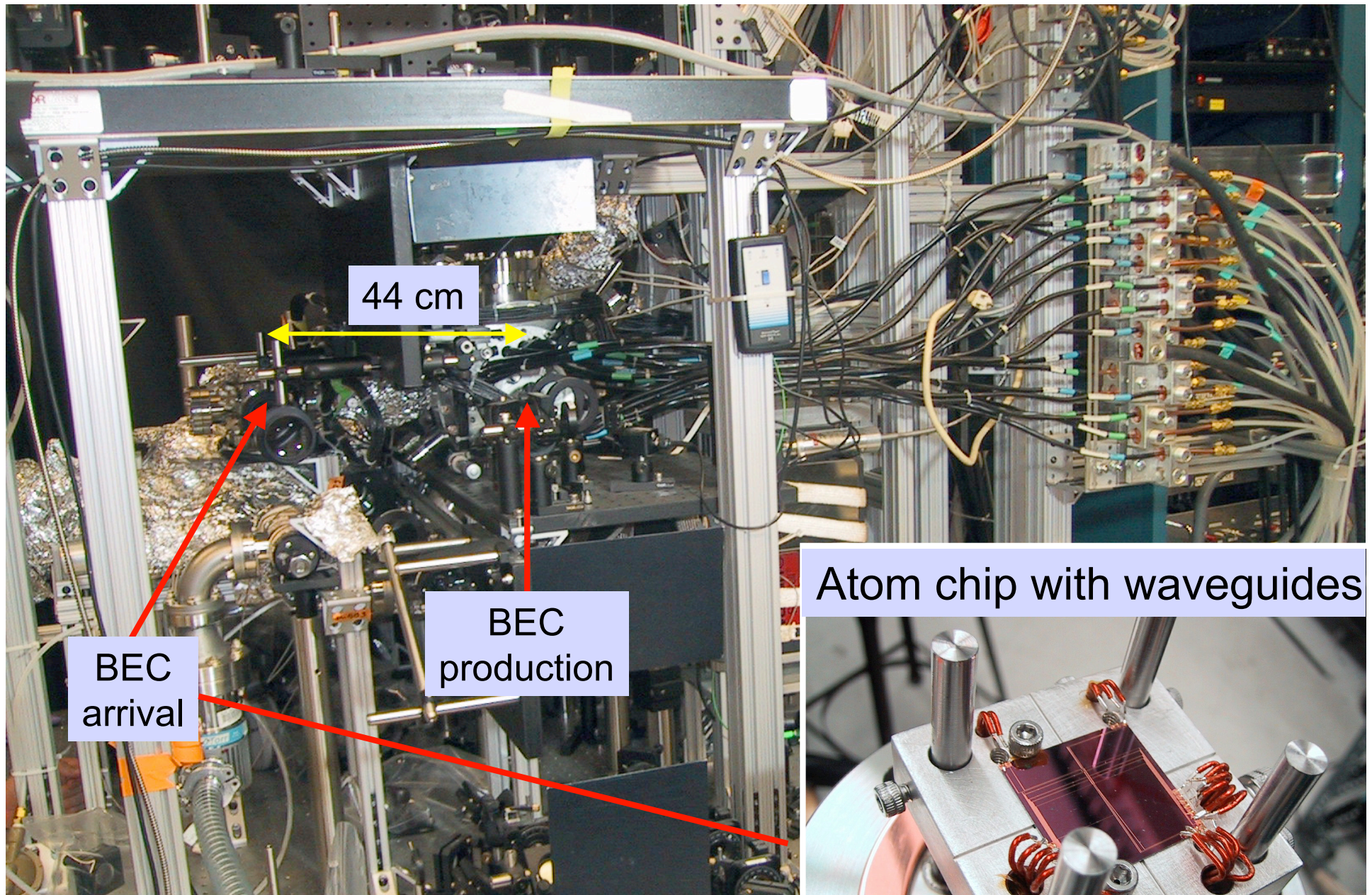


Martin W. Zwierlein, Zoran Hadzibabic, Subhadeep Gupta,  
Wolfgang Ketterle, PRL 91, 250404 (2003)

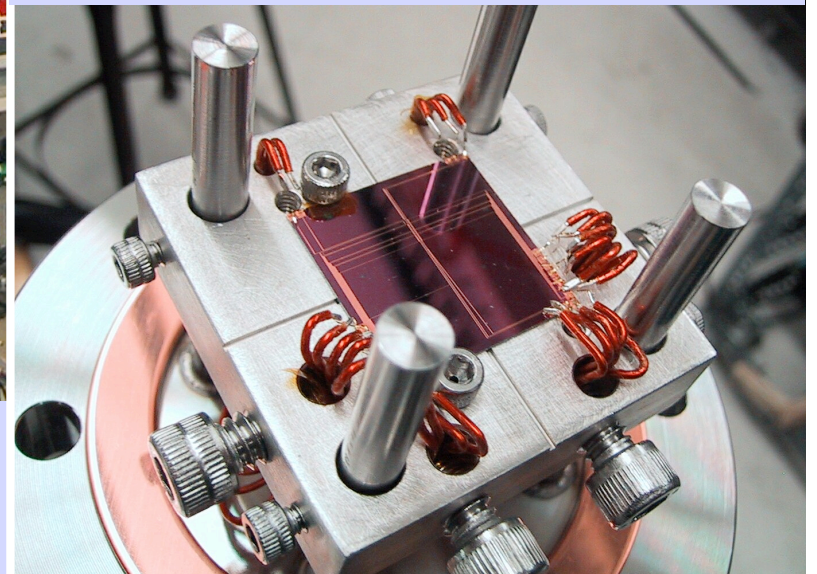
# Overview

- Record Low Temperature
- Zero clock shift in Fermions
- • Atom Chips ←
- Atom Interferometry
- Raman Matter Wave Amplifier
- BEC of molecules
  - From condensed Bosons
  - From cold Fermions





Atom chip with waveguides



T.L.Gustavson, A.P.Chikkatur, A.E.Leanhardt,  
A.Görlitz, S.Gupta, D.E.Pritchard, W. Ketterle,  
Phys. Rev. Lett. **88**, 020401 (2002).

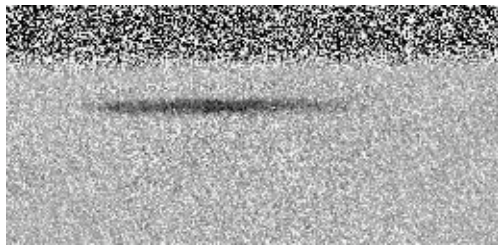


Analogy:

Atoms in magnetic wave guides - Light in optical fibers

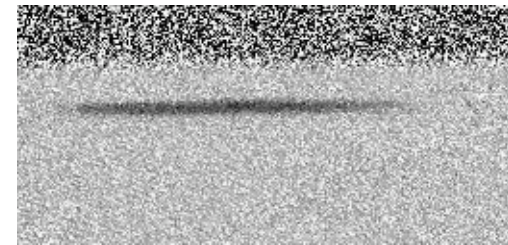
## Excitationless (“single-mode”) propagation

Initially



← 2 mm →

After 100 ms and 4 mm  
(speed ~ 4 cm/s)



← 2 mm →

$\omega_{\text{radial}} \sim 2\pi \times 600 \text{ Hz}$ ,  $r_{\text{surface}} \sim 200 \text{ }\mu\text{m}$ ,  $N \sim 10^6$ , 5 ms TOF

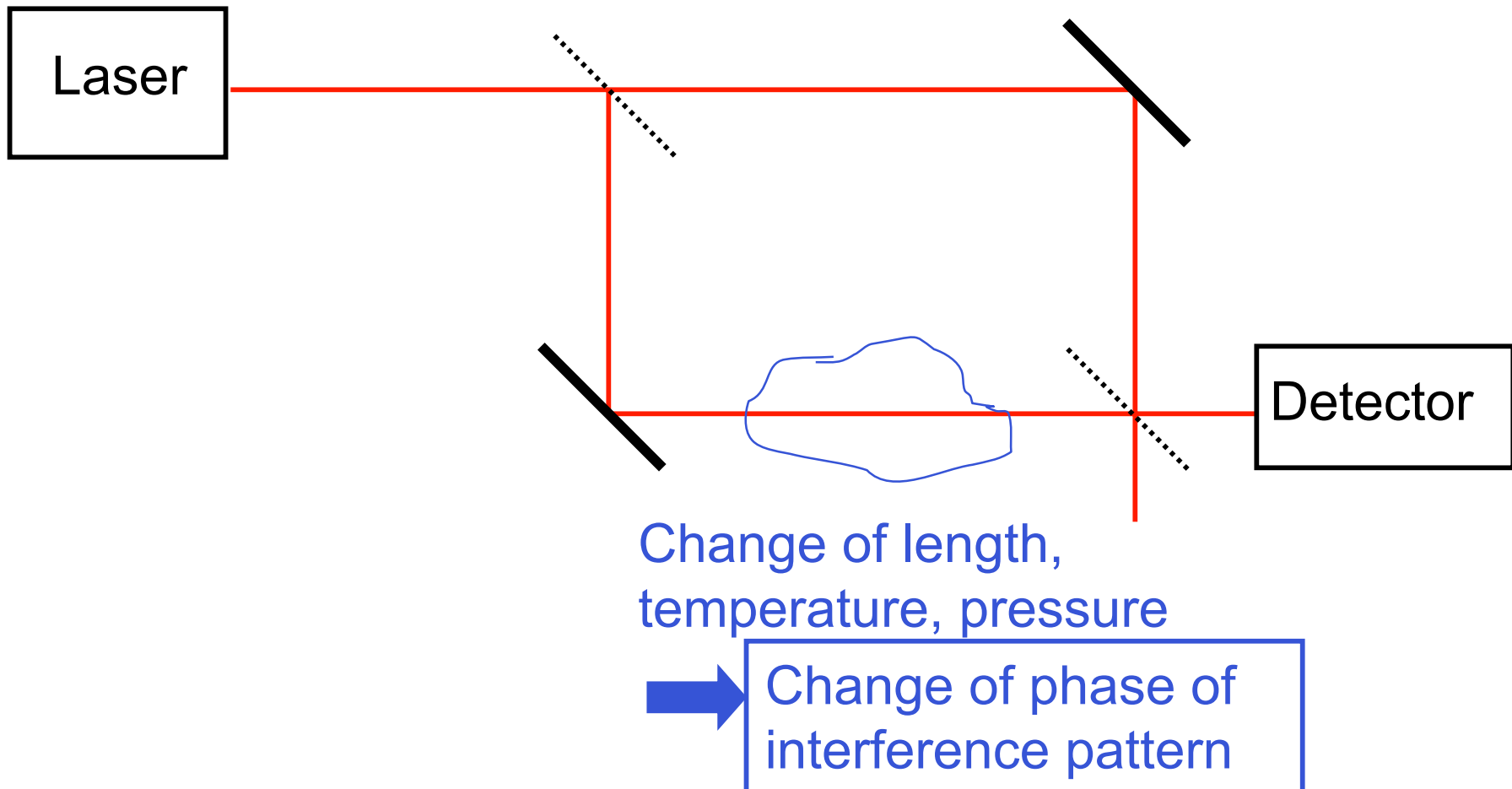
A.E. Leanhardt, A.P. Chikkatur, D. Kielpinski, Y. Shin, T.L. Gustavson,  
W. Ketterle, and D.E. Pritchard, Phys. Rev. Lett. 89, 040401 (2002).

# Overview

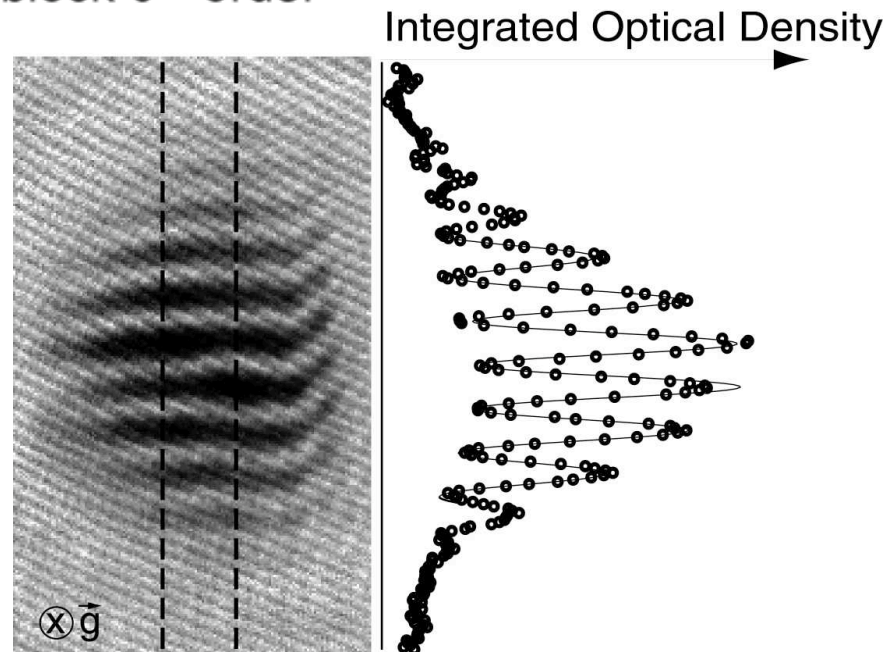
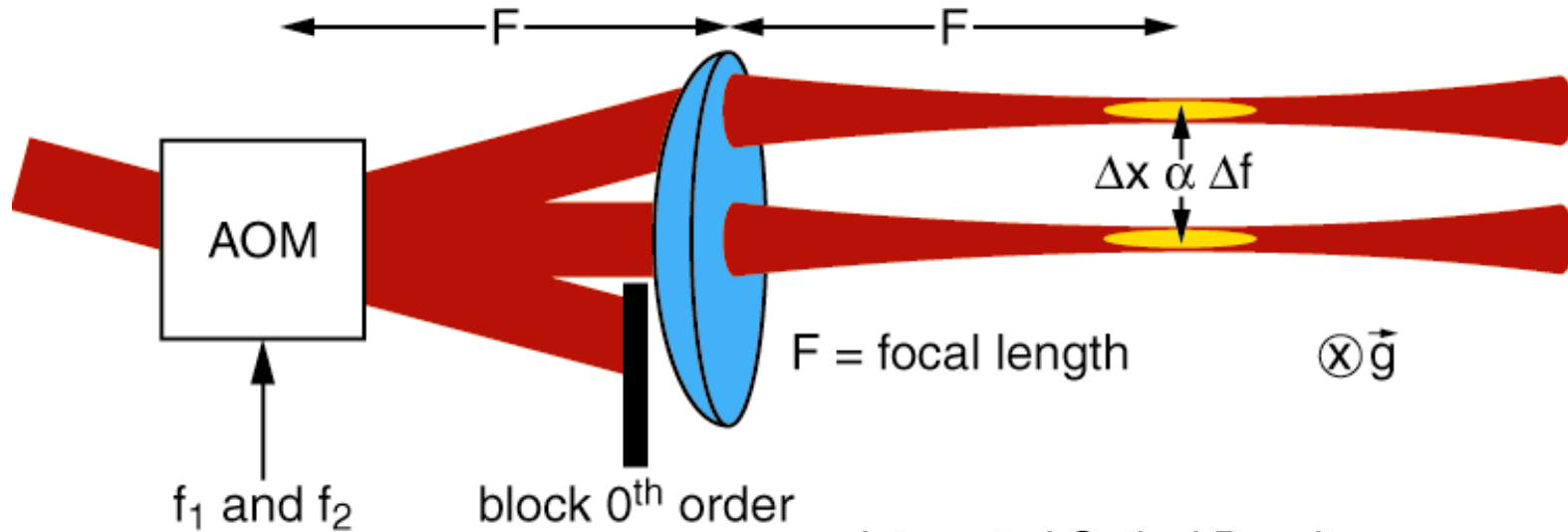
- Record Low Temperature
- Zero clock shift in Fermions
- Atom Chips
- • Atom Interferometry ←
- Raman Matter Wave Amplifier
- BEC of molecules
  - From condensed Bosons
  - From cold Fermions

# Goal: Atom interferometry on a chip

Optical precision measurements using interferometry:



# Atom Interferometry with two BECs

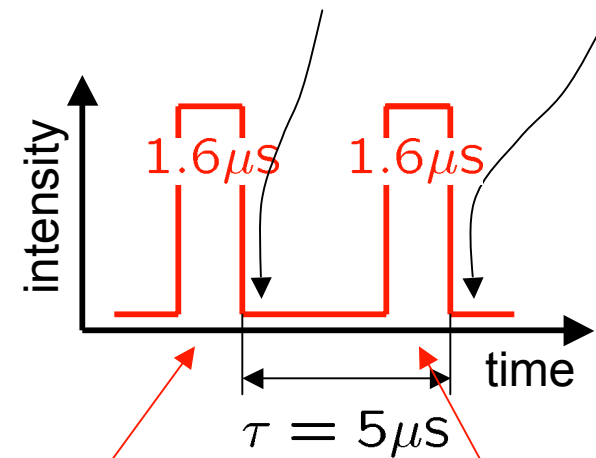
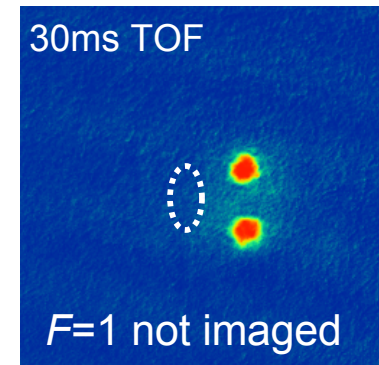
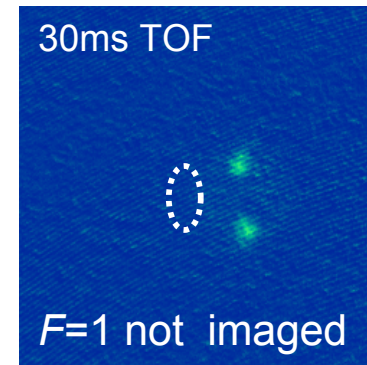
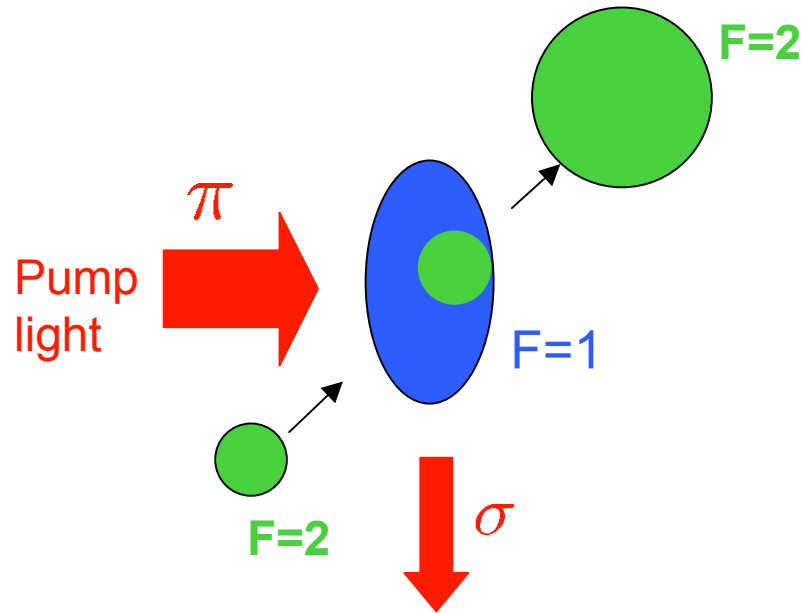


Y. Shin, M. Saba, T. Pasquini, W. K., D.E. Pritchard, A.E. Leanhardt, Phys. Rev. Lett. **92**, 050405 (2004).

# Overview

- Record Low Temperature
- Zero clock shift in Fermions
- Atom Chips
- Atom Interferometry
- • Raman Matter Wave Amplifier ←
- BEC of molecules
  - From condensed Bosons
  - From cold Fermions

# Raman Matter Wave Amplification



Input  
preparation

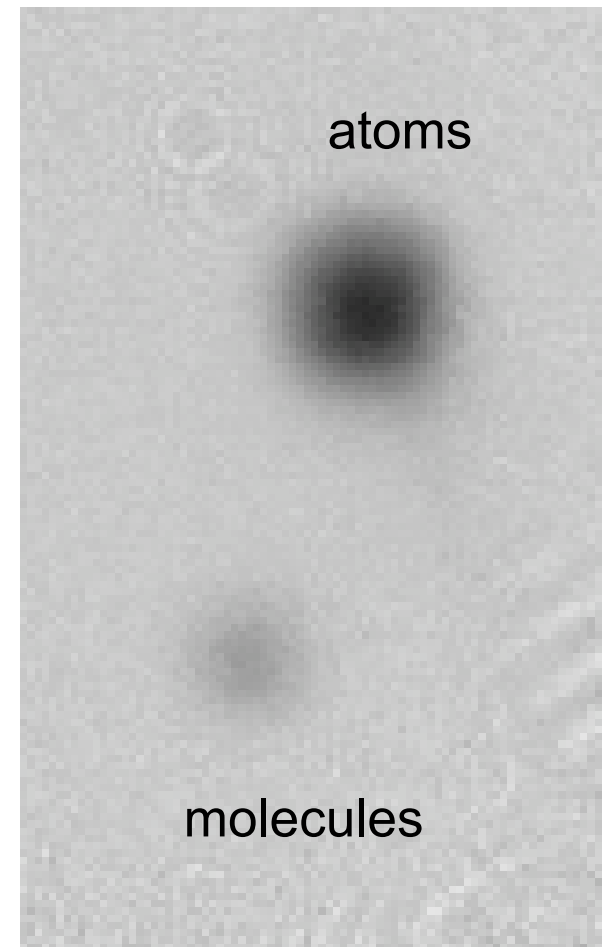
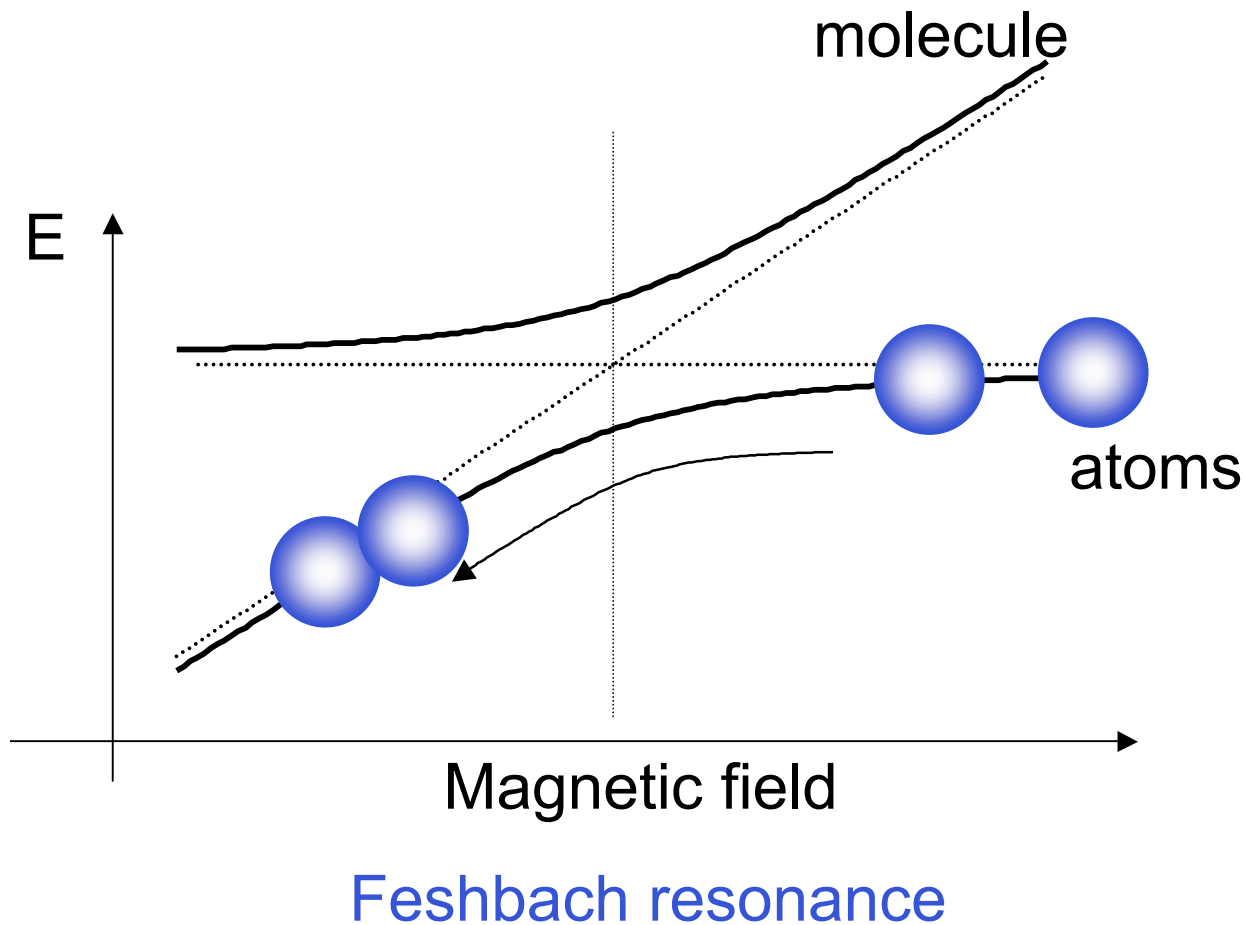
Amplification  
of input

Dominik Schneble, Gretchen Campbell,  
Erik Streed, Micah Boyd, DP, WK.  
PRA 69 041601 (2004)

# Overview

- Record Low Temperature
- Zero clock shift in Fermions
- Atom Chips
- Atom Interferometry
- Raman Matter Wave Amplifier
- • BEC of molecules ←
  - From condensed Bosons
  - From cold Fermions

# Feshbach Resonance For Molecule Formation



Bosons: Boulder, Garching, Innsbruck, MIT

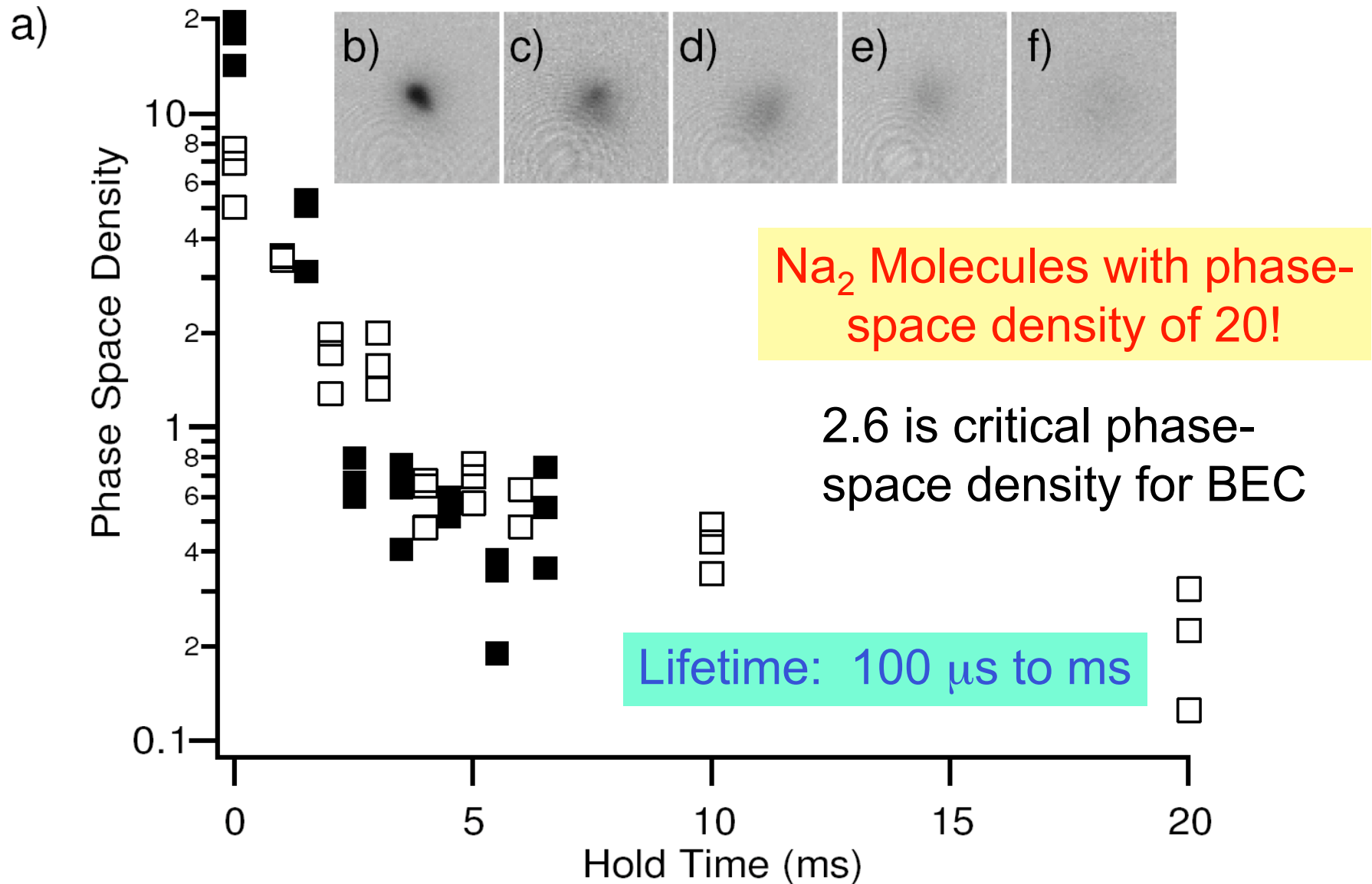
Fermions: Boulder, Rice, Paris, Innsbruck, MIT



# Overview

- Record Low Temperature
  - Zero clock shift in Fermions
  - Atom Chips
  - Atom Interferometry
  - Raman Matter Wave Amplifier
  - BEC of molecules
- – From condensed Bosons ←
- From cold Fermions

# Coherent Na atoms to coherent Na<sub>2</sub> molecules

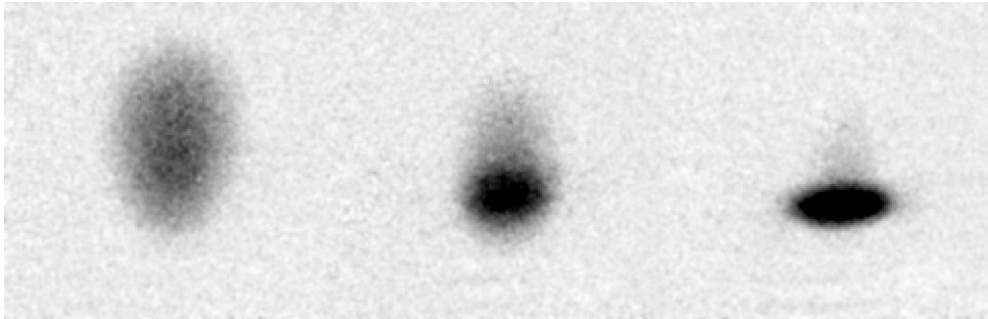


Takashi Mukaiyama, Kaiwen Xu, Jamil Abo-Shaeer, Jit Kee Chin, Daniel Miller, W.K.  
Phys. Rev. Lett. **91**, 210402 (2003)

# Overview

- Record Low Temperature
- Zero clock shift in Fermions
- Atom Chips
- Atom Interferometry
- Raman Matter Wave Amplifier
- BEC of molecules
  - From condensed Bosons
  - – From cold Fermions ←

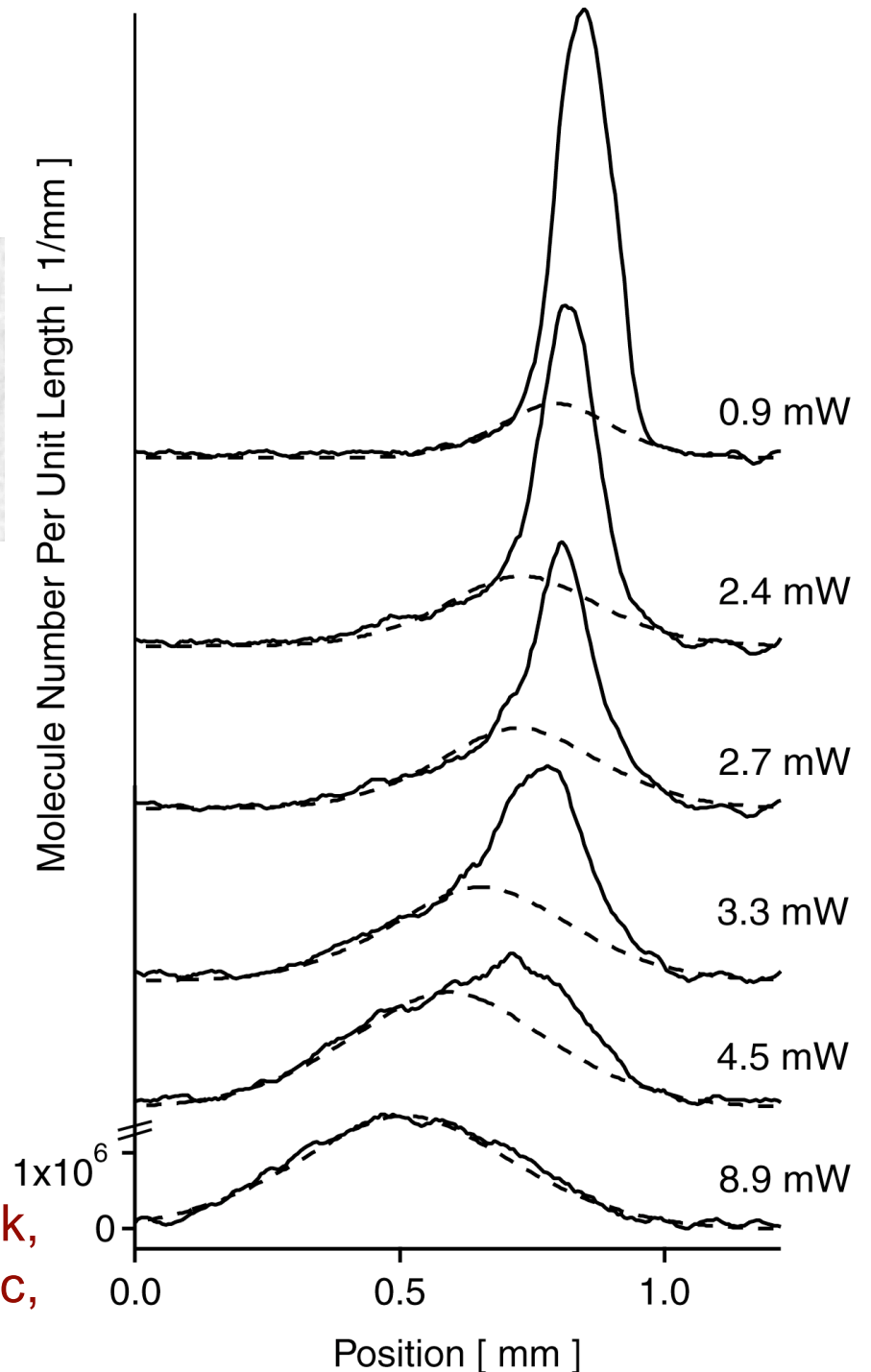
# BEC of $\text{Li}_2$ Molecules



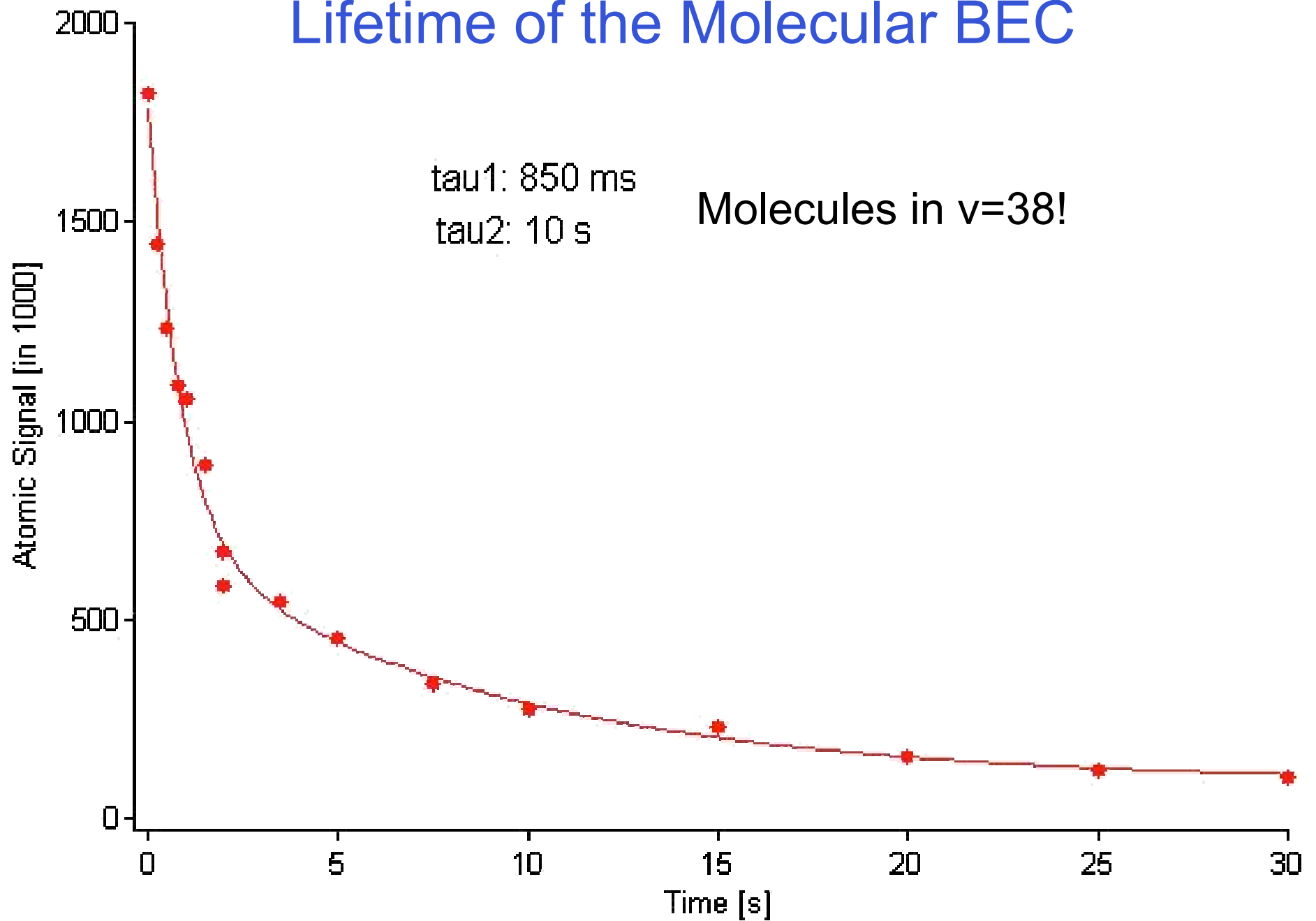
Up to 3 million condensed molecules

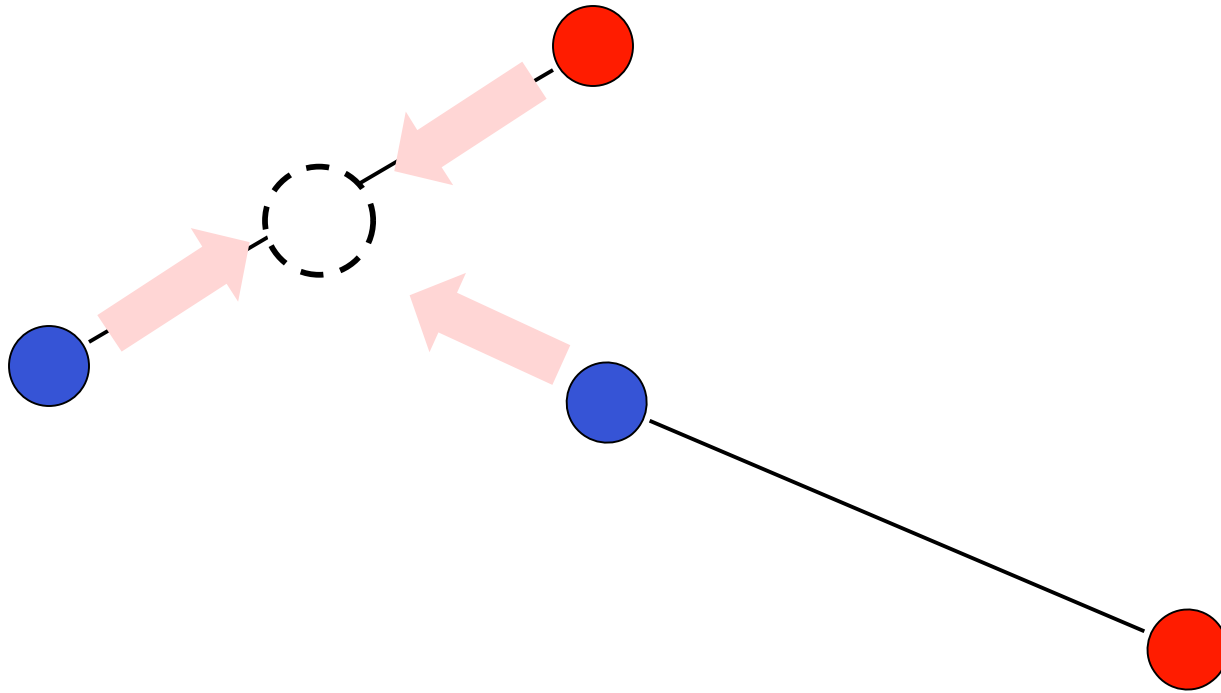
Boulder	Nov '03
Innsbruck	Nov '03, Jan '04
MIT	Nov '03
Paris	March '04

M.W. Zwierlein, C. A. Stan, C. H. Schunck, S.M. F. Raupach, S. Gupta, Z. Hadzibabic, W.K., Phys. Rev. Lett. 91, 250401 (2003)



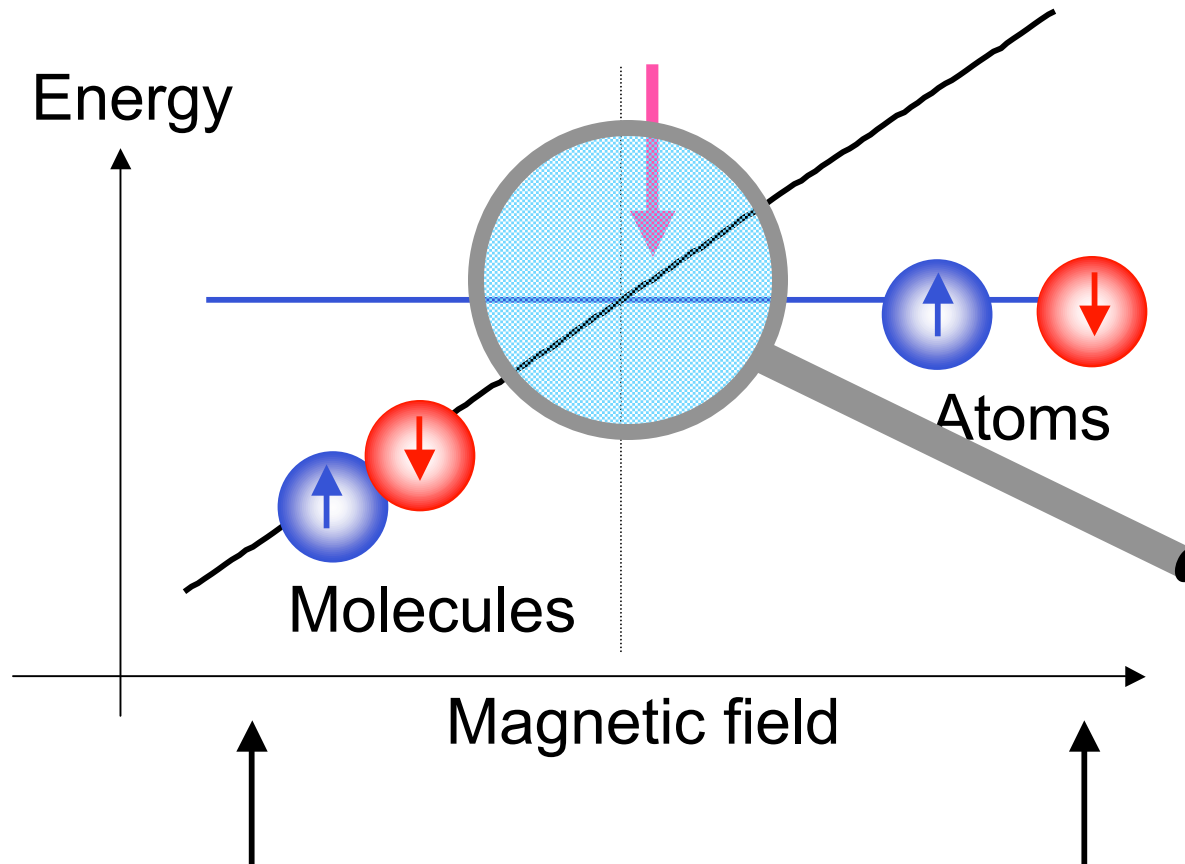
# Lifetime of the Molecular BEC





Reason for suppression of inelastic collisions: **Pauli principle**  
Three atoms can't be at the same point at the same time

Two would have same location and spin state!



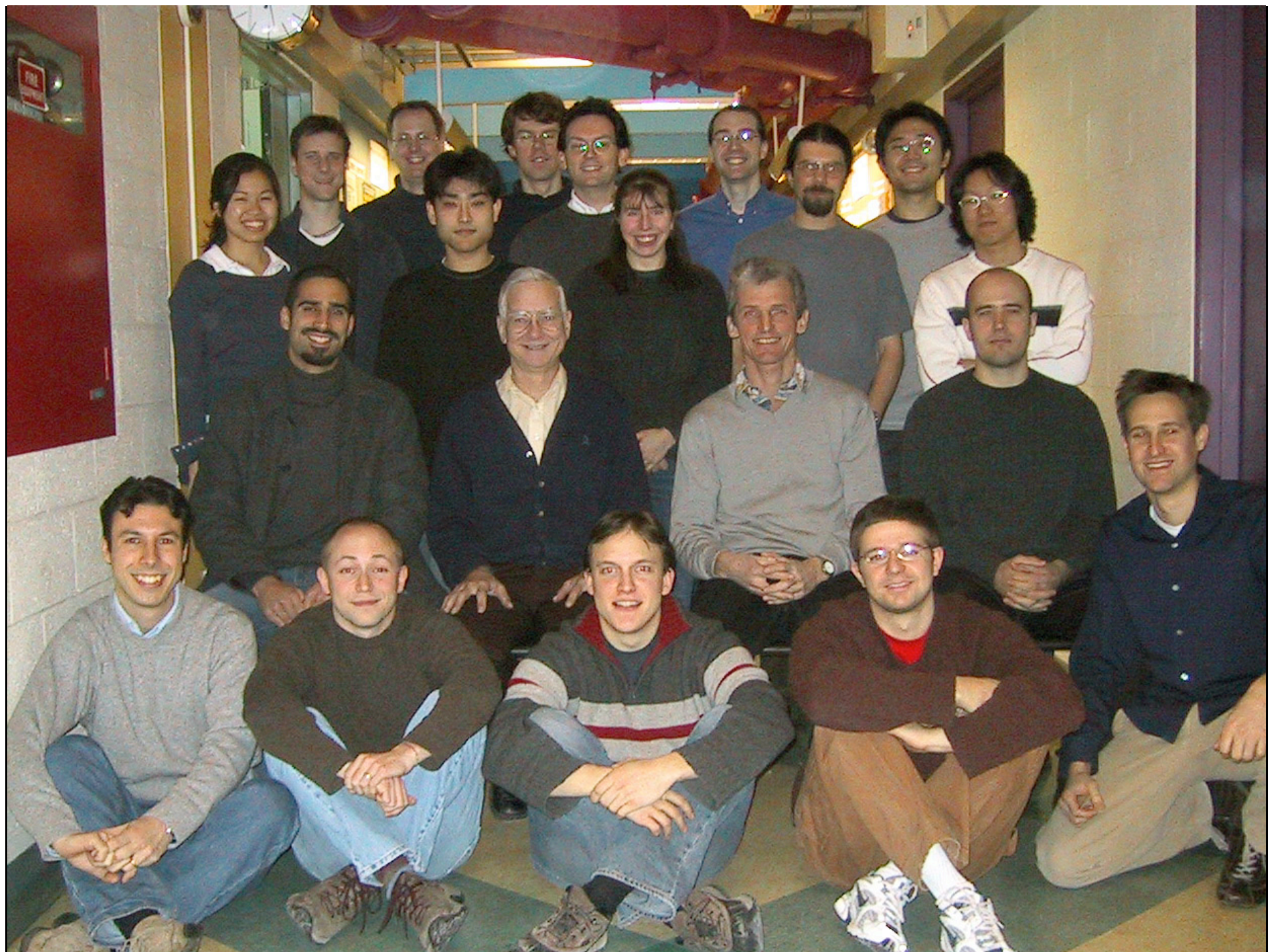
Atoms form stable molecules

Molecules are unstable

**Atoms repel each other**  
 **$a > 0$**

**Atoms attract each other**  
 **$a < 0$**







## BEC I

Ultracold  
fermions

Claudiu Stan  
Martin Zwierlein  
Christian Schunck  
Jamie Kerman  
Sebastian Raupach

\$\$

NSF  
ONR  
ARO  
NASA  
DARPA

## BEC II

Na<sub>2</sub> molecules  
Condensed  
matter physics  
with BECs

Jamil Abo-Shaeer  
Kaiwen Xu  
Jit Kee Jin  
Daniel Miller  
Takashi Mukaiyama

## BEC III

Atom chips,  
surface atom  
optics

Yong-Il Shin  
Tom Pasquini  
Michele Saba  
Andre Shirotzek  
Christian Sanner  
**D.E. Pritchard**

## BEC IV

Atom optics  
and lower  
dimensions

Micah Boyd  
Erik Streed  
Gretchen Campbell  
Jongchul Mun  
Dominik Schneble  
Aaron Leanhardt  
**D.E. Pritchard**

## **Resonance superfluidity in dilute fermion gases**

Murray Holland  
JILA and University of Colorado

In the field of dilute quantum gases, there is currently a significant experimental and theoretical effort ongoing to pursue the remarkable physics of resonant superfluids. In particular the ability to use Feshbach resonances to control interactions between the atoms opens up many nontrivial avenues for future research. A few topics include the development of techniques for the production of molecular condensates, the investigation of high-temperature fermion superfluidity believed to have connections with high temperature superconductors, the realization of quantum Hall physics in these systems, and connections with the physics of reduced dimensionality.

This problem is particularly relevant to the description of the crossover from the theory of Bose-Einstein condensation, where the scattering length is positive and small, to that of fermion superfluidity (as in weak or strong coupling superconductors), where the scattering length is negative and small. This crossover can be realized in atomic gases by Feshbach resonances by changing the strength of a magnetic field through the resonant value. To understand these things theoretically, it is necessary to bridge the regime of infinite scattering length which lies in the crossover in such a way as to correctly interpolate between the correct equations of state on both sides of the resonance. This would allow a robust connection to be made between two seminal concepts in physics: superfluid bosons and superfluid fermions. I will present our recent results on the systematic development of such a quantitative theory in which these aspects are investigated.

# Hydrodynamics in a Degenerate, Strongly Attractive Fermi Gas



John E. Thomas

Department of Physics, Duke University

**Students: Joseph Kinast, Staci Hemmer,**

**Post Doc: Andrey Turlapov**

**Ken O'Hara\*, Mike Gehm\*,  
Stephen Granade\***

**Sponsored by: NASA (also DOE, NSF, ARO)**

# Outline

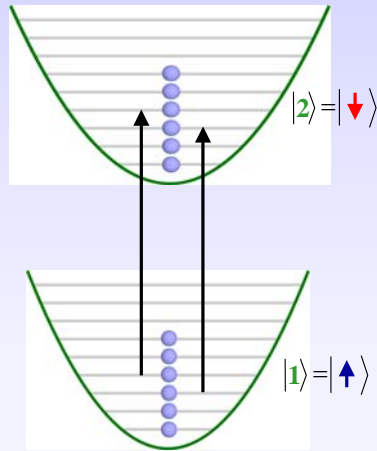


- Degenerate Fermi Gases
- All-Optical Cooling Method
- Hydrodynamic Expansion
- Evidence for Superfluid Hydrodynamics
- Conclusions

We begin by reviewing the reasons for interest in degenerate Fermi gases, both noninteracting and strongly interacting. Then we describe our all-optical cooling and trapping method for creating the samples. Finally, we describe our observations of hydrodynamic expansion of the gas, and evidence for superfluid hydrodynamics in the trapped gas.

# Trapped Degenerate Fermi Gases

## Hyperfine Transitions in an Optical Trap



Fermions in **Same** Superposition  
State are Noninteracting  
(Gibble and Verhaar)

Fermionic atoms in the same superposition of hyperfine spin states are noninteracting. For this reason, fermionic atoms have potential applications in new atomic clocks where interactions are suppressed.

# Strongly-Interacting Fermi Gases Mimic Exotic Systems in Nature



## A BUNCH OF DEGENERATES

A degenerate gas of fermions occurs in diverse situations, as described below:

### ■ Superconductors:

The electrons are degenerate and form loosely correlated Cooper pairs, which produce the superconductivity. Something similar must happen in high-temperature superconductors, but that process remains a mystery.

■ **Neutron stars:** The refusal of neutrons (which are fermions) to occupy identical quantum states generates a repulsion that prevents the star from collapsing under its own immense weight. A similar repulsion stabilizes the laboratory-made degenerate fermi gases against collapse.

- High-Temperature Superconductors
- Neutron Stars
- Strongly-Interacting Matter
- Quark-Gluon Plasma – Elliptic Flow

### ■ Quark-gluon plasma:

As created at the Relativistic Heavy Ion Collider at Brookhaven National Laboratory, the exploding cloud of free quarks (which are fermions) and gluons has properties similar to a gas of fermionic atoms released from the confines of a trap.

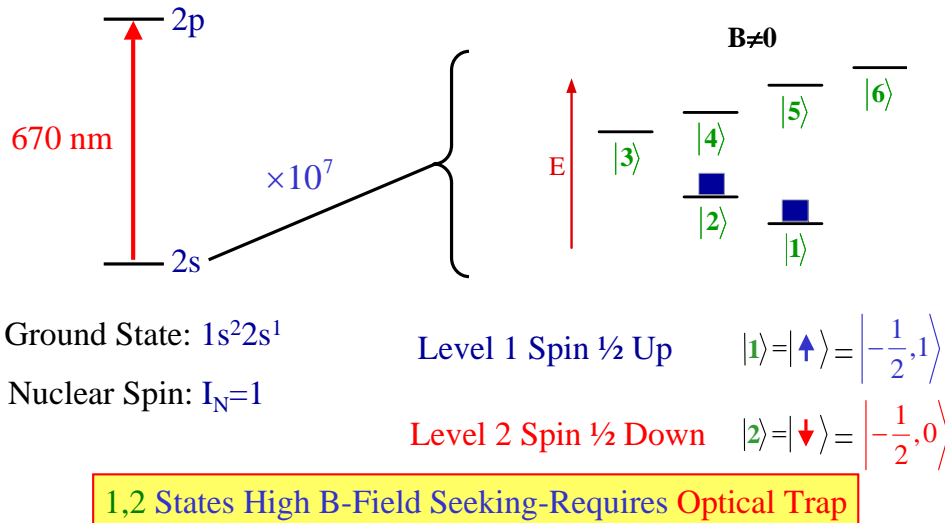
26 SCIENTIFIC AMERICAN

Fermionic atoms also can be made to interact strongly by exploiting a Feshbach resonance. In this case, a gas comprised of strongly interacting spin-up and spin-down atoms mimics a variety of exotic systems in nature, ranging from high temperature superconductors to nuclear matter. The elliptic flow exhibited by a quark-gluon is closely related to the anisotropic hydrodynamic expansion of a mixture of strongly interacting spin-up and spin-down atoms.

# Mixture of Spin Up/Down ${}^6\text{Li}$ Atoms



## Ground State Hyperfine Structure in a Magnetic Field $B$

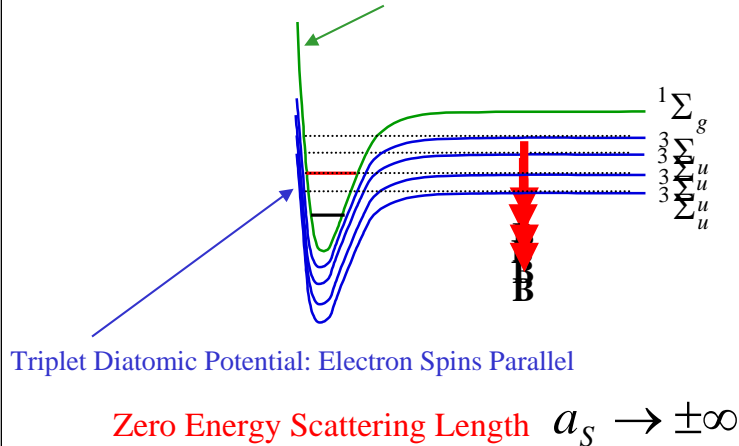


We employ lithium-6 atoms in a 50-50 mixture of the two lowest hyperfine states in a magnetic field. The spin-up and spin-down states have the same electron spin down and different nuclear spin. Both states are repelled from magnetic traps and require optical traps for study.

# Controlling Interactions with a Feshbach Resonance

Resonant Coupling between Colliding Atom Pair – Bound Molecular State

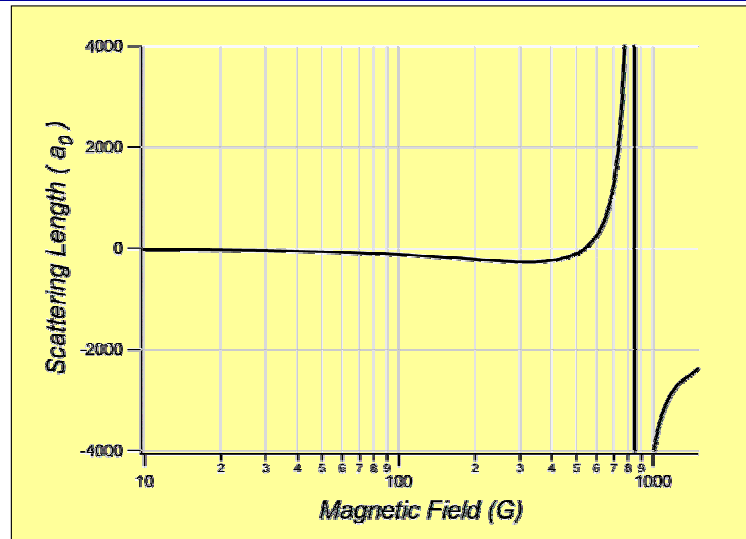
Singlet Diatomic Potential: Electron Spins Not Parallel



Strong, magnetically tunable interactions are produced using a Feshbach resonance. Normally, a pair of lithium atoms forms a diatomic molecule in the singlet electronic state (green), where the electron spins are not parallel. One diatomic molecular state is shown in red. However, the trapped states have parallel electron spins, and therefore collide in a triplet electronic state (blue). Normally, the atoms approach each other and bounce off of the potential inner wall. However, by tuning an applied magnetic field, the total energy of the colliding atoms can be tuned, because the triplet state has a magnetic moment. When the total energy of the colliding pair coincides with the energy of the bound molecular state in the singlet potential, the molecular amplitude becomes large, causing the scattering length to increase. The scattering length at zero energy determines the distance over which the wavefunction of the colliding atoms is modified.



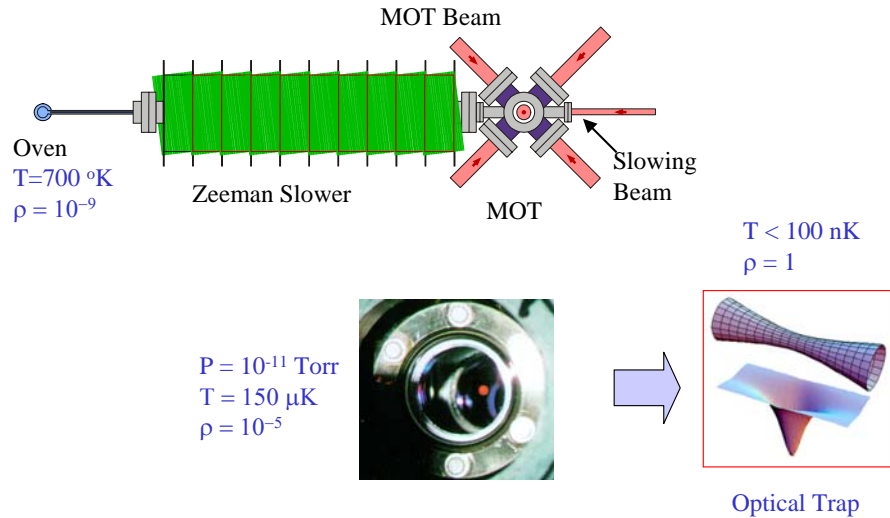
## \*Feshbach Resonance for 1-2 Mixture



\*M. Houbiers, *et al.*, Phys. Rev. A **57**, 1497 (1998)

The scattering length is plotted as a function of magnetic field. Near 850 G, there is a resonance in which the scattering length ranges from extremely large and positive to extremely large and negative. At 530 G, the scattering length passes through zero, producing a sample of noninteracting atoms.

# Cooling Fermi Gases in Optical Traps

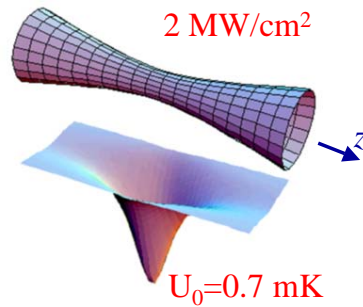


Our approach to producing a degenerate, strongly interacting gas differs from that of most other groups, in that we employ all-optical trapping and cooling methods. The optical trap is loaded from a standard magneto-optical trap which is produced from a slowed atomic beam.

# Optical Trap

## Focused Gaussian Laser Beam

$$U = -\frac{1}{2} \alpha \overline{E_0^2} \frac{1}{1+(z/z_0)^2} e^{-2r^2/w_0^2}$$



The optical trapping potential is proportional to the product of the static polarizability and the laser intensity. Approximately 65 watts of CO<sub>2</sub> laser power is focused to a radius of 50 micrometers, producing an intensity of 2 megawatts per square centimeter, and trap depth of 0.7 mK. The length of the trap is approximately a millimeter.

# Ultrastable CO<sub>2</sub> Laser Trap

- Stable Commercial Laser



- Typical Trap Parameters

$$P = 65 \text{ W} \quad \omega_0 = 47 \text{ } \mu\text{m}$$
$$z_0 = 0.7 \text{ mm}$$

$$I_0 = 2.0 \text{ MW/cm}^2 \quad U_0 = 0.7 \text{ mK}$$

$$\nu_r \cong 6.6 \text{ kHz} \quad \nu_z \cong 340 \text{ Hz}$$

- Negligible Optical Heating
  - Scattering Time: 1/2 hour
  - Optical Heating: 18 pK/s

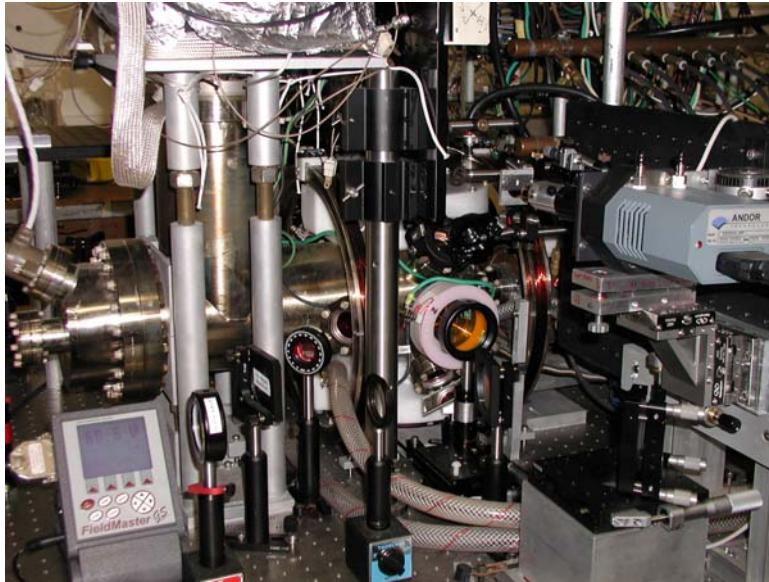
- Extremely Low Noise
  - Intensity Noise Heating

$$\Gamma^{-1} \geq 2.3 \times 10^4 \text{ sec}$$

- Ultra-High Vacuum
  - Pressure:  $< 10^{-11}$  Torr
  - Heating:  $< 5$  nK/sec
  - Lifetime: 400 sec

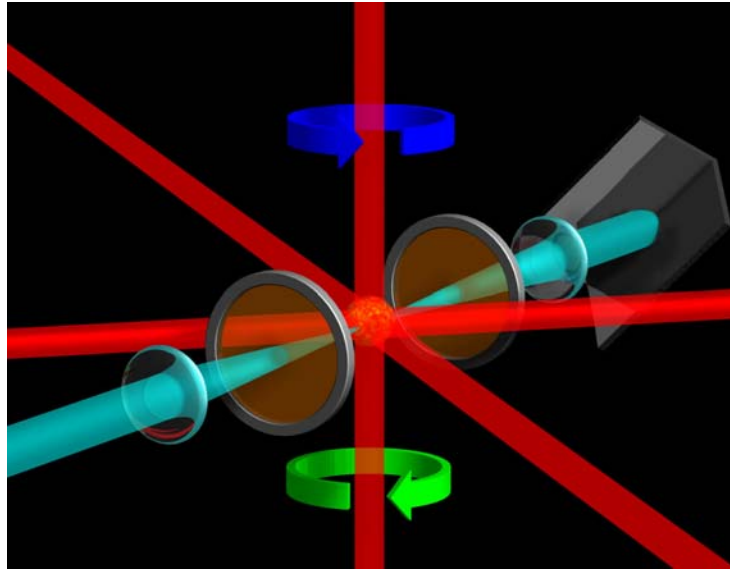
We use a 140 watt CO<sub>2</sub> laser from the lidar industry. The laser is exceptionally stable, with a noise-induced heating time of 23 thousand seconds. The long wavelength and large detuning from resonance yields a light scattering rate of only two photons per hour and negligible optical heating. The trap lifetime is 400 seconds.

# Experimental Apparatus



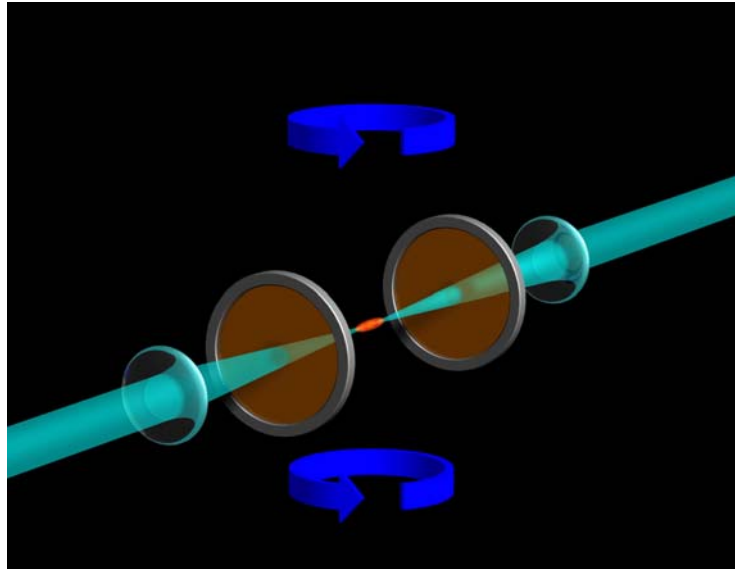
The lens in the foreground is used to focus the CO<sub>2</sub> laser beam into the vacuum system. A camera is used to record absorption images of the cloud.

# Optical Trap Loading



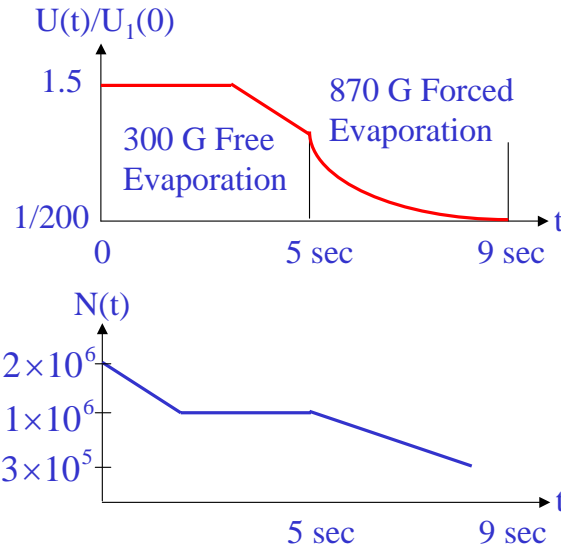
To reiterate the loading procedure, the CO<sub>2</sub> laser trap is first loaded from a magneto-optical trap. To increase the loaded number of atoms, the CO<sub>2</sub> laser beam is retroreflected using a rooftop mirror.

# Forced Evaporation



Next, the optical beams are extinguished and a magnetic field is applied to tune the gas into the Feshbach resonance region. Forced evaporative cooling is accomplished by lowering the trap laser intensity.

# Timing Sequence for Evaporation



Scaling Laws:

$$\frac{\rho_f}{\rho_i} = \left( \frac{U_i}{U_f} \right)^{1.3} = 10^3$$

$$\frac{N_f}{N_i} = \left( \frac{U_f}{U_i} \right)^{\frac{3}{16}} = \frac{1}{2.7}$$

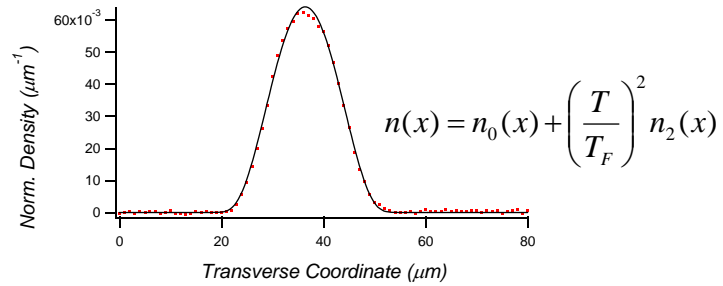
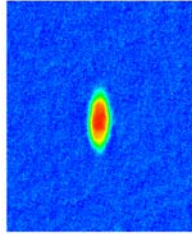
First, a 300 G magnetic field is applied at fixed trap depth. Then the trap is lowered at a field of 870 G, near the Feshbach resonance to produce a degenerate sample in a few seconds. Typically 2 million atoms are loaded. After free evaporation, 1 million atoms remain. Finally, after forced evaporation the number of atoms is reduced by a factor of 3, to 300 thousand, consistent with a scaling law model we have developed.



# Cooling a Strongly-Interacting Fermi Gas

Evaporate for 3.5 s at 910 G:

$t = 0.2$  ms after release

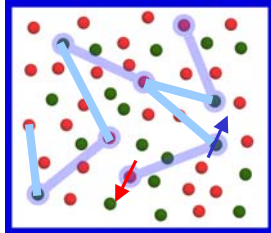


$T/T_F = 0.09$   
 $T = 0.7 \mu\text{K}$  at full trap depth  $U_0$   
 $T = 50 \text{ nK}$  at  $U_0/200$

Temperature is determined by fitting the transverse distribution of the expanded cloud to a Thomas-Fermi distribution for a noninteracting gas. Temperatures less than 0.1 of the Fermi temperatures are obtained.

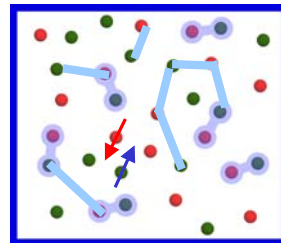
# Superfluidity in Atomic Fermi Gases

- Magnetically tunable interactions via Feshbach Resonance
- Theory BCS Pairing  $^6\text{Li}$ : Houbiers, *et al.*, PRA **56**, 4864 (1997).



$$\eta_c \approx \exp\left(\frac{-L}{|a_s|}\right) \ll 1$$

$$T_C = \eta_c T_F$$



$$\eta_c \approx 0.2-0.5$$

- On Resonance: **Super-High  $T_C$  Superconductivity!**

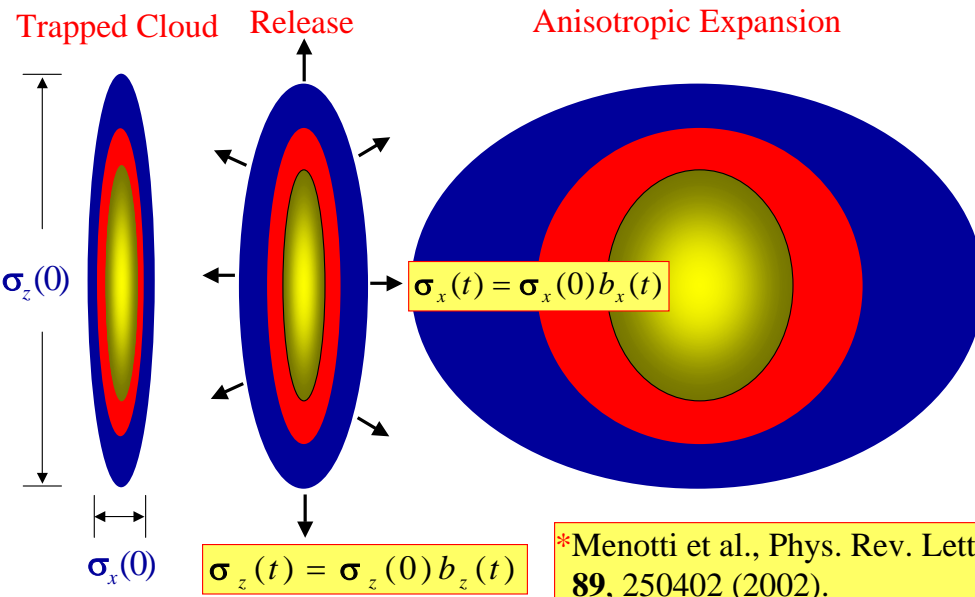
M. Holland, *et al.* Phys. Rev. Lett. **87**, 120406 (2001)

E. Timmermans, *et al.* Phys. Lett. A **285**, 228 (2001)

Y. Ohashi *et al.* cond-mat/0201262 (2002)

Tunable interactions enable new studies of superfluidity in the strongly interacting gas. The first theory of superfluidity in an atomic Fermi gas was done by a collaboration between the groups of R. Hulet and H. Stoof. They applied BCS theory to lithium-6. Recent theories of superconductivity in strongly interacting atomic Fermi gases suggest very high transition temperatures, a large fraction of the Fermi temperature. Such a transition, scaled to a condensed matter system would correspond to a superconductor which could operate at thousands of degrees, far above room temperature.

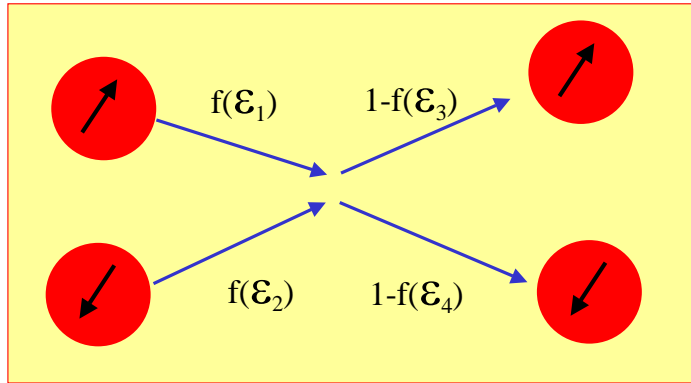
# Prediction of Anisotropic Expansion\*




One possible signature of superfluidity was predicted to be anisotropic expansion after release from the optical trap. The gas is expected to expand strongly in the transverse direction, while remaining nearly stationary in the axial direction.

## Can Pauli Blocking Suppress Collisions?

Collision **cannot** occur if the final state is occupied:



$$\Gamma_{\text{coll}} = \gamma \left( \frac{T}{T_F} \right)^2$$

||  0  
as  $T \rightarrow 0$

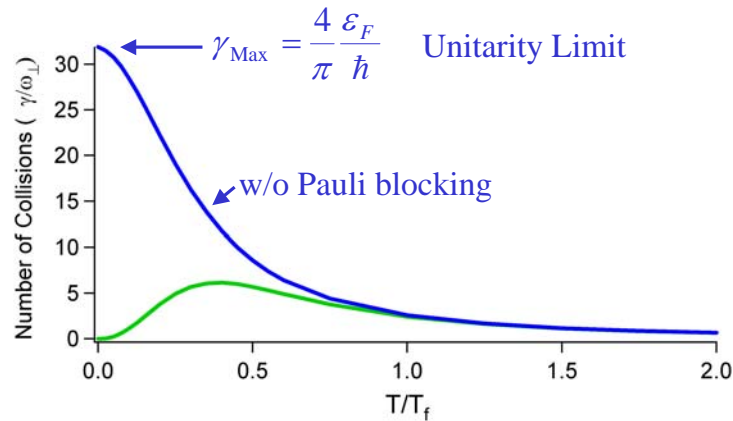
$f(\epsilon)$  is the occupation probability

The observation of anisotropic expansion is a signature of superfluidity if the gas is in the collisionless regime. Otherwise, the anisotropy can arise from collisional hydrodynamics. However, collisions are suppressed at low temperatures by Pauli blocking. In this case, colliding atoms cannot enter occupied energy levels, and the collision rate declines as the square of the temperature.

# Pauli Blocking in a Harmonic Trap

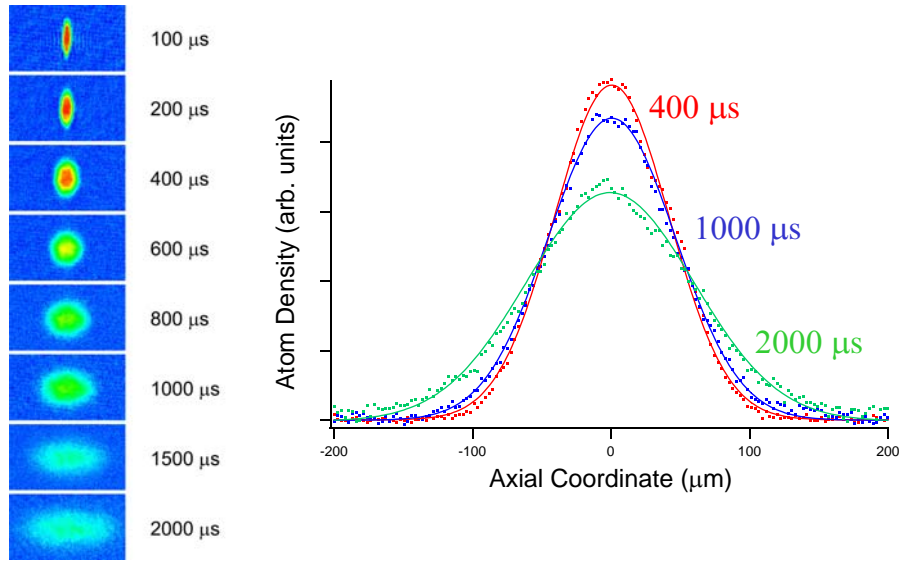


Depletion rate **with** and **without** Pauli Blocking:



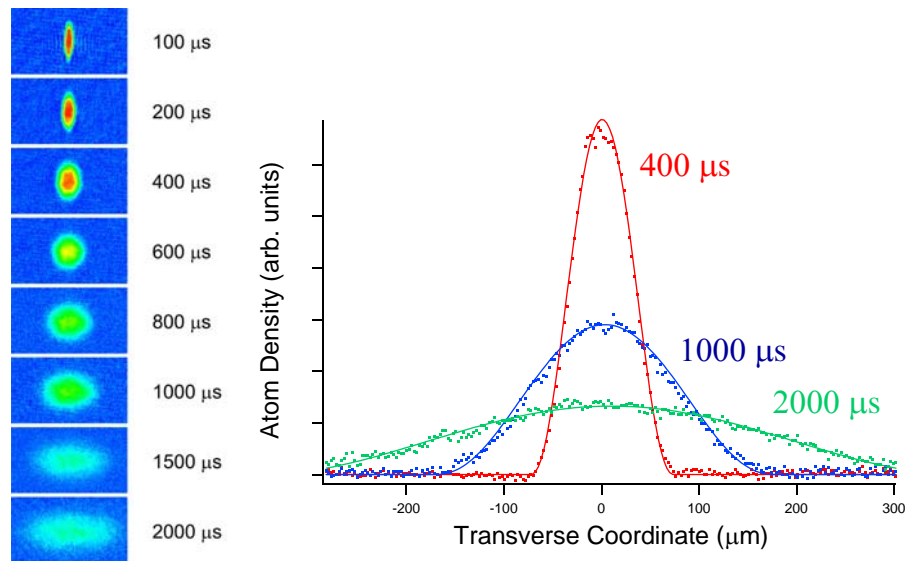
The blue curve shows how the collision rate of a unitarity-limited gas varies with temperature in the absence of Pauli blocking. With Pauli blocking, the collision rate is suppressed as shown by the green curve. Hence, by operating at temperatures of 0.15 TF or less, the collision rate of the trapped gas is suppressed. Nevertheless, an expanding gas may become collisional as the Fermi surface is deformed. Recent modeling suggests however, that this mechanism is not sufficient to produce strongly hydrodynamic expansion.

## Axial Expansion at 910 G



After release from the trap, the gas exhibits strongly anisotropic expansion, characteristic of nearly perfect hydrodynamics. The axial distributions remain nearly stationary.

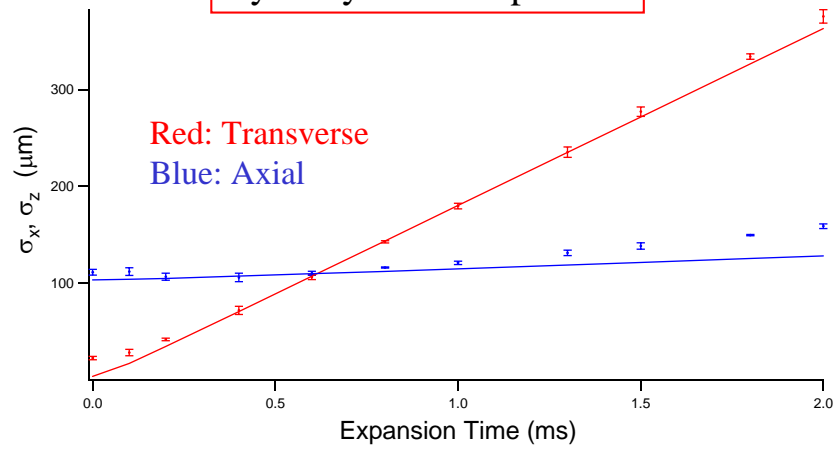
# Transverse Expansion at 910 G



By contrast, the transverse distributions expand rapidly.

## Transverse and Axial Widths vs Time

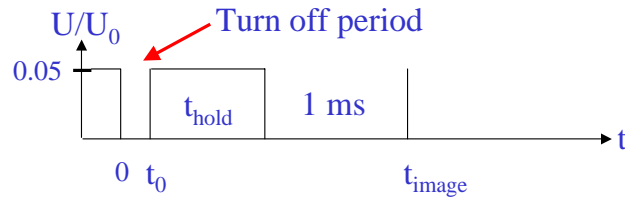
### Hydrodynamic Expansion



The fit of the observed expansion data is in very good agreement with hydrodynamic theory.



## Breathing Mode in a Trapped Fermi Gas



$$t_0 = \frac{1}{16} \frac{2\pi}{\omega}$$

$$\frac{T_i}{T_F} \cong 0.1 - 0.15$$



$$\frac{\Delta T}{T_F} \cong 0.05$$

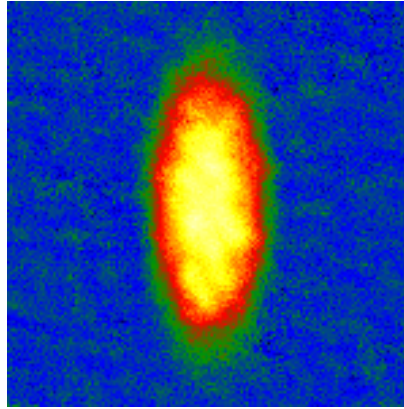
Measure the Breathing Mode Oscillation Frequency and Damping Time versus Temperature

To avoid issues of deforming the Fermi surface in observing hydrodynamic expansion, we have instead measured the radial breathing mode frequencies and damping times. The breathing mode of the trapped gas is excited by briefly turning off the trap. The corresponding energy input corresponds to 0.05  $T_F$  when the trap is extinguished for 1/16 of a radial oscillation period, and is reduced to 0.01  $T_F$  when the trap is off for only 1/32 of a period.

## Collective Modes in a Trapped Fermi Gas

$$B = 870 \text{ G}$$

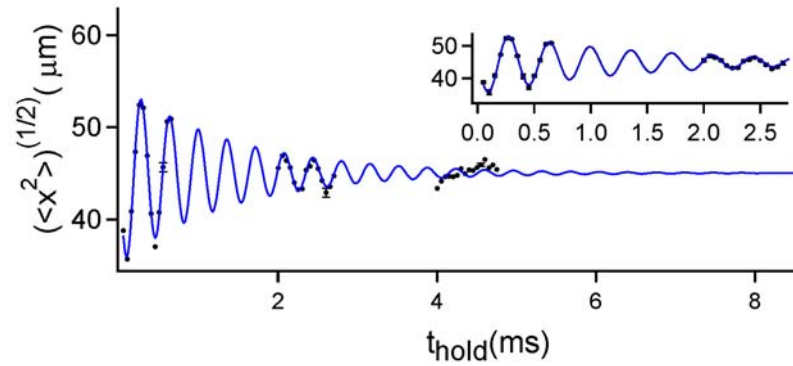
$$\frac{T_i}{T_F} = 0.1 - 0.15$$



After the breathing mode is excited, the gas is held for a variable time, and then allowed to expand for 1 ms, after which it is imaged to show the oscillation.

## Breathing Mode in a Trapped Fermi Gas

$$B = 870 \text{ G} \quad \frac{T_i}{T_F} = 0.50$$

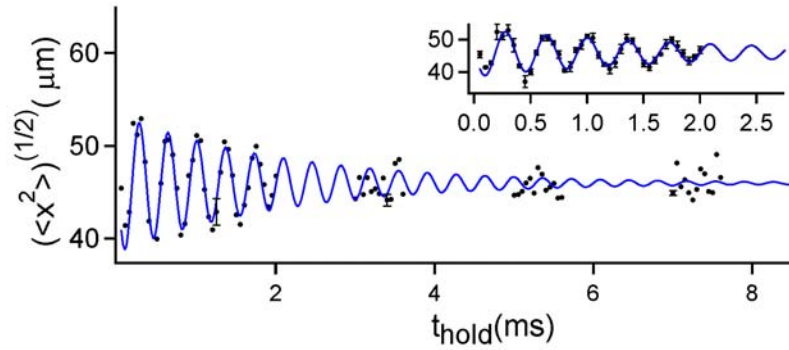


At a temperature of 0.5  $T_F$ , the oscillation decays in 1.4 ms.

## Breathing Mode in a Trapped Fermi Gas



$$B = 870 \text{ G} \quad \frac{T_i}{T_F} = 0.33$$

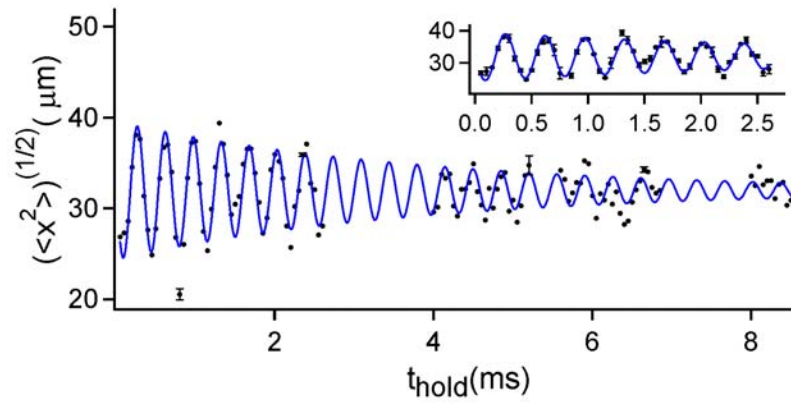


At 0.33  $T_F$ , the decay time increases to 2 ms.

## Breathing Mode in a Trapped Fermi Gas



$$B = 870 \text{ G} \quad \frac{T_i}{T_F} = 0.17$$



Finally, at a temperature of 0.17, the gas decays in 4 ms.

## Breathing Mode Frequency



Measured Oscillation Frequencies of Noninteracting Atoms:

$$\omega_x = 2\pi \times 1600 \text{ Hz}$$

$$\omega_y = 2\pi \times 1500 \text{ Hz}$$

Predicted Frequency for Hydrodynamic Fermi Gas:

$$\omega_{\text{Hydro}} = \sqrt{\frac{10}{3}} \omega_x \omega_y = 2\pi \times 2830 \text{ Hz}$$

Measured Oscillation Frequency for Sinusoidal Fit:

$$\omega_{\text{Meas}} = 2\pi \times 2840 \text{ Hz}$$

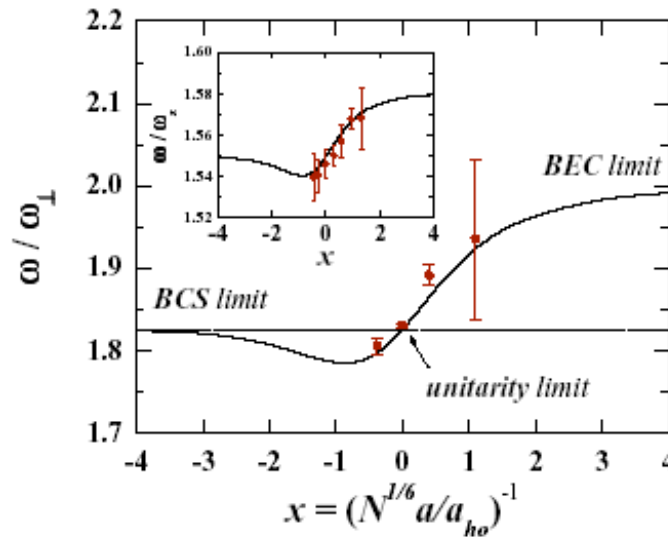
At 870 G, the measured frequency of the breathing mode is in very good agreement with that expected for a hydrodynamic gas in the unitarity limit.

The predictions are based on the oscillation frequencies measured for atoms in the noninteracting gas.

# Breathing Mode Frequency vs B-Field



Hui Hu, A. Minguzzi, Xia-Ji Liu, and M. P. Tosi



Feshbach at 850 G

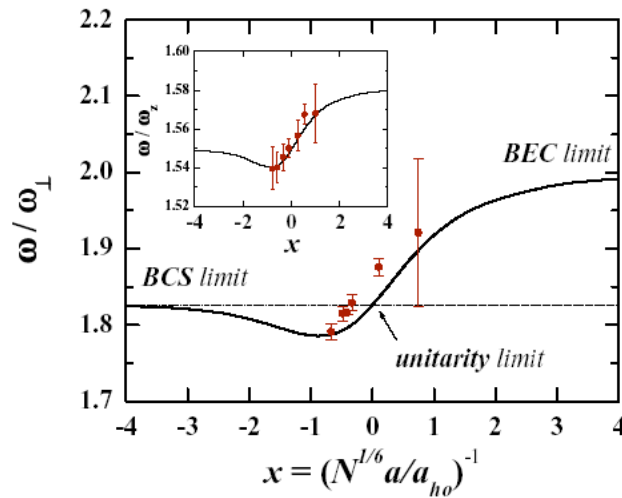
cond-mat/0404012  
(Apr 2004)

The magnetic field dependence of the breathing mode frequencies is shown for the radial direction (lower) measured by our group and for the axial direction (measured by the Innsbruck group). If the Feshbach resonance is located at 850 G, the agreement is reasonably good.

# Breathing Mode Frequency vs B-Field



Hui Hu, A. Minguzzi, Xia-Ji Liu, and M. P. Tosi



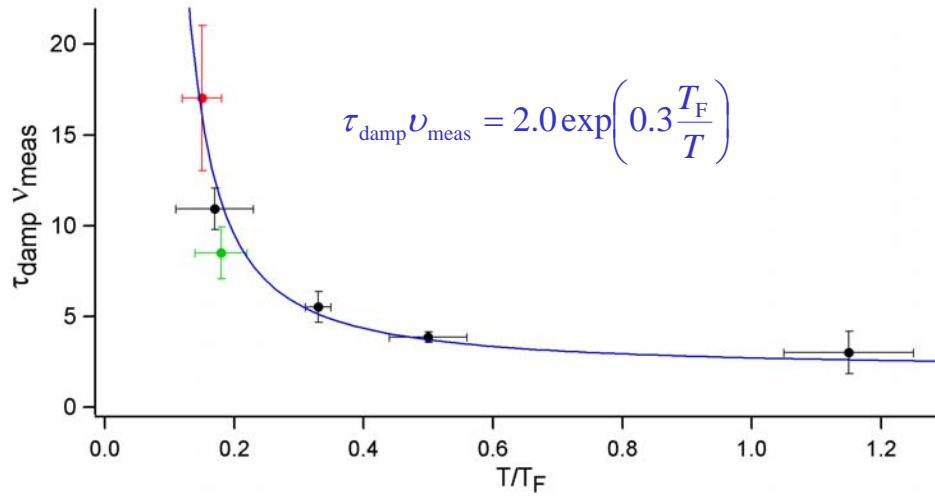
Feshbach at 822 G

cond-mat/0404012  
(Apr 2004)

Moving the Feshbach resonance to 822 G produced worse agreement with the radial measurement. However, the measured frequencies display the predicted trend and are still hydrodynamic.



## Damping Time of the Breathing Mode



The damping time shows a rapid increase with decreasing temperature.

The red and green data points are taken with the duration of the trap turn off set to 25 microseconds, while all other data is taken at 50 microseconds. The green point is taken at approximately four times the trap depth, and it is at approximately twice the frequency.

# Summary



- All-Optical Production of Degenerate Fermi Gas
  - Efficient evaporation near Feshbach resonance
  - Very low  $T/T_F$

## Hydrodynamics of a Strongly-Interacting Fermi Gas

- Observation of Anisotropic Expansion
  - For low  $T$ , collisions may not explain hydrodynamics
- Trapped Atom Hydrodynamics
  - Collisionally-damped hydrodynamic spectra at high  $T$
  - Hydrodynamic breathing modes weakly-damped as  $T$  is reduced
  - First evidence for superfluid hydrodynamics in a Fermi gas

In summary, we use all-optical methods with evaporative cooling near a Feshbach resonance to produce a strongly interacting degenerate Fermi gas.

We observe hydrodynamic behavior in the expansion dynamics. At low temperatures, collisions may not explain the expansion dynamics.

We observe hydrodynamics in the trapped gas. Our observations include collisionally-damped excitation spectra at high temperature which were not discussed above. In addition, we observe weakly damped breathing modes at low temperature. The observed temperature dependence of the damping time and hydrodynamic frequency are not consistent with collisional dynamics nor with collisionless mean field interactions. These observations constitute the first evidence for superfluid hydrodynamics in a Fermi gas.

# Numerical simulation studies of the convective instability onset in a supercritical fluid

A. Furukawa<sup>1</sup>, H. Meyer<sup>2</sup> and A. Onuki<sup>1</sup>

1. *Department of Physics, Kyoto University, Kyoto 606-8502, Japan*

2. *Department of Physics, Duke University, Durham, NC 27708-0305, USA.*

(Dated: 8/22/04)

Numerical simulation studies are reported for the convection of a supercritical fluid,  $^3\text{He}$ , in a Rayleigh-Bénard cell. The calculations provide the temporal profile  $\Delta T(t)$  of the temperature drop across the fluid layer. In a previous article, systematic delays in the onset of the convective instability in simulations relative to experiments were reported, as seen from the  $\Delta T(t)$  profiles. They were attributed to the smallness of the noise which is needed to start the instability. Therefore i) homogeneous temperature noise and ii) spatial lateral periodic temperature variations in the top plate were programmed into the simulations, and  $\Delta T(t)$  compared with that of an experiment with the same fluid parameters. An effective speed-up in the instability onset was obtained, with the best results obtained through the spatial temperature variations with a period of  $2L$ , close to the wavelength of a pair of convection rolls. For a small amplitude of  $0.5 \mu\text{K}$ , this perturbation gave a semiquantitative agreement with experimental observations. Results for various noise amplitudes are presented and discussed in relation to predictions by El Khouri and Carlès.

PACS numbers: 44.25+f, 47.27.Te, 64.70.Fx

## I. INTRODUCTION

In recent papers, convection experiments of supercritical  $^3\text{He}$  at the critical density in a Rayleigh-Bénard cell with a constant heat current  $q$  were reported[1, 2]. After  $q$  is started, the temperature drop  $\Delta T(t)$  across this highly compressible fluid layer increases from zero, an evolution accelerated by the “Piston Effect” [3–5]. Assuming that  $q$  is larger than a critical heat flux necessary to produce fluid instability,  $\Delta T(t)$  passes over a maximum at the time  $t = t_p$ , which indicates that the fluid is convecting and that plumes have reached the top plate. Then truncated or damped oscillations, the latter with a period  $t_{\text{osc}}$ , are observed under certain conditions before steady-state conditions for convection are reached, as described in refs.[1, 2]. The scenario of the damped oscillations, and the role of the “piston effect” has been described in detail in refs.[6] and [7] and will not be repeated here. The height of the layer in the RB cell was  $L = 0.106 \text{ cm}$  and the aspect ratio  $\Gamma=57$ . The  $^3\text{He}$  convection experiments extended over a range of reduced temperatures be-

tween  $5 \times 10^{-4} \leq \epsilon \leq 0.2$ , where  $\epsilon = (T - T_c)/T_c$  with  $T_c = 3.318 \text{ K}$ , the critical temperature. The truncated - or damped oscillations were observed for  $\epsilon \geq 0.009$  and over this range the fluid compressibility varies by a factor of about 30.

The scaled representation of the characteristic times  $t_{\text{osc}}$  and  $t_p$  versus the Rayleigh number, and the comparison with the results from simulations has been described in ref.[8]. Good agreement for the period  $t_{\text{osc}}$  was reported. However a systematic discrepancy for the times  $t_p$  shows that in the simulations the development of convection is retarded compared to the experiments. This effect increases with decreasing values of  $[Ra^{\text{corr}} - Ra_c]$ , where  $Ra^{\text{corr}}$  is the Rayleigh number corrected for the adiabatic temperature gradient as defined in refs.[1, 2] and  $Ra_c$  is the critical Rayleigh number, 1708. This is shown in Fig.1 of ref.[8], in particular in Fig.1b) for  $\epsilon = 0.2$  and  $q = 2.16 \times 10^{-7} \text{ W/cm}^2$  ( $[Ra^{\text{corr}} - Ra_c] = 635$ ), where an experimental run is compared with simulations for the same parameters. Here clearly the profile  $\Delta T(t)$  from the simulations shows the smooth rise until the steady-state value,  $\Delta T = qL/\lambda$

$= 95 \mu\text{K}$  has been reached, where  $\lambda$  is the thermal conductivity. Only at  $t \approx 90 \text{ s.}$  does convection develop, as shown by a sudden decrease of  $\Delta T(t)$ . By contrast, the experimental profile shows a much earlier development of convection. Fig.1 of ref.[8] is representative for the observations at low values of  $[Ra^{\text{corr}} - Ra_c]$ . At high values, both experiment and simulations show the convection development to take place at comparable times, as indicated in Fig.5b) of ref.[8], and specifically in Fig.2 a) of ref.[7], where  $[Ra^{\text{corr}} - Ra_c] = 4.1 \times 10^5$ . It is the purpose of this report to investigate the origin of this discrepancy by further simulation studies.

## II. CONVECTION ONSET CALCULATIONS, SIMULATIONS AND COMPARISON WITH EXPERIMENTS

El Khouri and Carlès[9] studied theoretically the stability limit of a supercritical fluid in a RB cell, when subjected to a heat current  $q$  started at the time  $t = 0$ . Their fluid was also  $^3\text{He}$  at the critical density, and the same parameters as in ref.[1] were used. They calculated the time  $t_{\text{instab}}$  and also the corresponding  $\Delta T(t_{\text{instab}})$  for the onset of fluid instability and they determined the modes and the wave vectors of the perturbations for different scenarios of  $q$  and  $\epsilon$ . For  $t > t_{\text{instab}}$  inhomogeneities in the RB cell and noise within the fluid will produce perturbations which will grow, from which the convection will develop. An indication of the growth of convection is a deviation of the  $\Delta T(t)$  profile in the experiments or in the simulations from the calculated curve for the stable fluid (see for instance Eq.3.3 of ref[6]). It is readily seen from simulation profiles such as Fig.1a) and b) in ref.[6] that the deviation becomes significant for  $t$  only slightly below  $t_p$  - the maximum of  $\Delta T(t)$ . In simulations, the effective start of convection can also be seen from snapshots in 2D of the fluid temperature contour lines at various times, as shown in Fig. 5 of ref.[10].

P.Carlès [11] has argued that the reason for the discrepancy for the time  $t_p$  between experiment and

simulation is that in the former, the physical system has noise and inhomogeneities which cause the perturbations beyond  $t_{\text{instab}}$  to grow into the developed convection. By contrast simulations have a much smaller noise. Therefore in the simulations the perturbations take a longer time to grow than in the physical system, leading to a larger  $t_p$  than observed. Carlès' comment led us to try as a first step imposing a thermal random noise on the top plate of the RB cell, which was to simulate fluctuations in the upper plate temperature control of the laboratory experiment. The temperature of the plate was assumed to be uniform, because of the large thermal diffusivity  $D_T \approx 2 \times 10^4 \text{ cm}^2/\text{s.}$  of the copper plate in the experiments. Accordingly simulations were carried out with a homogeneous time-dependent temperature random fluctuation of given rms amplitude imposed on the upper plate. This implementation consisted in adding or subtracting randomly temperature spikes  $T_t$  at the time  $t$  with a programmed rms amplitude at steps separated by 0.02 s. This interval is much larger than the estimated relaxation time of the top plate over a distance  $2L$ , approximately the wavelength of convection roll pair. Values of the variance  $A = \sqrt{\langle (T_t - \langle T_t \rangle)^2 \rangle}$  were chosen between 0 and 40  $\mu\text{K}$ . The range of the  $A$  values was taken well beyond the estimated fluctuation rms amplitude during the experiments[1] of  $\approx 1 \mu\text{K}/\sqrt{Hz}$ . Three representative curves with 0, 3 and 40  $\mu\text{K}$  are shown in Fig.1a) by dashed lines for  $\epsilon = 0.2$  for  $q = 2.16 \times 10^{-7} \text{ W/cm}^2$ ,  $L = 0.106 \text{ cm}$  and  $\Gamma = 5.1$ . For this value of  $q$ , the calculation by El Khouri and Carlès [12] give  $t_{\text{instab}} = 6.3 \text{ s}$  and  $\Delta T(t_{\text{instab}}) = 75 \mu\text{K}$ . In the simulation without imposed noise, the start of convection has therefore been considerably delayed relative to  $t_{\text{instab}}$ . The injection of random noise has a significant effect in developing convection at an earlier time. In Fig.1a) the three curves are also compared with the experimental one, shown by a solid line. Here we have not incorporated into the simulations the delay affecting the experimental temperature recording, so that they could be inter-compared more readily, and also with predictions[12]

However this operation will be presented in Fig.4. Further simulations with added random noise were carried out for  $\epsilon = 0.2$  and  $0.05$  where the  $\Delta T(t)$  time profiles are not shown here.

Fig.2a) shows a plot of the time of the developed convection, represented by  $t_p$ , versus the random rms amplitude  $A$  for three series of simulations, all taken for a cell with  $\Gamma = 5.1$ . They are a) and b)  $\epsilon = 0.2$ ,  $q = 2.16$  and  $3.89 \times 10^{-7} \text{ W/cm}^2$ , and c)  $\epsilon = 0.05$ ,  $q = 60 \text{ nW/cm}^2$ ,  $([Ra^{\text{corr}} - Ra_c] = 635, 1740 \text{ and } 4200)$ . The simulation results, shown by solid circles, are compared with the experimentally observed  $t_p$  shown by horizontally dot-dashed lines. It can be clearly seen that noise imposition, which creates a vertical disturbance across the fluid layer, reduces the time of convection development. While the decrease of  $t_p$  is strong for small values of  $A$ , it saturates at a certain level of noise amplitude. The gap between simulations and experiment increases with a decrease of  $[Ra^{\text{corr}} - Ra_c]$ , namely as the fluid stability point is approached. A “critical slowing down” is seen in the effectiveness of the perturbations in triggering the instability. Hence this mode of noise introduction fails, because its amplitude is limited to the vertical  $z$  direction and it evidently couples only weakly into the convective motion.

In parallel with the present experiments, S. Amiroudine[13] also carried out a systematic study of simulations on supercritical  $^3\text{He}$  in a RB cell for several values of  $\epsilon$  and  $q$ . The resulting profiles  $\Delta T(t)$  could be compared with those from experiments done under nearly the same conditions. In his simulations, homogeneous temperature random noise was again imposed on the top plate. The shift in  $t_p$  showed less systematic trends than in the results described in this report. However for the same values of  $\epsilon$  and  $q$  as those reported above, and at zero noise, the  $t_p$  values tended to be somewhat smaller than in the results of Fig 2a).

Here we mention that the onset of convection in the simulations is further influenced by the aspect ratio  $\Gamma$ . The simulations described above, but without noise, were carried out in a cell  $\Gamma = 5.1$  hav-

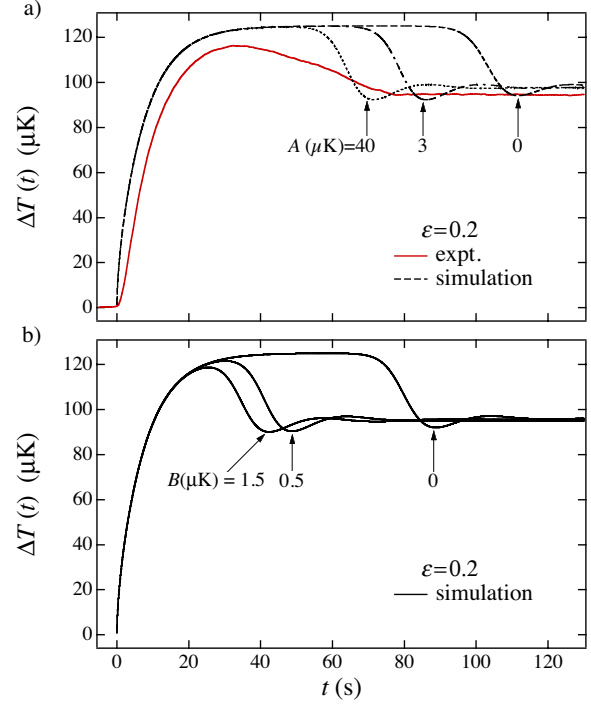


FIG. 1: a) the temperature profile  $\Delta T(t)$  from experiments (solid line with noise) and from several simulations (dashed lines) at  $\epsilon = 0.2$ ,  $q = 2.16 \times 10^{-7} \text{ W/cm}^2$ . In the simulations,  $\Gamma = 5$  and uniform temperature noise has been imposed on the top plate with variance  $A(\mu K) = 0, 3$  and  $40$ , as described in the text. b) Temperature profile  $\Delta T(t)$  from several simulations at  $\epsilon = 0.2$ ,  $q = 2.16 \times 10^{-7} \text{ W/cm}^2$ ,  $\Gamma = 8$  and imposed lateral periodic, time independent temperature variations on the top plate with period  $2L$  and amplitude  $B(\mu K) = 0, 0.5$  and  $1.5$ .

ing periodic lateral boundaries. Further simulations with zero noise for  $\epsilon = 0.2$  with  $\Gamma = 8.0, 10.2, 20.5$  and  $41.0$  were carried out, and showed a decrease of the convection development time from  $\approx 90 \text{ s}$ , tending to a constant value of  $\approx 60 \text{ s}$ . above  $\Gamma = 20$ . This shift in the onset of instability is probably due to the decreased finite size effect which the rising plumes experience with increasing  $\Gamma$ , in spite of the periodic boundary conditions.

The next step in our attempts, stimulated by communications with P. Carlès, was introducing perturbations into the simulations via some time-independent lateral variation proportional to  $\sin$

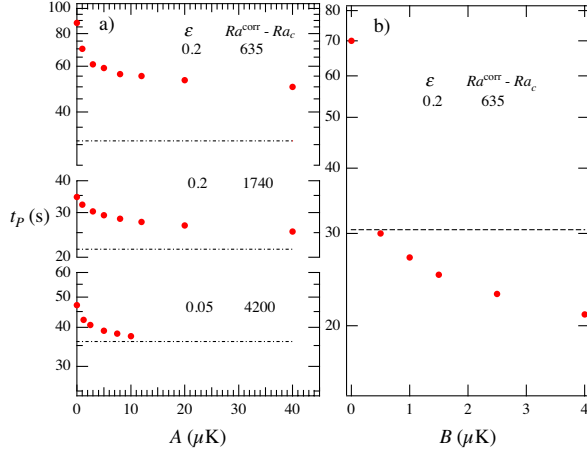


FIG. 2: a) The time for effective development of convection, characterized by  $t_p$ , versus  $A$  (homogeneous temperature noise imposed on the top plate). The horizontal dot-dashed lines indicate the observed  $t_p$ , corrected for instrumental recording delay. b) The time for effective development of the convection, labeled by  $t_p$  versus  $B$  (lateral time-independent periodic temperature variations). The horizontal dashed line indicates  $t_p$  as obtained by experiment, corrected as before.

( $2\pi x/P$ ) where  $P$  is the period. A periodic variation in the spacing of the plates proved not to be feasible for our simulation code, and instead we opted to introduce again a temperature variation in the top plate with an amplitude  $B$  (in  $\mu\text{K}$ ) and period  $P=2L$ , nearly the same as the wavelength of a pair of convection rolls. The temperature of the bottom plate was kept homogeneous. This “Gedanken Experiment” implies that the material of the top plate permitted a temperature inhomogeneity, which of course is not realized in the experiment. As a control experiment, we also made a simulation with  $P = L$ .

Fig 1b) shows representative profiles  $\Delta T(t)$  for the parameters  $\epsilon = 0.2$  and  $q = 2.16 \times 10^{-7} \text{ W/cm}^2$  and with  $B = 0, 0.5$  and  $1.5 \mu\text{K}$ , and for  $\Gamma=8$ . For  $B = 0$ , the effect of having a larger  $\Gamma$ , namely 8 instead of 5.1, can be seen by comparing with the curve  $A=0$  in Fig.1a). As  $B$  is increased from zero, there is a large decrease in the time for convection development, represented by  $t_p$ , which is plotted versus  $B$  in Fig 2b). The horizontal dashed line shows the  $t_p$

from the experiment, and this plot is to be compared with Fig. 2a). For an inhomogeneity amplitude of only  $B = 0.5 \mu\text{K}$ ,  $t_p$  is nearly the same for simulations and experiment. By contrast, simulations with  $B=2 \mu\text{K}$  and  $P=L$  (not presented here) show no difference from those with  $B=0$ . Hence the nucleation of the convection is accelerated if the period is in approximate resonance with the wavelength of a convection roll pair. The values of steady-state  $\Delta T$  and  $t_{\text{osc}}$  are only marginally affected by the noise.

We note from Fig.1b) that the simulation curve calculated for  $B = 0$  shows the fluid not convecting until  $\approx 70$  s. For the curves with  $B = 0.5 \mu\text{K}$ , the start of deviations from the stable fluid curve cannot be estimated well from Fig.1b) but is readily obtained from the data files, which tabulate  $\Delta T(t)$  to within 1 nK. For  $B = 0.5 \mu\text{K}$ , systematic deviations  $\delta \Delta T(t, B) \equiv [\Delta T(t, B=0) - \Delta T(t, B)]$  increase rapidly from 1 nK for  $t > 8$  s (where  $\Delta T \approx 85 \mu\text{K}$ ), a value comparable with the predicted  $t_{\text{instab}} = 6.3$  s.,  $\Delta T(t_{\text{instab}}) = 75 \mu\text{K}$ [12]. However a comparison with predictions becomes more uncertain as  $B$  is increased. This is because the changes in the base heat flow by the periodic perturbations are not considered in the theory[12]. We also note that the time interval  $\delta t \equiv [t_p - t_{\text{instab}}]$  between the first sign of instability ( $\delta \Delta T > 0$ ) and  $t_p$  is  $\approx 20$  s, and roughly independent of  $B$ . This represents approximately the period taken by the convection to develop and for the plumes to reach the top plate boundary.

In Fig.3, we present a series of 2D “snapshots” at various times for the simulation with  $B = 0.5 \mu\text{K}$ , showing the temperature contour lines (in color) for the RB cell. The “warm” side is shown by red,  $T(t, z = 0)$  and the “cold” side by mauve,  $T(z = L) = \text{const}$ . At  $t = 8$  s. the fluid instability has just started near the top of the layer, while near the bottom the temperature contour lines are still horizontal. At  $t = 27$  s., where the peak of  $\Delta T(t)$  at  $z = L$  has been reached, the warm plumes have reached the top plate, and the “cold” piston effect is about to start, causing the bulk fluid temperature to drop and  $\Delta T(t)$  to decrease. The transient process con-

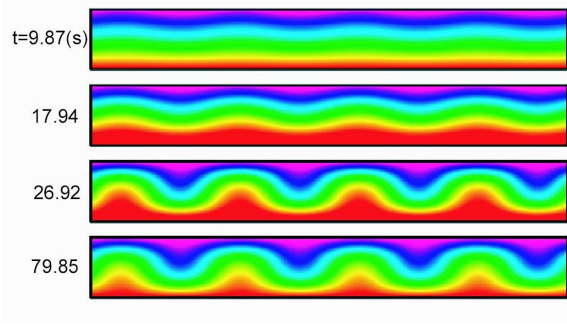


FIG. 3: Snapshots in 2D for the RB cell with an aspect ratio of 8, of simulations with  $B = 0.5 \mu K$  at various times  $t$  after starting the heat current  $q$ . The temperature contour lines and their evolution are described in the text. At the time  $t = 9.9$ s, the fluid instability has just started near the top.

tinues with damped oscillations of  $\Delta T(t)$ . Steady state convection is reached at  $t = 80$ s, with a pair of convection rolls having a wavelength of  $\approx 2L$ , as expected.

In Fig.4 we show the profiles  $\Delta T(t)$  from the experiment and from the simulations with a periodic perturbation amplitude  $B = 0.5 \mu K$ . For an optimal comparison, the delay affecting the experimental temperature recording was incorporated into the simulation curve. For this, the delay function with the instrumental time constant  $\tau = 1.3$  s. [1] was folded into the simulation curve by a convolution method. This operation retards the initial rise of the temperature drop by the order of 2-3 seconds, and brings both experiment and simulations into fair agreement in the regime where the fluid is stable. The time  $t_p$  for the maximum is now closely the same for both experiments and simulations. However beyond the predicted instability time  $t_{\text{instab}} = 6.3$  s., the experimental curve starts to deviate more rapidly with time than do the numerical simulations from the calculated curve for the fluid in the stable regime. As discussed previously[2], for these parameters of  $\epsilon$  and  $q$  the experiment does not show damped oscillations, which are observed for higher values of  $q$ . In the steady-state, the agreement is very good.

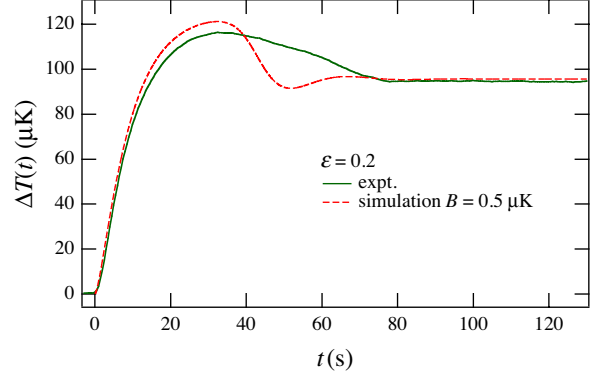


FIG. 4: Comparison of the profile  $\Delta T(t)$  from experiment and from simulations with  $B = 0.5 \mu K$ . To make the comparison realistic, the simulations have been convoluted with the same “instrumental” delay time  $\tau = 1.3$  s. which has influenced the shape of the experimental curve.

Our goal has been to show that injecting a small temperature perturbation into the top plate, produces for the simulations an earlier start in the convective instability, which becomes consistent with experimental observations. For this, we have limited ourselves to an example at a low value of  $[Ra^{\text{corr}} - Ra_c]$ , where the delay has been particularly large with respect to the experiment.

### III. SUMMARY AND CONCLUSION

We have presented a comparison of numerical simulations with experimental data investigating the transient to steady convection after the start of a heat current through a supercritical  $^3\text{He}$  layer in a RB cell. Here the temperature drop  $\Delta T(t)$  across the fluid layer versus time  $t$  was studied. The aim was to understand and to reduce the discrepancy between experiment and simulations in the time of the convection development, as detected by  $\Delta T(t)$ . Simulations for one set of fluid parameters (where the largest discrepancy had been observed) are reported with imposed temperature variations on the top plate. Satisfactory results were obtained for spatial lateral temperature variations with an amplitude of  $0.5 \mu K$  and a period approximately equal to that

of the wavelength of a convection roll pair. As the perturbation amplitude is further increased, the development of convection occurs earlier than the observed one.

#### IV. ACKNOWLEDGMENT

The authors are greatly indebted to P. Carlès for stimulating correspondence and suggestions, to F.

Zhong for help with figures formatting and the convolution program in Fig.3 and to R.P. Behringer and P. Carles for useful comments on the manuscript. The interaction with S. Amiroudine, who conducted numerical simulation in parallel with present investigations is greatly appreciated. The work is supported by the NASA grant NAG3-1838 and by the Japan Space Forum H12-264.

- 
- [1] A.B. Kogan and H. Meyer, Phys. Rev. E **63**, 056310 (2001).
  - [2] H. Meyer and A.B. Kogan, Phys. Rev. E **66**, 056310 (2002).
  - [3] A. Onuki and R.A. Ferrell, Physica A **164**, 245 (1990).
  - [4] B. Zappoli, D. Bailly, Y. Garrabos, B. le Neindre, P. Guenoun and D. Beysens, Phys. Rev. A **41**, 2264 (1990).
  - [5] B. Zappoli, Phys. of Fluids **4**, 1040 (1992), B. Zappoli and P. Carles, Eur. J. Mech. B/Fluids **14**, 41, (1995)
  - [6] A. Furukawa and A. Onuki Phys. Rev. E **66**, 016302 (2002).
  - [7] S. Amiroudine and B. Zappoli, Phys. Rev. Lett. **90**, 105303 (2003).
  - [8] A. Furukawa, H. Meyer, A. Onuki and A.B. Kogan, Phys. Rev. E **68**, 0563XX (2003)]
  - [9] L. El Khouri and P. Carlès, Phys. Rev. E **66**, 066309 (2002).
  - [10] Y. Chiwata and A. Onuki, Phys. Rev. Lett. **87**, 144301 (2001).
  - [11] P. Carlès, private communication.
  - [12] L. El Khouri and P. Carlès, Private communication.
  - [13] S. Amiroudine, private communication.



# Shape of Strained Solid $^4\text{He}$ at Low Temperatures

Harry Kojima  
Rutgers University

JPL/NASA Workshop on Fundamental Physics in Microgravity

Solvang, CA 2004

# outline

1. introduction to stress-driven instability
2. motivation: related phenomena on geologic, kitchen and nano-scales
3. intuitive picture of stress-driven instability  
(without and with gravity, critical stress, why use helium?)
4. apparatus: interferometry set up
5. results
6. summary

# 1. Introduction to stress-driven instability

Start with a solid in equilibrium with its melt.  
Apply external stress.

**Q: what happens to its shape?**



**Theoretical study by:** Asaro-Tiller-Grinfeld\*

(Asaro-Tiller started their theory work on cracks and corruptions induced by stress. Grinfeld independently generalized the theory to apply to other situations.)

**A: beyond a threshold stress, the surface is predicted to become unstable and to develop corrugations.**

**Present research:** use solid  $^4\text{He}$  in contact with superfluid melt to experimentally study the predicted instability.

\*Asaro, R.J.Tiller, W.A, Metall. Trans. **3**, 1789(1972).  
Grinfeld, M., Soviet Phys. Dokl. **31**, 31 (1986).

# 2. Phenomena related to stress-driven instability

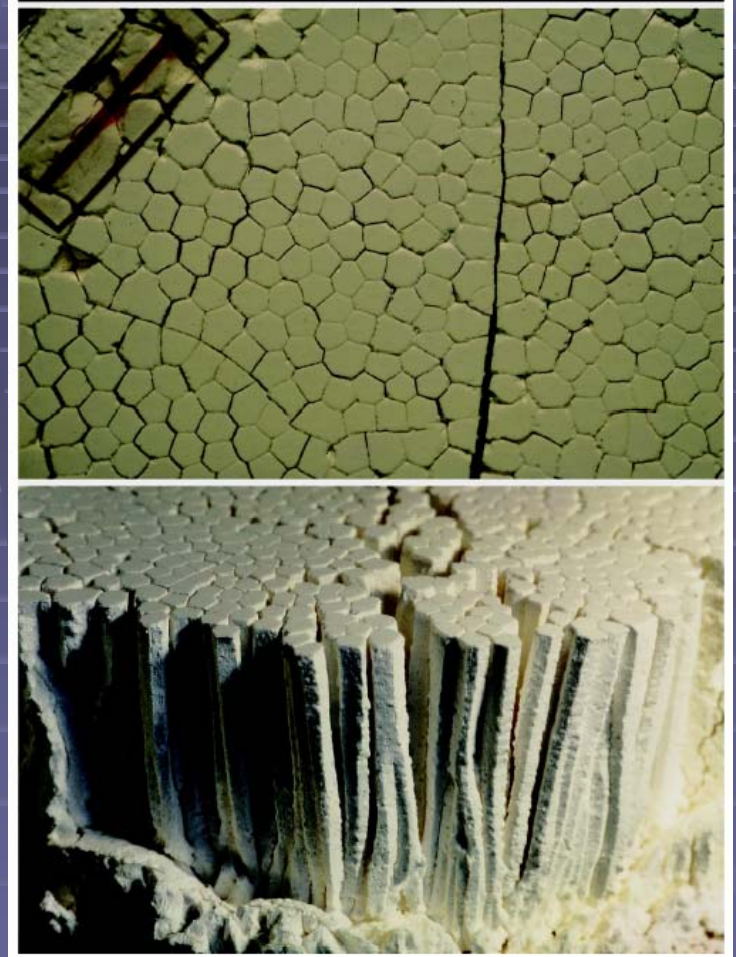
## (1) Giant's Causeway Northern Ireland



These are photographs for Giant's Causeway in Northern Ireland. These geologic formations are thought to be formed by the rapid cooling of molten lava. The rapid cooling can produce large stresses within the lava. These stresses are thought to have produced these patterned surface formations. So this is (possibly) an example of stress-driven instability on a grand geologic scale. Of course, the natives have another theory based on a fight between Giants. But, that's another story.



## (2)Drying starch



Structures somewhat similar to the Giant's causeway can be produced in a kitchen. Muller\* made the observation by drying a beaker of wet starch. The photos at right show the regular pattern seen after drying. This may be another example of stress-driven instability effect, now on the mm scale rather than meter scale.

\*G. Muller, J. Volcanology and Geothermal Research 86, 93(1998)

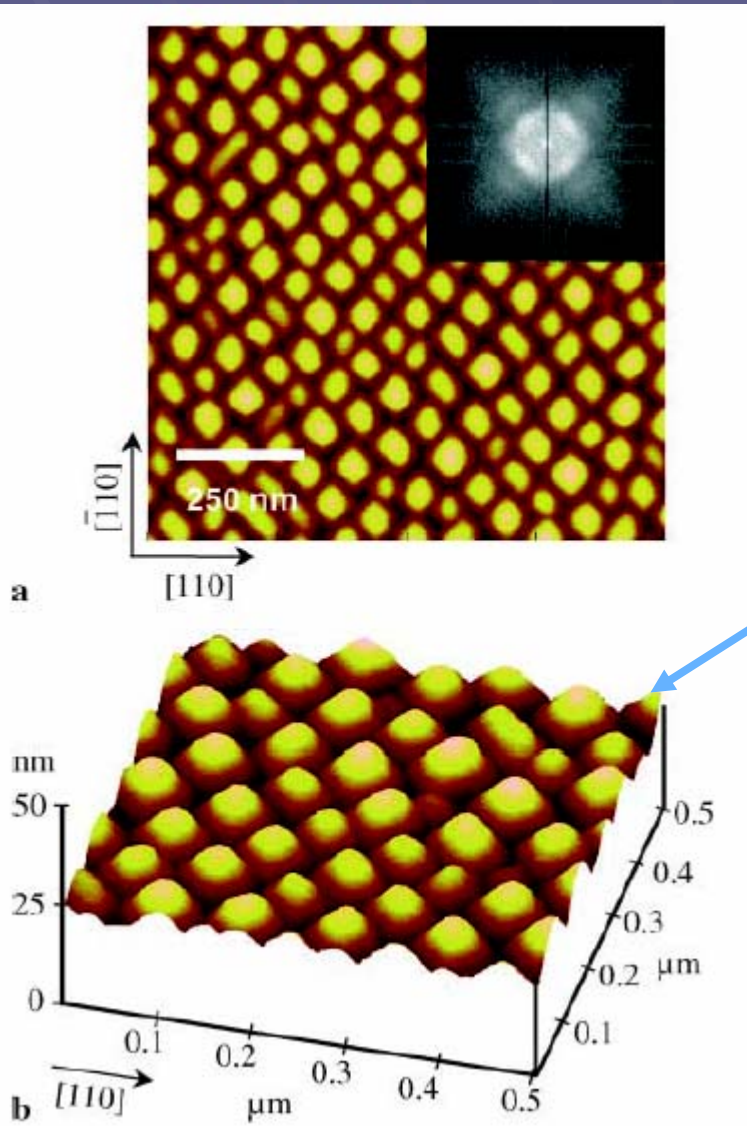
### (3) nano-structures by self-organization

Strain mediated self-organization of {105} faceted SiGe crystallites in a SiGe/Si superlattice grown on Si(001). a  $1\text{ }\mu\text{m}\times 1\text{ }\mu\text{m}$  AFM image of the 20th alloy layer of a  $20\times(2.5\text{ nmSi}_{0.25}\text{Ge}_{0.75}/10\text{ nm Si})$  multilayer film, color scale range: 20 nm. (The *inset*: the 2D power spectrum calculated from a  $5\text{ }\mu\text{m}\times 5\text{ }\mu\text{m}$  image).

3D AFM image of multiple adlayers of Si-Ge grown on Si substrate.

C. Teichert, Applied Phys. **A76**, 653 (2003)

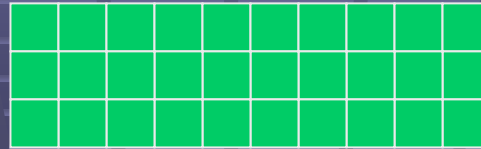
The lower figure is an AFM image of the multiple layers of Silicon-Germanium grown on top of Silicon substrate. As the number of adlayers is increased, there is an island like pattern that develops on a nano-meter scale. The driving mechanism for this is thought to be the shear stress between the substrate and the adlayer. The stress comes from the lattice mismatch. The mass motion is the atomic diffusion on the surface.



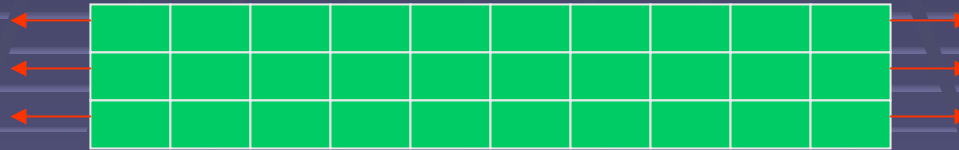
# 3. Intuitive picture of stress-driven instability

(no gravity, no surface tension)

begin with solid  
under zero stress

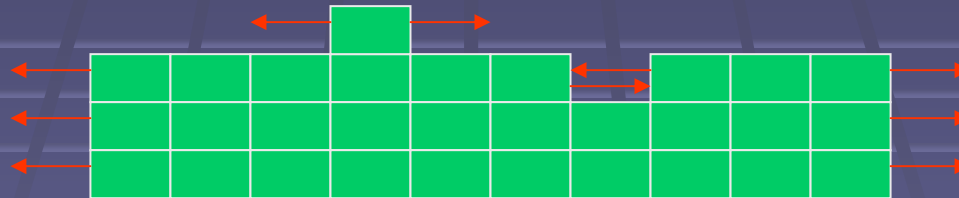


apply uniaxial stress



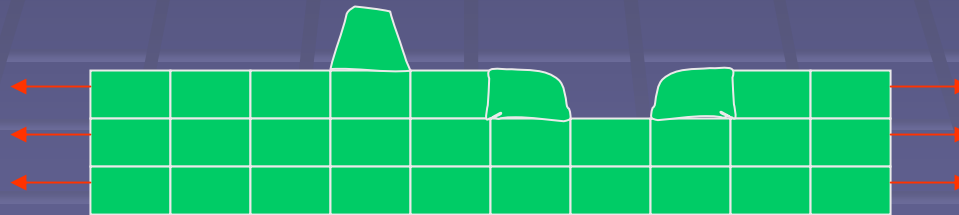
$E_{\text{regular}}$

fluctuation moves  
one element, with  
constant stress



$E_{\text{corrugated}} = E_{\text{regular}}$

without stress,  
solid relaxes



$E_{\text{corrugated}} < E_{\text{regular}}$   
→ instability!

The idea of stress-driven instability is illustrated with the help of these cartoons. Start with a piece of solid with no stress. Apply uniaxial stress from the side. The solid accumulates an elastic energy with regular strain. Suppose, by fluctuation, a cell melts and forms on top surface. If the all cells retain the regular shape, there is no change in elastic energy. If the cells at the bump and the dip are allowed to relax, the elastic energy will decrease. The process is then unstable and leads to instability. The effect is different from Euler buckling instability which occurs under compression only. And it occurs without mass transfer. I emphasize that the mass transport is important in this rearrangement instability.

# quantitative basis

(including gravity and surface tension -- these oppose surface deformation)

Assume: surface height profile:  $h(x) = \eta \cos(kx)$

net energy cost:  $U = (\text{gravity}) + (\text{surface tension}) + (\text{elastic energy})$

$$U = \frac{\eta^2}{4} \left[ (\rho_{\text{solid}} - \rho_{\text{liq}})g + \gamma k^2 - 2 \frac{(1 - \sigma^2)}{E} \sigma_0^2 k \right]$$

**g = gravitational constant**

$\gamma$  = surface tension  $\sim 0.3$  dyn/cm

$\sigma$  = Poisson's ratio

$E$  = Young's modulus

$\sigma_0$  = Applied stress

critical or threshold effects:

$$\text{critical stress : } \sigma_c = \sqrt{\frac{2\pi\gamma E}{\lambda_c(1 - \sigma^2)}}$$

$$\text{critical wavelength : } \lambda_c = \sqrt{\frac{\gamma}{g(\rho_{\text{solid}} - \rho_{\text{liq}})}}$$

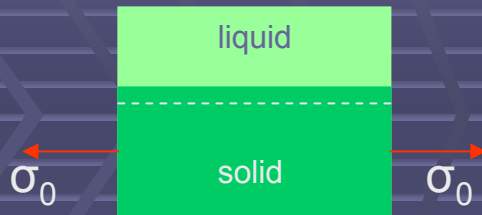
When the critical stress (or strain) is exceeded, corrugation with wavelength ( $\lambda_c$ ) of  $\sim 6$  mm should appear.

$$\sigma_c = 2.4 \times 10^4 \text{ dyn/cm}^2 \text{ or } u_c = 8 \times 10^{-5} \text{ (critical strain)}$$

The instability on the preceding page due to the decrease in elastic energy is opposed by gravity and surface tension. So at low stress levels, the surface remains flat. Beyond some critical stress, the instability sets. The instability can be made quantitative by considering sinusoidal surface height profile. Analysis shows that when a critical stress is exceeded, corrugation of wavelength of about 6 mm should appear. We wish to study this stress-induced instability on solid He-4. The critical stress or critical strain is easily achievable on solid He-4. Note the importance of gravitational acceleration constant.



# small stress below critical stress



applied stress  
increases the elastic  
energy of solid ...  
chemical potential  
increases ...  
equilibrium is broken



chemical potential  
of liquid must  
increase to come to  
equilibrium ... solid  
melts!

Assume isotropic solid for simplicity  
equilibrium is maintained if →

$$\begin{aligned}\delta\mu_{\text{solid}} &= \delta\mu_{\text{liquid}} \\ \delta\left(\frac{f_{\text{solid}} - \sigma_{zz}}{\rho_{\text{solid}}}\right) &= \frac{\delta P}{\rho_{\text{liquid}}} \\ \delta h &= -\frac{(1-\sigma)\sigma_0^2}{2Eg(\rho_{\text{solid}} - \rho_{\text{liquid}})}\end{aligned}$$

$f_{\text{solid}}$  = free energy/vol

$\sigma$  = Poisson's ratio

$E$  = Young's modulus

=  $3 \times 10^8$  dyn/cm<sup>2</sup> solidHe

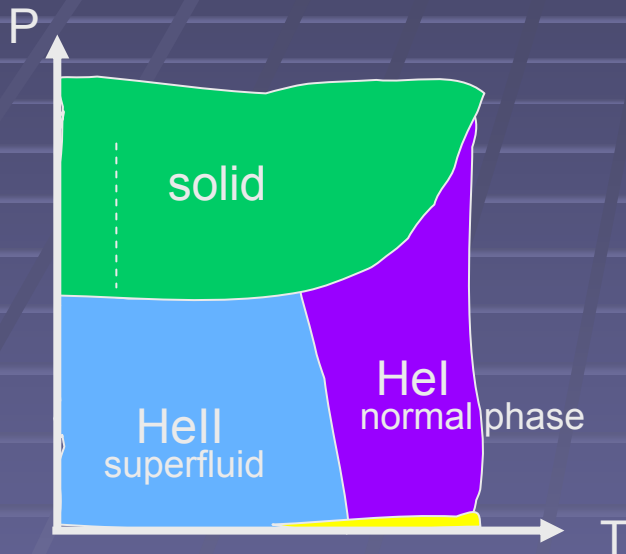
=  $\sim 10^{11}$  dyn/cm<sup>2</sup> Lead

The height of solid decreases under stress.

$$\delta h = -8.2 \times 10^{-11} \sigma_0^2 \text{ (cgs)}$$

What happens if the applied stress is less than the critical stress? Under stress, the chemical potential of the solid increases. In equilibrium, the chemical potentials of the two phases remain equal. To maintain equilibrium, the chemical potential of the liquid must then increase. That means, the solid should melt and the liquid depth should increase. We wish to observe this as a check on the applied stress in the linear response regime.

# Why use solid He-4?

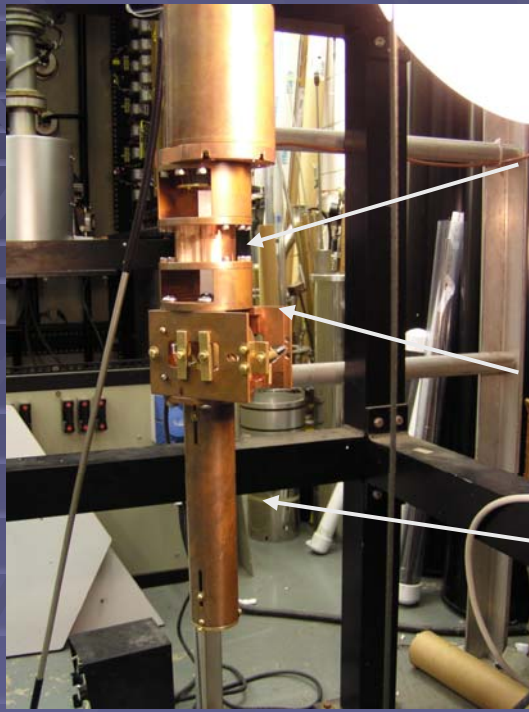


## Advantages:

- high purity
- superfluid "melt"  
rapid heat transfer
- small latent heat
- rapid melting and freezing
- relative ease in growing crystals
- mm scale corrugations

# 4. Apparatus

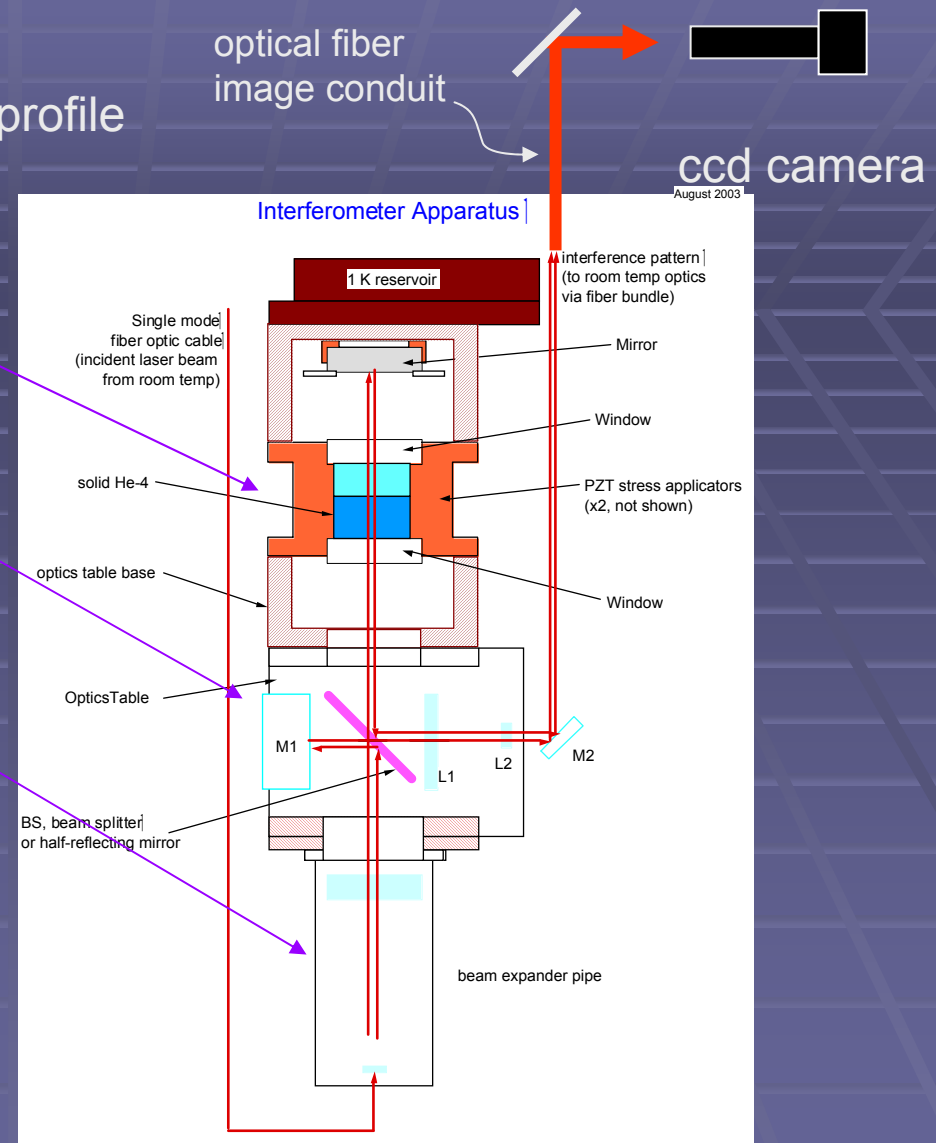
interferometer method to detect surface profile



solid He chamber

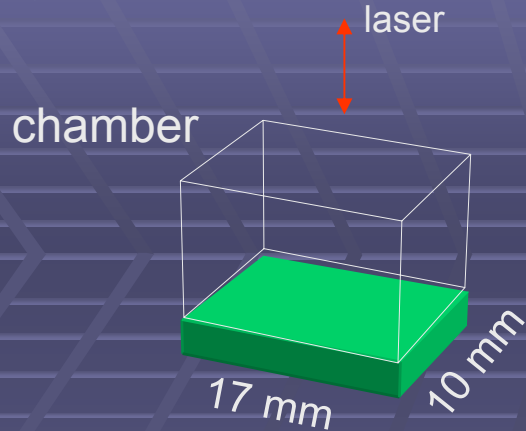
optics table

beam expander



We have constructed an interferometer apparatus to observe the solid height profile. Illumination He-Ne laser beam is fed into vacuum can at low temperature with an optical fiber. The beam goes through an expander and split into a reference beam and a probe beam. The probe beam goes through the chamber containing solid and liquid. The two beams combine to form an interference image. The difference in index of refraction and the spatial dependence of the solid height leads to changes in interference pattern. The interference image is captured with a CCD camera.

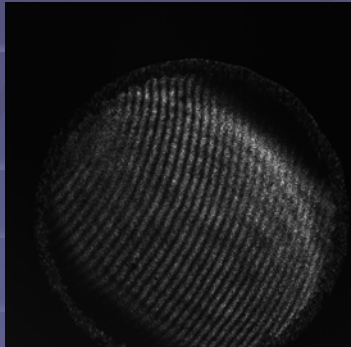
# 5. Results



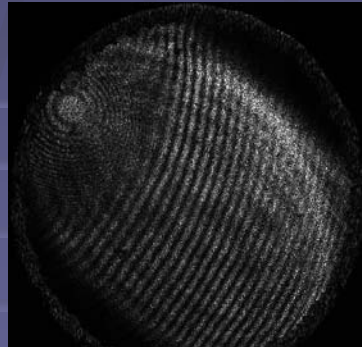
Process of formation, growth  
and melting of solid  $^4\text{He}$

$$T = 1.2 \text{ K} \quad P_{\text{melting}} \sim 25 \text{ bars}$$

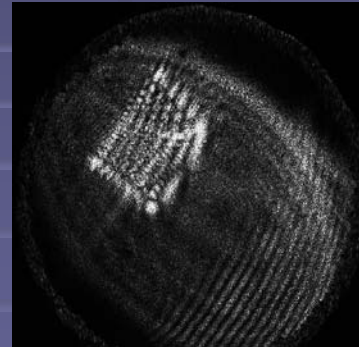
time sequence of interference pattern as solid grows in the chamber  
(total elapsed time = 70 min.)



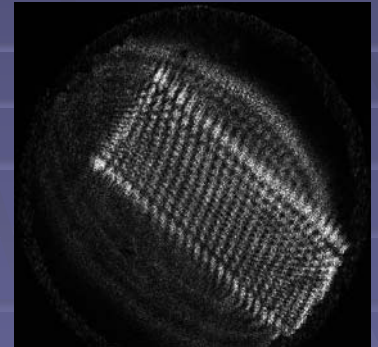
all liquid



→ solid seed appears



→ solid spreading

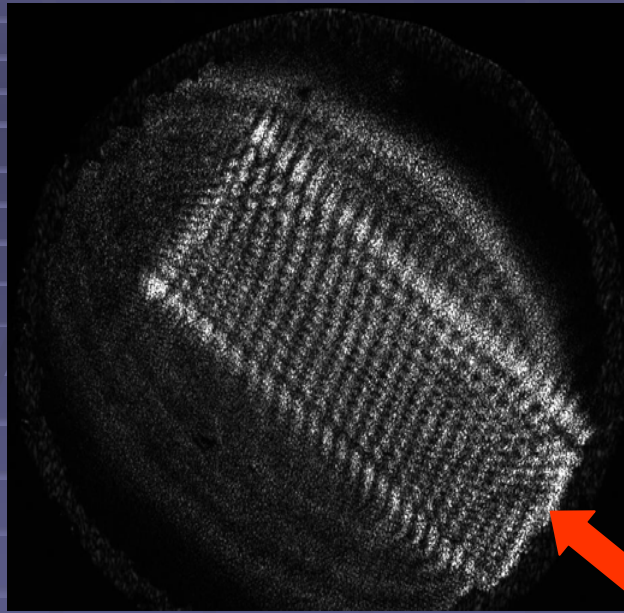


→ flat solid surface

A schematic of the chamber is shown. The movie shows the development of interference pattern from liquid. The temperature is near 1.2 K. Initially, the chamber contains all liquid near melting pressure. The pattern is caused by the misalignment of the two mirrors. The pressure is increased by forcing liquid into the chamber. A solid seed can be seen in the second video frame. Solid begins to grow and spread across the chamber bottom as in the third frame. As more helium is introduced, solid spreads all over the bottom surface of the chamber.

# applying stress to solid

Piston attached to PZT pushes or pulls on solid.



stress by piston  
attached to PZT

$$\text{strain} = 5.8 \times 10^{-8} \times (\text{applied voltage}), 0 < \text{strain} < 2 \times 10^{-4}$$

Convert fringe (or phase) shift  $\rightarrow$  height change (1 fringe shift =  $93 \mu\text{m}$ )

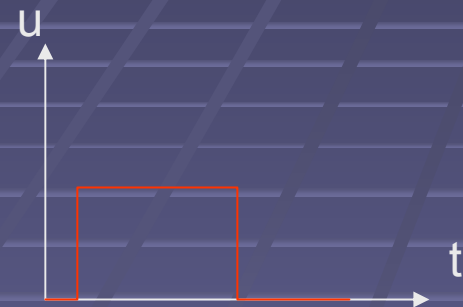
Stress is applied from one end of the chamber as shown. We use a tubular PZT to push a piston which in turn pushes or pulls on the edge of solid. We can apply more than 4500 V to PZT. The fringe pattern moves as the stress is applied. The changes of fringe pattern is converted to phase shift and finally to height changes.

# apply strain, $u < u_c$

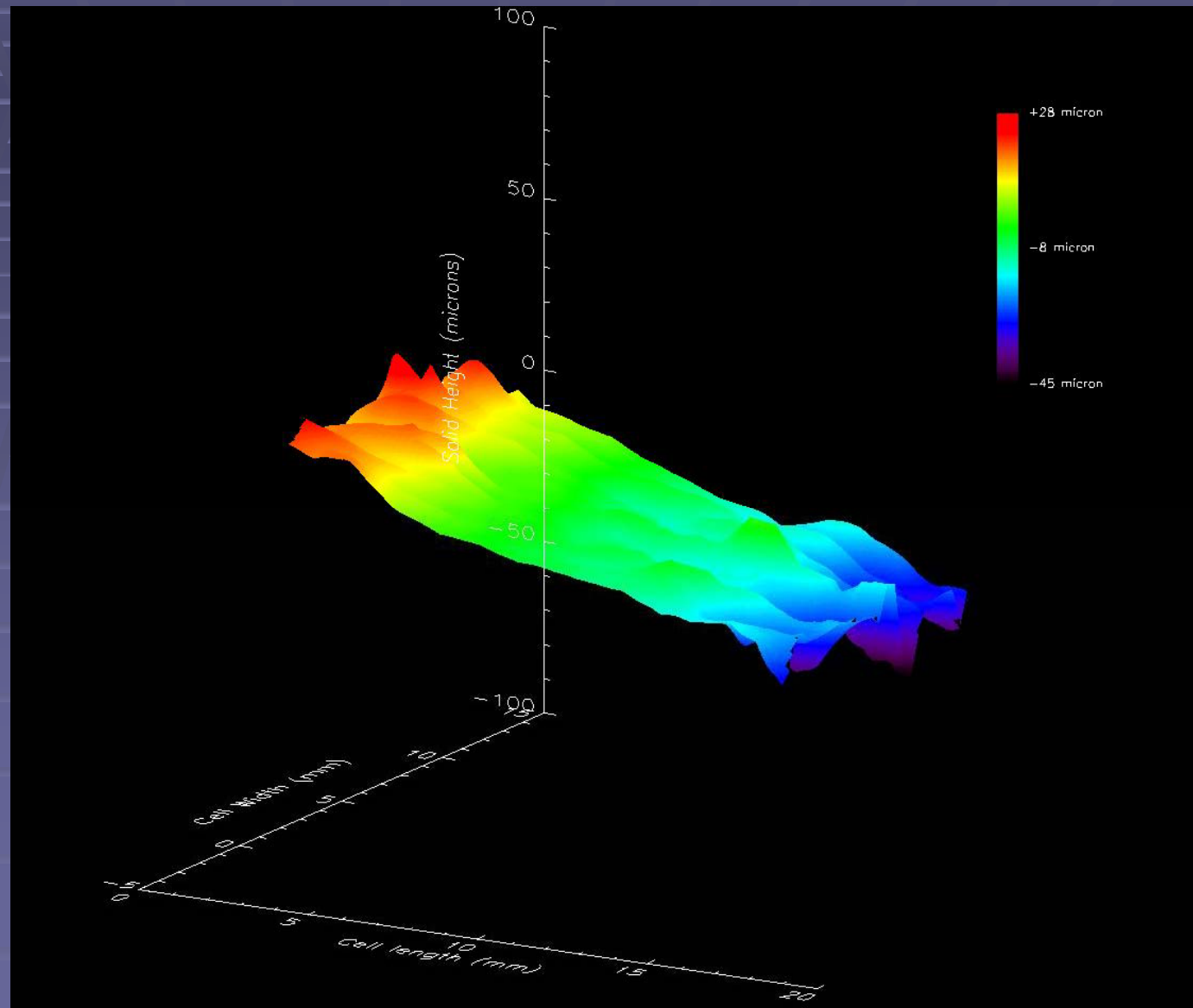
Uniform decrease in solid surface height is expected.

$$u = -5 \times 10^{-5}$$

$$|u_c| \sim 8 \times 10^{-5}$$



A strain smaller than the critical strain is applied at the beginning and is removed a little later. We expect to see a uniform decrease in solid height. We see a linear slope appearing as shown. When the strain is removed, the surface profile returns to the original flat shape. The profile motion is reversible but different from the expected behavior.

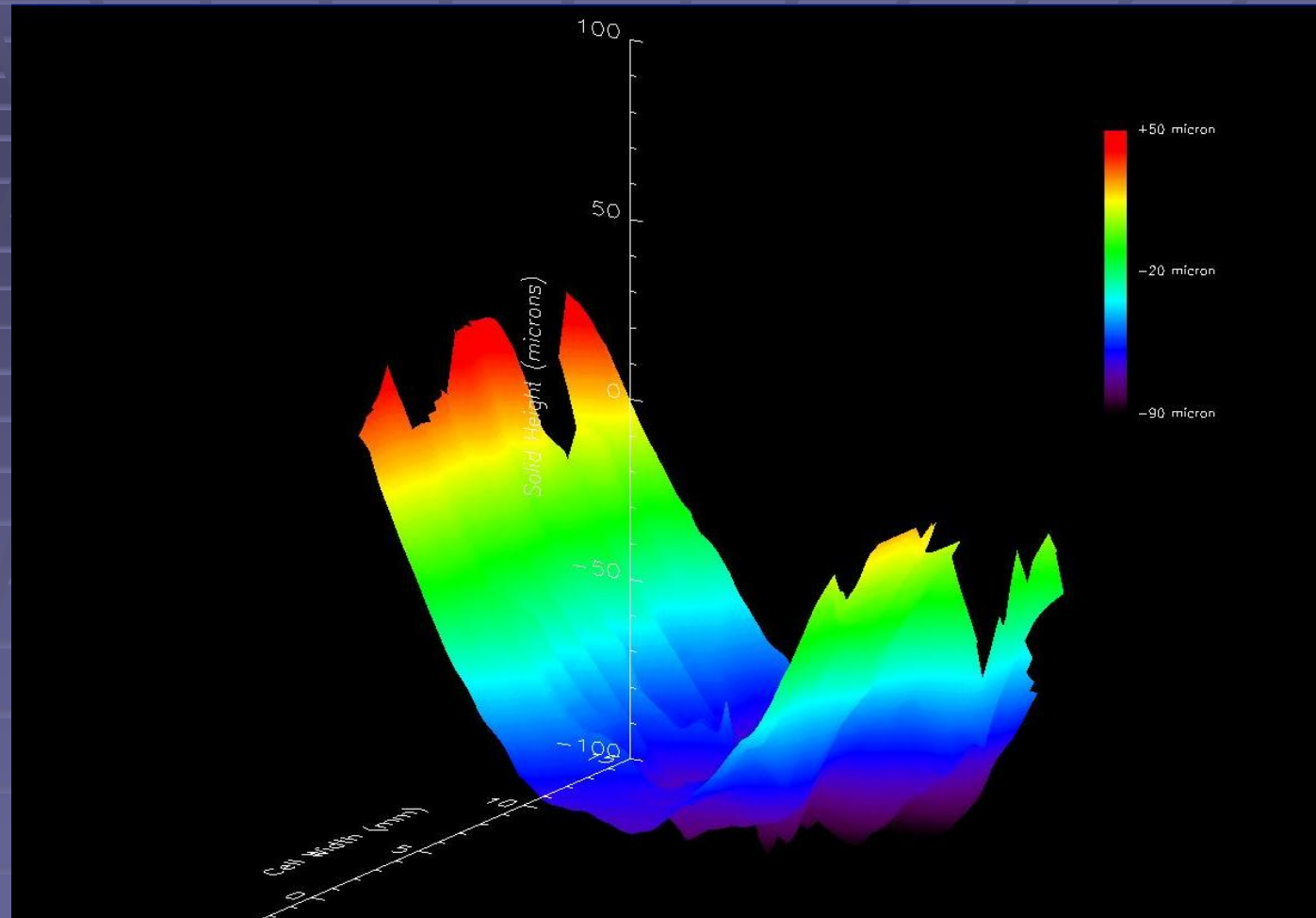
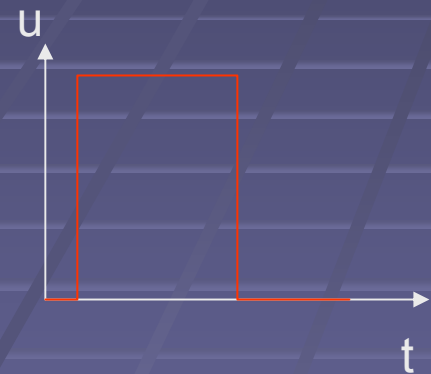




# apply strain, $u > u_c$

Corrugation on solid surface height is expected.

$$u = -11 \times 10^{-5}$$
$$|u_c| \sim 8 \times 10^{-5}$$



Let's see what happens when the applied strain is greater than the expected critical threshold. We expect to see corrugations according to theory. After the strain is applied, the surface profile develops an undulation as shown. When the strain is removed, the surface profile does not return to the original flat profile. The process is irreversible. The wavelength of the undulation is 15 mm, not 6 mm as expected. The onset of the undulation is not sudden as a function of strain. The undulation sets in more or less gradually

# Summary

- (1) Interferometer apparatus for measuring surface profile
  - (2) For small strains, the expected linear decrease in height is not seen.
  - (3) For large strains, undulation and irreversible deformations begin to set in, but we cannot yet make clear connection with stress-driven instability theory.
- Torii and Balibar have observed appearances of deformations beyond threshold stress on  $^4\text{He}$  solid surface.
  - The difference of our results from theory real? We are not ready to claim in affirmative.
  - To be able to answer:
    - improve crystal growth techniques ... orientation, annealing, better pressure control
    - improve homogeneity of stress ... better alignment with vertical, better understanding of interaction between solid He-4 and walls
    - improve optics



# acknowledgements

- Tamer Elkohly, Josiah Fay, Yuichiro Wada and Ryuichi Masutomi
- Misha Grinfeld and Pavel Grinfeld
- supported by NASA/ground-based research program